

Thermodynamic Investigation into Chemical Stability of
(La,Sr)Cr_xFe_{1-x}O_{3-δ} and Dual-Phase (La,Sr)Cr_xFe_{1-x}O_{3-δ}/ stabilized
Zirconia for Oxygen Transport Membranes

By

Hooman Sabarou

A Dissertation Submitted to the Faculty

of the

Worcester Polytechnic Institute

In partial fulfillment of the requirements for the degree of

Doctor of Philosophy

In

Manufacturing Engineering

November 12, 2019

Approved:

Abstract

Ceramics oxides with mixed ionic and electronic conductivity have received a lot of attention due to their wide range of applications in solid oxide fuel cells, interconnects, gas sensors, and ion transport membranes. However, owing to harsh operating conditions, the choice of proper materials and engineering their properties are still challenging. Perovskite and fluorite structures are two promising structures for ceramic membrane applications. The objective of this research is to explore the stability of lanthanum chromite-based perovskite ((La,Sr)(Cr,Fe)O_{3-δ}) as single phases and dual-phase composites with fluorite phases under fabrication and operating conditions of Oxygen Transport Membranes (OTM).

The current research has been categorized into two sections: structural and chemical stability of perovskite phases and dual-phase perovskite/fluorite composites. Also, investigation on both categories has been conducted with two separate approaches: experimental examinations and computational Thermodynamic. In the computational part, independent methods have been considered for the single-phase perovskite and dual-phase perovskite/fluorite composites. In the experimental section, the bulk chemical stability of the dual-phase samples has been examined under controlled oxygen partial pressure $p(\text{O}_2)$ atmospheres at 1400°C for 10 hours with slow and fast cooling rates. Besides, the phase stability of the perovskite structures as a single-phase has been also examined under OTM fabrication conditions.

The results present new phenomena in the chemical stabilities of the materials. They include formations of liquid phases, Sr-segregation, and perovskite phase separations. The correlations between compositions/ temperature/ $p(\text{O}_2)$ and secondary phases have been investigated to improve the chemical stability and extend the lifetime of the materials. The findings in this thesis enhance the knowledge about the chemical stabilities of OTMs and help to develop more reliable materials for ceramic-based OTMs.

Contents

Chapter 1 : Introduction	11
Objective	11
Ceramic Membranes	12
Perovskite-based ceramic membranes	13
Doping in perovskite structures	15
Fluorite Structure	16
Transport Mechanism and Performance in Oxygen Permeation Flux	17
Critical Issues in Ceramic Membranes	18
Dual-Phase Ceramic Membranes	19
Current Approaches for Perovskite-based Ceramic Membranes	20
Thesis Outline	21
Chapter 2 : Methodology	23
CALPHAD Approach and Computational Thermodynamic	23
1.1. La ₂ O ₃ -SrO-Mn ₂ O ₃ -Cr ₂ O ₃ system	24
1.2. La-Fe-O System	25
1.3. Cr-O System.....	26
1.4. La-Mn-Y-Zr-O, Y-Zr-O, and La-Sr-Mn-O Systems.....	27
1.5. La-Sr-Cr-Fe-Ar-H-O and La-Sr-Cr-Fe-O-H-Ar-Zr-Y-O Systems.....	28
2. Experimental Approach	28
2.1. Synthesis	28
2.2. Sample Preparation	30
2.3. Stability Tests.....	31
2.4. Materials Characterizations.....	32
Chapter 3 : Thermodynamic Assessment of the Chemical Stability of (La _{0.8} Sr _{0.2}) _{0.98} Cr _x Fe _{1-x} O _{3±δ} under Oxygen Transport Membrane Fabrication and Operation Conditions.....	39
Abstract.....	39
1. Introduction.....	40
2. Previous Investigation on the LSCrF Perovskite	41
3. Computational Thermodynamic	42
a. Thermodynamic Database and Models.....	43
b. Current La-Sr-Cr-Fe-O + H database.....	44
c. Simulated Conditions.....	44

4.	Predictions from the Computational Thermodynamic	45
a.	Solid/Liquid Phase Stability at 1400°C	45
b.	Thermodynamic Cooling Simulations	47
c.	Thermodynamic Equilibria with Gas	50
5.	Discussions	51
a.	Thermodynamic Consideration of the Sintering	51
b.	Liquid Phase Stability at High Temperature	51
c.	Emission of Cr ⁶⁺ Containing Gas Species.....	57
6.	Conclusions.....	57
Chapter 4 : The Origin of Phase Separation in (La _{0.8} Sr _{0.2}) _{0.95} (Cr _x Fe _{1-x})O _{3±δ} Perovskites		59
	Abstract.....	59
1.	Introduction.....	59
2.	Experimental.....	61
3.	Computational Thermodynamic	62
4.	Results.....	63
4.1	Thermodynamic Simulations	64
4.2	Crystal Structure and Ceramic Microstructure	68
4.	Discussion.....	72
4. 1)	The Perovskite Phase Separation.....	72
4. 2)	Dual-Phase Perovskite-Fluorite Composites	75
5.	Conclusion	78
Chapter 5 : The Chemical Stability of Dual-Phase Composites of (La, Sr)(Cr, Fe)O _{3-δ} - 8YSZ, 10Sc1YSZ, and 10Sc1CeSZ.....		80
	Abstract.....	80
1.	Introduction.....	80
2.	Previous Investigations in Dual-Phase Ceramic Membranes	81
3.	Experiments	84
4.	Computational Thermodynamic	85
a.	Thermodynamic databases and models.....	86
5.	Results.....	87
a.	The Effect of p(O ₂)	89
b.	The Effect of Sr.....	91
c.	The Effect of The Cr: Fe Ratio	93

d. Perovskite Phase Separation	96
e. Simulations by Computational Thermodynamic	99
6. Discussion	101
7. Conclusion	103
Chapter 6 : Conclusion and Future Work	105
1. The Contribution of This Dissertation	105
2. The future works	107
Reference:	109

List of Figures

Figure 1-1. Ceramic membrane oxygen ion transport	11
Figure 1-2. Three crystal structures of perovskite a) cubic, b) rhombohedral, and c) orthorhombic (Model structures are based on LaCrO ₃).	13
Figure 1-3. Fluorite-type structure based on the cubic symmetry of ZrO ₂	16
Figure 1-4. Current Challenges in mixed conducting ceramic membranes [6].	18
Figure 2-1. The diagram for the CALPHAD approach and its implementation.	23
Figure 2-2. Flowchart for the Sol-Gel synthesis procedure.	30
Figure 2-3. A pellet of a dual-phase composite sample after sintering at 1150°C for 2 hours under air.	31
Figure 2-4. Experimental setup for heat treatment and stability tests.	32
Figure 3-1. The diagram of the computational thermodynamic with using of Thermo-Calc.	43
Figure 3-2. Chemical stability of a) LSCrF-37, b) LSCrF-55, and c) LSCrF-73 with reduction in P(O ₂) at 1400°C.	47
Figure 3-3. The chemical stability of a) LSCrF-37, b) LSCrF-55, and c) LSCrF-73 during equilibrium cooling at P(O ₂)=10 ⁻¹⁰ atm.	48
Figure 3-4. The fast cooling simulation for the liquid phase for a) LSCrF-37, b) LSCrF-55, and c) LSCrF-73 at P(O ₂)=10 ⁻¹⁰ atm.	49
Figure 3-5. The Cr ⁺⁶ species in gas a) with change in P(O ₂) at 1400°C for the LSCrF-55, b) with change in temperature at P(O ₂)=10 ⁻¹⁰ atm for the LSCrF-55, and c) with change in Cr concentration at 1400°C and P(O ₂)=10 ⁻¹⁰ atm, and d) with change in H ₂ O concentration for LSCrF-55 at 1400°C and P(O ₂)=10 ⁻¹⁰ atm.	50
Figure 3-6. Sketch of the liquid phase stability with the change of P(O ₂) at 1400°C.	53
Figure 3-7. Threshold diagram for 0.2 moles of the liquid phase with the change in temperature and P(O ₂).	54
Figure 3-8. The liquid phase volume percentage with the A-site deficiency for (La _{0.8} Sr _{0.2}) _{1-y} Cr _x Fe _{1-x} O _{3±δ} (x=0.5, and 0≤y≤0.9) at 1400°C and P(O ₂)=10 ⁻⁶ atm and 1200°C and P(O ₂)=10 ⁻¹⁰ atm.	55
Figure 3-9. The schematic of the liquid phase (a, b) formation and (c, d) solidification.	56

Figure 4-1 Changes in a) phases stability and b) distribution of Fe in phases in $(\text{La}_{0.8}\text{Sr}_{0.2})_{0.95}\text{Cr}_{0.9}\text{Fe}_{0.1}\text{O}_3$ between 700 to 1300°C at $p(\text{O}_2)=10^{-18}\text{atm}$	65
Figure 4-2. Changes in a) phase stability and b) distribution of Fe in phases in $(\text{La}_{0.8}\text{Sr}_{0.2})_{0.95}\text{Cr}_{0.9}\text{Fe}_{0.1}\text{O}_{3\pm\delta}$ with changes in $p(\text{O}_2)$ (10^{-19} to 0.21 atm) at 850°C.....	66
Figure 4-3. The partitioning of Fe ion species (Fe^{2+} , Fe^{3+} , and Fe^{4+}) in Perovskite #1 and Perovskite #2 with changes in temperature at $p(\text{O}_2)=10^{-18}$ atm for $(\text{La}_{0.8}\text{Sr}_{0.2})_{0.95}\text{Cr}_{0.9}\text{Fe}_{0.1}\text{O}_{3\pm\delta}$	67
Figure 4-4. The formation of the perovskite#2 and liquid phase with changes in the Fe content in $(\text{La}_{0.8}\text{Sr}_{0.2})_{0.95}\text{Cr}_{0.9}\text{Fe}_{0.1}\text{O}_{3\pm\delta}$ at two different temperatures and oxygen partial pressures.	68
Figure 4-5. The XRD patterns of $(\text{La}_{0.8}, \text{Sr}_{0.2})_{0.95}\text{Cr}_{0.9}\text{Fe}_{0.1}\text{O}_3$ perovskite after heating at 850°C for 10 hours under wet forming gas (4% H_2 -96%Ar).	69
Figure 4-6. The microstructural analysis on the LSCrF91 after heating at 850°C for 10 hours under wet forming gas (4% H_2 -96%Ar): (a) the formation of the spinel phase (b) EDS map analysis.	70
Figure 4-7. The SEM pictures of the heat-treated (a) LSCrF81 and (c) and (e) LSCrF91 together with their corresponding quantitative line scan analyses.....	71
Figure 4-8. The formation of SrO with changes in the Fe content in the LSCrF91 ($T=850^\circ\text{C}$, $p(\text{O}_2)=10^{-18}$ atm).	73
Figure 4-9. The XRD patterns for LSCrF91-8YSZ after heat-treating at 850°C for 10 hours under wet forming gas (4% H_2 -96%Ar).	76
Figure 4-10. The analysis on peak shapes of LSCrF91-8YSZ after heat-treating at 850°C for 10 hours under wet forming gas (4% H_2 -96%Ar).	76
Figure 5-1. A schematic microstructure of a dual-phase composite of LSCrF-YSZ and transporting electrons and oxygen ions through different grains. Inspired by [8].	82
Figure 5-2. The XRD pattern for $(\text{La}_{0.8}, \text{Sr}_{0.2})_{0.95}\text{Cr}_{0.7}\text{Fe}_{0.3}\text{O}_{3-\delta}$ -8YSZ after heating at 1400°C for 10 hours under forming gas 1 (wet-0.1% H_2 -Ar).	88
Figure 5-3. The Microstructure analysis for $(\text{La}_{0.8}, \text{Sr}_{0.2})_{0.95}\text{Cr}_{0.7}\text{Fe}_{0.3}\text{O}_{3-\delta}$ -8YSZ after heating at 1400°C for 10 hours under forming gas 1 (wet-0.1% H_2 -Ar).	88
Figure 5-4.XRD patterns for $(\text{La}_{0.8}, \text{Sr}_{0.2})_{0.95}\text{Cr}_{0.8}\text{Fe}_{0.2}\text{O}_{3-\delta}$ -fluorite phases after heat treatment under argon for 10 hours.	90
Figure 5-5. XRD patterns for $(\text{La}_{0.8}, \text{Sr}_{0.2})_{0.95}\text{Cr}_{0.9}\text{Fe}_{0.1}\text{O}_{3-\delta}$ -10Sc1CeSZ after heat treatment at 1400C for 10 hours, forming gas 1 (wet-0.1% H_2 -Ar).	90

Figure 5-6. XRD patterns for $(\text{La}_{0.9}, \text{Sr}_{0.1})_{0.95}\text{Cr}_{0.7}\text{Fe}_{0.3}\text{O}_{3-\delta}$ -8YSZ and 10Sc1YSZ after heat treatment at 1400°C for 10 hours under air and forming gas 1 (wet-0.1% H_2 -Ar).....	91
Figure 5-7. Microstructural analysis on $(\text{La}_{0.9}, \text{Sr}_{0.1})_{0.95}\text{Cr}_{0.7}\text{Fe}_{0.3}\text{O}_{3-\delta}$ -8YSZ after heating at 1400°C for 10 hours under forming gas 1 (wet-0.1% H_2 -Ar).....	92
Figure 5-8. Microstructural analysis on $(\text{La}_{0.9}, \text{Sr}_{0.1})_{0.95}\text{Cr}_{0.7}\text{Fe}_{0.3}\text{O}_{3-\delta}$ -10Sc1CeSZ after heating at 1400°C for 10 hours under a and b) air c and d) forming gas 1 (wet-0.1% H_2 -Ar).....	92
Figure 5-9. XRD patterns for $(\text{La}_{0.8}, \text{Sr}_{0.2})_{0.95}\text{Cr}_{0.7}\text{Fe}_{0.3}\text{O}_{3-\delta}$ -8YSZ and 10Sc1YSZ after heat treatment at 1400°C for 10 hours under air and forming gas 1 (wet-0.1% H_2 -Ar)	93
Figure 5-10. Microstructural analysis on $(\text{La}_{0.8}, \text{Sr}_{0.2})_{0.95}\text{Cr}_{0.5}\text{Fe}_{0.5}\text{O}_{3-\delta}$ -8YSZ after heating at 1400°C for 10 hours under argon.	94
Figure 5-11. Changes in the phase content of SrZrO_3 with the Cr: Fe ratio for a)10Sc1YSZ, b)1Sc1CeSZ, and c) 8YSZ after heat treatments at 1400°C under argon and forming gas 1 (wet-0.1% H_2 -Ar).	95
Figure 5-12. The formation of the spinel phase in $(\text{La}_{0.8}, \text{Sr}_{0.2})_{0.95}\text{Cr}_{0.5}\text{Fe}_{0.5}\text{O}_{3-\delta}$ -10Sc1YSZ after the heat treatment at 1400°C for 10 h under argon.....	96
Figure 5-13. The occurrence of perovskite phase separation for LS2CrF82-10Sc1YSZ after a) heating under wet-4% H_2 -Ar at 850°C for 10 hours b) heat treating under air at 1400°C for 10 hours. Blue peak: Cr-perovskite, Black peaks: Fe-rich perovskite.....	98
Figure 5-14. The correlation between SZO and spinel phases with changes in $p(\text{O}_2)$ at 1400°C in LS2CrF73-8YSZ.....	100
Figure 5-15. The formation of SZO with changes in a) temperature and b) the Cr: Fe ratio at 1400°C under different oxygen partial pressures ($p(\text{O}_2)$).	101
Figure 5-16. The formations of spinel and liquid phases with changes in the Cr: Fe ratio under different $p(\text{O}_2)$ conditions at 1400°C.	101
Figure 5-17. Involved parameters in the formations of a) $(\text{La}_{0.5}\text{Zr}_{0.5})\text{O}_{1.75}$ (LZO) and b) SrZrO_3 (SZO) phases in $(\text{La},\text{Sr})(\text{Cr},\text{Fe})\text{O}_{3-\delta}$ -8YSZ dual-phase composites.	103

List of Tables

Table 2-1. The list of raw materials for the Sol-Gel synthesis procedure.	29
Table 2-2. Reference structures for fluorite, perovskite, and secondary phases.....	33
Table 3-1. The composition for the corundum ($(\text{Fe}_x\text{Cr}_y)_2\text{O}_3$) ($\text{P(O}_2)=0.1\text{ atm}$) and spinel ($(\text{Fe}(\text{Fe},\text{Cr})_{2-x}\text{O}_4)$) phases ($\text{P(O}_2)=10^{-2}\text{ atm}$) at 1400°C for each perovskite composition.	45
Table 3-2. The predicted composition of the liquid phase formed from LSCrF-37, 55, and 73 at 1400°C and under $\text{P(O}_2) = 10^{-10}\text{ atm}$	46
Table 3-3. The compositions of the perovskite #1,2, and 3 for LSCrF-73 at 1000°C and $\text{P(O}_2) = 10^{-10}\text{ atm}$	49
Table 4-1 The refined parameters for $(\text{La}_{0.8}\text{Sr}_{0.2})_{0.95}\text{Cr}_x\text{Fe}_{1-x}\text{O}_{3\pm\delta}$ perovskites after the heat-treatment at 850°C for 10 hours under wet forming gas (4% H_2 -96%Ar).....	69
Table 4-2 The refined parameters for LSCrF91-8YSZ after the heat-treatment at 850°C for 10 hours under wet forming gas (4% H_2 -96%Ar).	77
Table 5-1. The list of examined compositions of perovskite and fluorite.	84
Table 5-2. The list of the analyzed phases with their reference card numbers and crystal structures.	89
Table 5-3. Perovskite phase separation in dual-phase composites sample (perovskite#1 is Cr-rich, and perovskite #2 is Fe-rich).....	97

Chapter 1 : Introduction

Objective

“Oxygen is among the top five chemicals produced worldwide by volume.” In the gas industry, oxygen production can make over \$75 billion in annual sales [1, 2]. Purified oxygen has a critical role in the production of clean power, ferrous and non-ferrous metals, chemicals paper, glass, cement, pulp, and petrochemicals. The conventional and commercial methods to produce purified oxygen are cryogenic distillation, pressure swing adsorption (PSA), and polymeric membranes. In addition to the listed methods, one of the new and advanced techniques for producing purified oxygen is dense ceramic membranes or Oxygen Transport Membranes (OTM). It is promised that membrane-based electrochemical separation of oxygen from air will significantly reduce capital cost and energy for oxygen production. A commercial OTM should deliver unique properties of mixed ionic and electronic conductivity and maintain its performance in temperatures above 700°C and oxygen partial pressure ($p(\text{O}_2)$) gradient ($p(\text{O}_2)$ air/ $p(\text{O}_2)$ fuel) exceeding 10,000 [3, 4]. To achieve commercial success, the membrane should survive more than 40,000 hours under these conditions [3]. Compared to conventional methods, ceramic membranes have some advantages [5]:

- 1) Using air as the oxidant, only passing oxygen, and eliminating N_2
- 2) Reducing the cost of gas compression in downstream processing
- 3) Achieving high product selectivity
- 4) Avoiding the formation of environmental pollutants like NO_x

Figure 1-1 schematically shows the performance of a ceramic membrane at operating conditions.

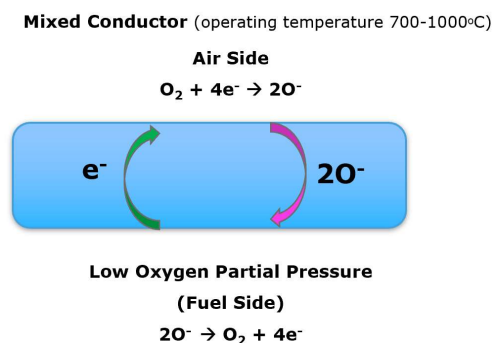


Figure 1-1. Ceramic membrane oxygen ion transport

Another approach in developing OTM materials is to mix perovskite and fluorite phases and design a dual-phase perovskite/fluorite composite, to take advantage of the best traits of each. In this design, the fluorite phase is responsible for ionic conductivity, and the perovskite phase presents both electronic and ionic conductivity. Based on this, oxygen ions inside the membrane structure have more available paths to transport. It results in higher oxygen flux, compared to single-phase material [3]. In the choice of the fluorite phase, there are options between Scandia stabilized Zirconia (ScSZ) and Ytria stabilized Zirconia (YSZ).

Ceramic Membranes

Ceramic-based membranes are unique materials, which transport both oxygen ions and electrons across a gas-impermeable membrane. For Oxygen Transport Membrane (OTM), the gas is oxygen. From mass transport characteristics, they can be categorized into pure oxygen conducting membranes and mixed ionic-electronic conducting membranes [6]. The former is called Solid Electrolyte, and it needs electrodes for electron pathways and external electrical circuit (figure). The advantage of using an external electrical circuit is to control the amount of produced oxygen via applying an electrical current.

On the other hand, membranes with mixed ionic-electronic conductivity can perform with neither electrodes nor external currents (Figure 1-1). In these membranes, oxygen ions are transferred from a side with high oxygen partial pressure (airside) to another side with lower oxygen partial pressure (fuel side), while electrons are moved in the opposite direction. Accordingly, the charge neutrality can be maintained across the membrane.

Regardless of the advantages of using ceramic membranes for producing oxygen from the air, the choice and design pertinent materials for this application remains an exciting research topic. Structures with mixed ionic-electronic conductivity typically have defined phase structures of perovskites (ABO_3), fluorites (AO_2), brownmillerite ($A_2B_2O_5$), Ruddlesden-Popper ($A_{n+1}B_nO_{3n+1}$), and pyrochlores ($A_2B_2O_7$). By the end of the 1980s, dense stabilized Zirconia was well-known as an oxygen ion conductor. However, its low oxygen permeation rates limited the application of ceramic membranes [5]. In 1985, new studies on perovskite structure revealed that some perovskite structure could present oxygen permeation rates one or two orders higher than dense stabilized zirconia while they have mixed ionic and electronic conductivity. From that date to now, different perovskite compositions have been examined.

Perovskite-based ceramic membranes

Perovskite oxides are of great interest due to having exceptional catalytic, ionic, and/or mixed ionic-electronic transport properties under extreme conditions. A perovskite structure is represented as $ABO_{3\pm\delta}$, where A and B stand for metallic cations and O is for oxygen. Different metallic ion species for cations are possible in perovskite structures if the total positive valance is equal to 6. The variations can be $A^{2+}B^{4+}O_3$, $A^{3+}B^{3+}O_3$, or $A^{1+}B^{5+}O_3$. On the anion site (oxygen), nonstoichiometry is denoted by δ , which is commonly negative [7]. In a perovskite structure, A-site cations have twelve-fold coordination while B-site cations have 6-fold coordination. From the crystallographic point of view, the ideal crystal structure of perovskite is cubic (Figure 1-2). The stability of the eight BO_6 octahedral is a key requirement to maintain the cubic structure. The stability of the cubic structure depends on A-site and B-site cation radii. Increase of A-site cation radius ($1.10\text{-}1.80 \text{ \AA}$, $> 0.9 \text{ \AA}$) and decrease of B-site cation radius ($0.62\text{-}1.00 \text{ \AA}$, $> 0.51\text{\AA}$) promote the cubic symmetry [8]. However, the cubic symmetry in perovskites changes toward lower symmetries, including rhombohedral and orthorhombic, due to the involvement of two factors: applied conditions and the presence of dopants (Figure 1-2). The applied conditions for oxides refer to temperature (T) and oxygen partial pressure ($p(O_2)$) under the fabrication and processing stages. The presence of dopants refers to partial substitution of A- and B-sites cations with other cations to tune the ultimate properties of the perovskite.

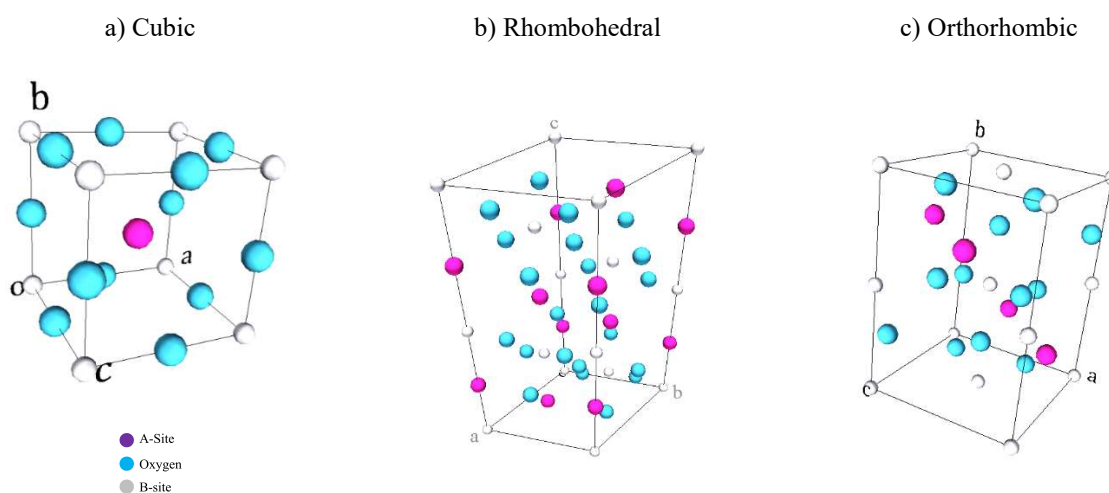


Figure 1-2. Three crystal structures of perovskite a) cubic, b) rhombohedral, and c) orthorhombic (Model structures are based on $LaCrO_3$).

Goldschmidt's tolerance factor can examine structural stability and changes in crystal symmetry of perovskites concerning A-site and B-site cation size [9]:

Equation 1 Goldschmidt tolerance factor

$$\text{Goldschmidt's tolerance factor } (t) = \frac{(r_A+r_B)}{\sqrt{2}(r_B+r_O)}$$

Where r_A , r_B , and r_O are the ionic radii units of A-site, B-site cations, and oxygen anions, respectively. Goldschmidt's tolerance factor has been widely accepted as a criterion for the formation of perovskite structures. The observed tolerance factors for perovskite compounds have been between 0.75 to 1.00 so far. The higher tolerance factor means higher crystal symmetry. However, doping perovskites on both A-site and B-site has added some complexity in the use of Goldschmidt's tolerance factors for these structures. Owing to this fact, Recently, Bartel et al. have revised Goldschmidt's tolerance factor and proposed a new tolerance factor [10]. The new tolerance factor can consider the content of dopants and their oxidation states.

Equation 2 New tolerance factor

$$\tau = \frac{r_X}{r_B} - n_A \left(n_A - \frac{r_A/r_B}{\ln(r_A/r_B)} \right)$$

Where n_A is the oxidation state of A, r_i is the ionic radius of ion i, $r_A > r_B$ by definition. If $\tau < 4.18$, the structure is a perovskite.

An ideal structure of perovskite with cubic symmetry has no capacity for ionic conduction. However, perovskites can tolerate a high number of defects inside their structures, which are the primary source of diffusion and conduction. This unique character is the main reason to use these materials for ceramic membranes. Defects in perovskite are mainly controlled by temperature, $p(O_2)$, and dopants. Temperature and $p(O_2)$ are two environmental parameters that are applied to perovskites during fabrication and processing conditions. However, dopants are needed to be engineered in initial perovskite compositions.

Doping in perovskite structures

Perovskite structures are very welcome to host external metallic cations as dopants on both A-site and B-site. A perovskite structure with substitutions for either A-site, B-site, or both can be referred to as $A_xA'_{1-x}B_yB'_{1-y}O_{3-\delta}$. The effects of dopants can be categorized through two approaches. Firstly, dopants participate in the formation of secondary and intermediate phases during fabrication and processing conditions so that they can change sinterability, densification, chemical stability, thermal behavior, and mechanical properties. Secondly, as new cations are introduced to a perovskite structure, defect chemistry will be changed to maintain charge neutrality inside the structure and balance the total mass. It leads to changes in crystal symmetry, concentrations of defects, and angles and strength of A-O and B-O bonds. Consequently, the physical properties of the perovskite, such as electrical conduction, thermal expansion, lattice structure, and oxygen permeation can be affected. Hence, the doping strategy is widely utilized to tune the ultimate properties of perovskites.

However, owing to the widespread and simultaneous effects of dopants on several characteristics of perovskites, a proper doping strategy has always been a challenge. The appropriate doping strategy includes the dopants choice and dopant level, and it is vital to enhance ultimate physical properties. For perovskite-base ceramic membranes, the best physical properties have been reported for cations of transition metals as dopants. It makes defect chemistry of these perovskites more complicated due to change in oxidation states of these ions with temperature and $p(O_2)$. Indeed, change in valance states of these dopants results in changes in their ionic radii on both A-site and B-site. It ends up changes in crystal symmetries, thermal expansion, electrical conductivity, mechanical properties, and chemical stability of perovskites. Hence, the proper selection of effective doping strategies is essential to enhance oxygen flux in perovskite-type ceramic membranes.

Lanthanum series perovskites ((La) as A-site cation and transition metals (Cr, Fe, Mn, Ni, and Co) as B-site cations have received a lot of attention due to their superior oxygen flux properties and stability to the operating conditions of OTM. Chemical stability of lanthanum series perovskite changes with change in B-site cation so that two undoped perovskites of $LaCrO_{3-\delta}$ and $LaFeO_{3-\delta}$ can stay stable at 1000°C up to $p(O_2)=10^{-22}$ atm and $p(O_2)=10^{-17}$ atm, respectively [11]. Another attractive characteristic of the perovskite structures is the ability to tune final properties by adding different dopants in either A-site or B-site or both. To develop new materials for OTM

application, many dopants for A-site, B-site, or both have been examined. Strontium as A-site and Fe as B-site are two promising dopants in lanthanum chromite-based perovskites. In addition to the superior chemical stability of lanthanum chromite perovskites ($\text{LaCrO}_{3-\delta}$), these two dopants enhance both electronic and ionic conductivity and promote oxygen flux.

Fluorite Structure

Fluorite oxide structures are represented with AO_2 , where A is a sizeable four-valent cation. The crystal structure of fluorite with cubic symmetry has been shown in the below figure. Large cations are settled in the FCC structure as oxygen anions form a simple cubic structure inside the fluorite structure via occupying interstitial sites.

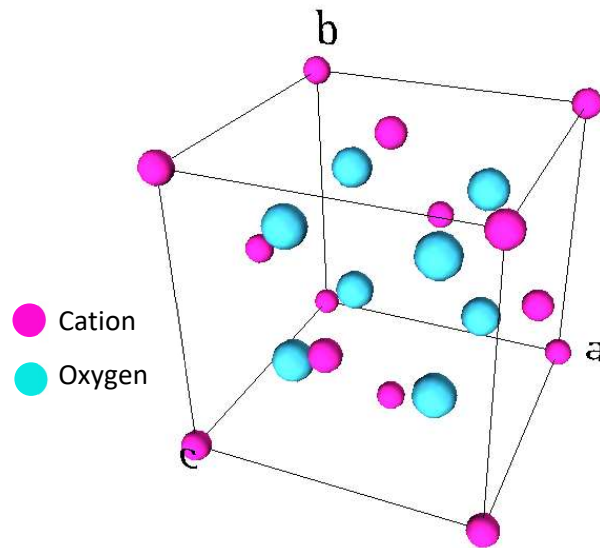


Figure 1-3. Fluorite-type structure based on the cubic symmetry of ZrO_2 .

Fluorite oxides have high ionic conductivity, but they show poor electronic conductivity. Accordingly, they have mainly used as layered electrolytes for solid oxide fuel cells (SOFC). The application of fluorite oxides for SOFC is mostly narrowed down to ZrO_2 , Bi_2O_3 , and CeO_2 . Structures of these oxides are primarily manipulated by doping to enhance their ionic conductivity and stability. Ceria (CeO_2) is mainly doped with Gd (gadolinium), Sm (samarium), or Pr (praseodymium).

Zirconia (ZrO_2) is the most investigated fluorite structure with reliable properties. It has several polymorphs, which their existences depend on temperature, dopants, and atmospheric conditions. Zirconia converts from monoclinic ($<1000^\circ\text{C}$) via tetragonal ($1100\text{--}2370^\circ\text{C}$) to cubic

(>2370°C) structures with changes in temperature. However, only its cubic structure presents effective ionic conductivity. Accordingly, several dopants such as Y₂O₃ (Yttria), Y, Ce, and Sc₂O₃ (Scandia) are added to the zirconia structure to stabilize its cubic phase. Yttria-Stabilized Zirconia and Scandia-Stabilized Zirconia are referred to as YSZ and ScSZ, respectively. To avoid the formation of the rhombohedral phase in ScSZ, it is usually co-doped with Ce or Y.

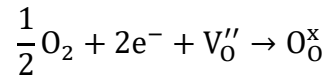
The advantages of using stabilized structures of zirconia refer to their low thermal/chemical expansion and excellent phase stability in the exposure of reducing atmospheres and CO₂ gas.

Transport Mechanism and Performance in Oxygen Permeation Flux

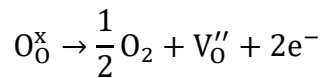
The oxygen separation process can be divided into at least four steps:

1. diffusion of oxygen molecules to the membrane surface on airside
2. dissociation of molecular oxygen into oxygen ions, consuming electrons

This can be expressed by using the Kröger-Vink notation as below :



3. diffusion of oxygen ions through the membrane via oxygen vacancies, counterbalancing with the flux of electron in the opposite direction
4. Recombine or react of oxygen ions on the fuel side, releasing electrons. The following formula can represent the reaction:



The driving force for oxygen transport is chemical activity or oxygen partial pressure gradient between air and fuel sides. However, there are other rate-limiting factors, which they interact with each other. One of these factors is the operating temperature. Oxygen permeation flux is insignificant for low temperatures (<600°C). When temperature increases, there is a considerable oxygen permeation flux value due to an increase in oxygen ions diffusion and/ or surface reaction rate. The thickness of membranes is another significant rate-limiting factor, especially in correlation with operating temperatures. The transport resistance in membranes can

be controlled with surface exchange reaction and bulk diffusion. Both two parameters can be affected by the thickness of membranes concerning the operating temperature. At low temperatures, the surface exchange reaction acts as the rate-limiting factor, while the bulk diffusion becomes the rate-limiting factor at elevated temperatures. Overall, the thickness of membranes has a critical effect on the oxygen permeation flux so that the reduction in the thickness can lead to an abrupt increase in the oxygen flux. The increase in the oxygen flux primarily occurs for operating temperatures above 800°C. The pressure of gases on both air and fuel sides can also be critical. High pressure of air and low pressure of the fuel side can improve the oxygen flux through membranes, but there is a threshold behavior for this factor. Other factors like the sintering profile, microstructure, and thermal history of the bulk are essential, as well. For most of the materials, a temperature above 700°C and partial pressure gradients ($p(\text{O}_2)_{\text{air}}/p(\text{O}_2)_{\text{fuel}}$) above 10,000 are necessary to achieve a commercial significance.

Critical Issues in Ceramic Membranes

Materials development is the main obstacle for using ceramic membranes as OTMs. Significant advances have been made in past decades; however, there are several issues with mixed ionic-electronic conductivity ceramic membranes. Figure 1-4 presents the main challenges in ceramic membranes in OTM applications.

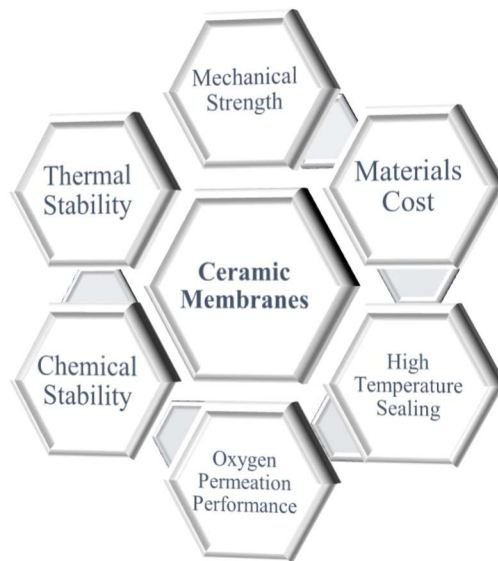


Figure 1-4. Current Challenges in mixed conducting ceramic membranes [6].

To tackle these issues, many techniques and measures have been proposed, but sometimes improvements in one or two factors end up sacrificing other parameters. For instance, a reduction in thickness of membranes has been proposed as a practical manufacturing technique to enhance oxygen permeation flux through reducing bulk diffusion. However, the mechanical strength of membranes will be compromised as their thickness decreases. To reinforce their mechanical strength of thin membranes, it has been suggested to use porous supportive materials. In this practice, chemical stability and compatibility of the supportive materials with the membranes should also be factored in. One of the studied supportive materials is α -Al₂O₃. However, its thermal expansion is almost lower than all mixed ionic-electronic ceramic membranes. It results in the formation of cracks in membranes. The existence of cracks in the membranes is detrimental to their gas-tight character. To overcome this issue, another measure is to use identical materials for both support and membrane. This measure requires fabricating ceramic material while one part of it is porous, and the other part is dense. Also, to improve oxygen permeation flux, the size of porous in the support should be smaller than the thickness of the membrane. Overall, it requires extensive research and development to tackle these problems without compromising other properties.

One of the most critical problems of ceramic membranes is their chemical stability. Indeed, most of the ceramic membranes with high mixed ionic- electronic conductivity suffers from low chemical stability and vice versa. The main reason for this refers to the existence of alkaline metals on the A-site of perovskite-based membranes. The presence of these elements leads to higher oxygen permeation flux, but they have low chemical stability due to reacting with water, SO₂, CO₂ etc. [12-16]. Accordingly, there are several methods to extend the chemical stability of these membranes, especially perovskite-base membranes. Doping is one of the most common ways to enhance stability; however, heavily doped structures pass through complicated chemical and structural changes under operating and fabrication conditions. Hence, doping to extend the chemical stability requires further investigations.

Dual-Phase Ceramic Membranes

The advent of the dual-phase ceramic membranes is the response to meet the requirements of ceramic membranes in one phase. A dual-phase ceramic membrane has been composed of an

ionic conducting phase with an electronic conductive phase as a mixed conductive membrane material. As it has been schematically shown in Figure 1-1, a dual-phase ceramic membrane has a dispersion of the ionic conducting phase in another phase with superior electronic conductivity.

The idea to design dual-phase ceramic membranes has been proposed by Wang, Li, and Kharton [17]. The main motive for this design is to reduce the cost of ceramic membranes. However, due to harsh operating conditions for these membranes, two phases in dual-phase membranes should have similar thermal expansion and remain chemically inert to each other over the lifetime of the membranes. Hence, the choice of phases for the dual-phase ceramic membranes require comprehensive investigations on fabrication and processing conditions.

Current Approaches for Perovskite-based Ceramic Membranes

Perovskite-base ceramic membranes have applications in oxygen separation membranes, Solid Oxide Fuel Cell (SOFC), and membrane reactors. There is a high demand for further advancement in these technologies due to their critical roles in less emission and higher efficiency energy production process. These three applications have some common characteristics, including high operating temperatures and harsh atmospheric conditions. Perovskite is exposed to elevated temperatures ($>500^{\circ}\text{C}$) to have enough content of oxygen vacancies for reliable ionic conduction. Investigations into perovskites for these three applications can be categorized into three parts.

The first part is to improve the oxygen permeation flux through engineering, either the thickness of membranes or compositions of perovskites. The current trend in this field is to reduce the thickness of the membrane to minimize the effect of bulk diffusion as the rate-limiting factor. Also, there are reports on the improvement of kinetic of the surface exchange stage due to the use of porous surfaces or coated surfaces with silver.

The improvement in the oxygen permeation flux has also been investigated via tuning compositions of perovskite for the increase in ionic conductivity. As mentioned before, modifications in perovskite compositions occur with adding dopant on both A-site, B-site, or both. For most perovskite-base membranes, electronic conductivity is generally higher than ionic conductivity; accordingly, the focus of current researches has been directed to increase ionic conductivity by adding dopants. Adding dopants can increase the total volume of unit cells,

decrease metal-oxygen bond energy, increase oxygen vacancy concentrations, and push crystal structures toward higher symmetries. All of these phenomena facilitate the transportation of oxygen ions inside the lattice via hopping mechanism and finally improve ionic conductivity.

The second part of the current approaches has been dedicated to the design and manufacturing of membranes. Most of the investigations are on the disk shape membranes due to the convenience of their productions. However, the disk-shaped membranes have some limitations owing to sealing, connection, and pressure resistance. Also, the surface of membranes is limited in a disk-shaped membrane. To tackle this problem, membranes in shapes of thin tubes and hollow fibers have been proposed. In these geometries, they can provide larger surface areas per unit volumes so that they can have remarkable oxygen permeation flux ($>10 \text{ mL cm}^{-2} \text{ min}^{-1}$) [6, 8].

The third part of the current investigations into perovskites for ceramic membranes is to search for measures to improve chemical stability. Indeed, while several perovskites with high oxygen permeation flux have been reported by adding dopants, their applications have been limited due to their poor structural stability at high temperatures and reducing atmospheres. Lanthanum cobaltite-base perovskite can be referred to as an example [18]. Limitations applied by poor chemical stability have also been reported for other techniques. For instance, using a silver coat on the surface of membranes cannot be employed widely due to the poor stability of silver at elevated temperatures. Endeavors toward better membranes design have been affected by poor chemical stability as well. The degradation of thin tubes and hollow fibers over long-term runs is not economical for industries. Accordingly, a significant portion of the investigations into perovskite-base ceramic membranes has been assigned to the improvement of their chemical stability under operating conditions.

Thesis Outline

This thesis will be organized into six (6) chapters.

Chapter 1 introduces perovskite-base ceramic membranes.

Chapter 2 explains about computational thermodynamic approach, its advantages, and

Chapter 3 describes the Thermodynamic assessment on the chemical stability of $(\text{La,Sr})(\text{Cr,Fe})\text{O}_{3\pm\delta}$ perovskites via computational Thermodynamic and investigates the formations of Cr^{+6} ions as a carcinogenic species

Chapter 4 examines the perovskite phase separation in $(\text{La, Sr})(\text{Cr, Fe})\text{O}_{3\pm\delta}$ and focuses involved mechanism and parameters

Chapter 5 discusses the chemical stability of dual-phase fluorites and $(\text{La, Sr})(\text{Cr, Fe})\text{O}_{3\pm\delta}$ perovskites with two computational and experimental approaches

Chapter 6 summarizes the contribution of the present work and discuss future work.

Chapter 2 : Methodology

CALPHAD Approach and Computational Thermodynamic

“CALPHAD is an abbreviation of CALculation of PHase Diagrams, but later it has been expanded to refer to Computer Coupling of Phase Diagrams and Thermochemistry” (Thermo-Calc website). The approach is based on two sets of data: first-principles calculations as theoretical data and available experimental Thermodynamic data on phase equilibria and thermochemical properties. Owing to employing these two sets of data and applying mathematical models with adjustable parameters, a description for Gibbs energy can be written for each phase in a system, which is a function of temperature, pressure, and constituents of that phase. Descriptions of Gibbs energies for different phases of a system can be optimized via fitting adjustable parameters with available theoretical/ experimental data. With having reliable descriptions of Gibbs energies, phase diagrams and thermochemical properties can be re-calculated, and then results can be extended to new conditions. Accordingly, the CALPHAD approach can be employed as a powerful tool to predict stable and metastable phases and simulate a system under unique circumstances. Based on this approach, many thermochemical data such as enthalpy, entropy, heat capacity, and activity can be derived for new settings of temperature, pressure, and compositions. With accurate models for phases of a system, the CALPHAD approach can also examine phase stabilities of phases in a system. The below flowchart presents the steps as mentioned earlier in the CALPHAD approach (Figure 2-1).

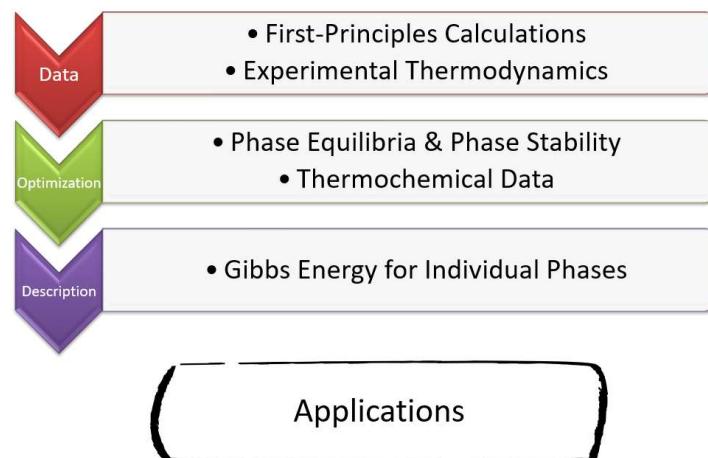


Figure 2-1. The diagram for the CALPHAD approach and its implementation.

The purpose of using CALPHAD for ceramic membranes can have some specific advantages as they have listed below:

- i. Previously reported experimental data could be accurately reproduced. Furthermore, they are in good agreement between experimental observations and simulation results via CALPHAD. Accordingly, results from the CALPHAD approach can be reliable for ceramic membranes systems.
- ii. The focus of the approach can be directed toward temperatures and atmospheric pressures where ceramic membranes are either fabricated or processed.
- iii. The CALPHAD approach can investigate multicomponent systems. It enables us to examine the stability of a wide range of compositions for perovskite and fluorite phases and narrow down on only several candidate compositions.
- iv. In the CALPHAD approach, database optimizations are made where experimental information is available, mainly on low-order binary. After optimizing databases, they can be employed for a high-order system where experimental data are rare or missing. Owing to this feature, the approach can be utilized to predict phase stabilities and provide thermochemical values at untouched conditions.
- v. Like other methods, the CALPHAD approach has its limitations, but optimizations can always improve its databases. It can be fed by new experimental data to enhance its databases. For this purpose, the CALPHAD approach can be employed to design upcoming experiments. New experimental results can be fed to databases to improve the quality of produced results.

In the current research, databases for several multicomponent systems have been deployed. The development of these databases is initially based on needs in SOFC applications. However, due to similarities between SOFC and ceramic membranes, they can be successfully used for ceramic membrane systems. These databases have been shortly re-addressed in the following parts. Further information about their Thermodynamic models can be found in original publications.

1.1. $\text{La}_2\text{O}_3\text{-SrO-Mn}_2\text{O}_3\text{-Cr}_2\text{O}_3$ system

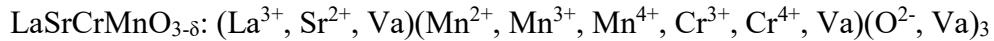
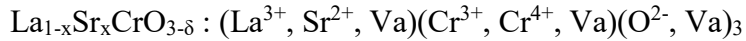
The system has been developed by Povoden-Karadeniz et al. for symmetrical SOFC applications [19]. The research presents thermodynamic models for solid oxide phases and Gibbs

energy functions for compositions of SrCrO₄, Sr_{2.67}Cr₂O₈, and Sr₂CrO₄. It can also re-produced experimental data for solid solubilities and nonstoichiometry in La_{1-x}Sr_xCrO_{3-δ} and LaMn_{1-x}Cr_xO_{3-δ}.

The sublattice models (Sr²⁺)(Cr⁶⁺)(O²⁻)₄ and (Sr²⁺)(Cr³⁺)₂(O²⁻)₄ have been considered for SrCrO₄ and SrCr₂O₄. For Sr_{2.67}Cr₂O₈, and Sr₂CrO₄, two sublattices of (Sr²⁺)_{8/3}(Va)_{1/3}(Cr⁶⁺)_{2/3}(O²⁻)_{8/3}(Cr⁵⁺)_{4/3}(O²⁻)_{16/3} and (Sr²⁺)(O²⁻)₁(Sr²⁺)(Cr⁴⁺)(O²⁻)₃ have been chosen, respectively. Perovskite phase has been described as (A,Va)(B,Va)(O²⁻,Va)₃ with using compound energy formalism (CEF) and the concept of reciprocal reactions [20]. Based on this, the molar Gibbs energy for perovskite phases of the system has been proposed as below:

$${}^{\circ}G_m^{\text{prv}} = \sum_i \sum_j \sum_k y_i y_j y_k {}^{\circ}G_{i;j;k} + RT \left(\sum_i y_i \ln y_i + \sum_j y_j \ln y_j + 3 \sum_k y_k \ln y_k + \right) + E_G^{\text{prv}}$$

where y_i is the site fraction of species i in sublattices and E_G^{prv} is the excess Gibbs energy of the perovskite phase. Based on this model, three different sublattices have been chosen for LaSrCrO_{3-δ}, LaMnCrO_{3-δ}, and LaSrCrMnO_{3-δ} as they have listed below:



The proposed model in this study allows the quantitative calculation of defects as a function of temperature, composition, and oxygen partial pressure. In the case of the stability of phases, the model is sufficiently in agreement with Thermodynamic phase diagrams. Hence, it can provide valuable information about the durability of SOFC materials under working conditions. Further information about optimized parameters and Thermodynamic models can be found in the original publication [19].

1.2.La-Fe-O System

This system has been modeled for La-Fe and La-Fe-O with considering oxygen and La and Fe mutual solubilities in body-centered cubic (BCC) and face-centered cubic (FCC) structures of

metallic phases [21]. The primary purpose of this development is to investigate the stability of lanthanum ferrite perovskites as cathode materials for SOFC applications. The proposed model has been deployed for defect chemistry and oxygen nonstoichiometry analysis by using CEF.

The liquid phase has been modeled with a two-sublattice model for ionic liquids. The two-sublattice ionic liquid model $(\text{Fe}^{2+}, \text{Fe}^{3+})_p(\text{O}^{2-}, \text{Va}^q)_q$ has been adopted based on the Thermodynamic assessment on the Cr-Fe-O system by Taylor and Dinsdale [22]. To model the perovskite phase, the sublattice of $(\text{La}^{3+}, \text{Va})(\text{Fe}^{2+}, \text{Fe}^{3+}, \text{Fe}^{4+}, \text{Va})(\text{O}^{2-}, \text{Va})_3$ has been considered to evaluate nonstoichiometry. Different Gibbs energy descriptions have been considered for low temperature orthorhombic (o-prv) and high temperature rhombohedral (r-prv) perovskite phases. Furthermore, the contribution of magnetic order-disorder transition has been added to Gibbs energy descriptions.

The proposed model in this study can successfully re-generate oxygen nonstoichiometry changes with temperature and oxygen partial pressure, orthorhombic \leftrightarrow rhombohedral phase transition, and magnetic order-disorder transition. It also provides thermochemical information about $\text{LaFe}_{12}\text{O}_{19}$ phase for the first time.

1.3. Cr-O System

The use of interconnect materials with Cr-base alloy in SOFC can result in degradation of their cathode due to diffusion on Cr from the interconnect material into strontium-doped lanthanum magnetite (LSM) as the cathode. Hence, the influence of Cr on this type of materials needs to be examined. This is the main motive to thermodynamically re-assess the Cr-O system. In this study, the Cr-O system has been re-assessed with new experimental data. Nonstoichiometry in $\text{Cr}_2\text{O}_{3-\delta}$ has been described by using CEF [23].

Its sublattice has been modeled as $(\text{Cr}^{2+}, \text{Cr}^{3+})_2(\text{Cr}^{3+}, \text{Va})_1(\text{O}^{2-})_3$. The liquid phase, magnetic transition, and the formation of Cr_3O_4 as a stoichiometric phase have also been considered. The proposed model can describe available Thermodynamic data and phase diagrams; however, it requires further experimental data on the miscibility gap in the liquid phase.

1.4. La-Mn-Y-Zr-O, Y-Zr-O, and La-Sr-Mn-O Systems

Due to similarities, in this thesis, CALPHAD assessments on La-Mn-Y-Zr-O and La-Sr-Mn-O systems have been examined for investigations into phase stabilities of single-phase LSCrF perovskites and dual-phase composites of LSCrF and YSZ. There are similar phases, such as $\text{La}_2\text{Zr}_2\text{O}_7$ (abbr. LZO) and SrZrO_3 (abbr. SZO) in both LSCrF-YSZ and LSM-YSZ systems, which their phase stabilities have been considered based on previous studies for LSM-YSZ.

A valuable Thermodynamic assessment on the La-Sr-Mn-O system has been conducted by Grundy [24]. The purpose of this assessment is to extend knowledge for state-of-the-art cathodes for SOFC. It has been started with the optimization of binary systems of La-O and Mn-O. His work has been extended to the La-Sr-O system by performing both experiments and optimizations. The results have been used for ternary systems of La-Mn-O and Sr-Mn-O, and then finally the La-Sr-Mn-O system has been developed. The proposed sublattice model is $(\text{La}^{3+}, \text{Sr}^{2+}, \text{Mn}^{3+}, \text{Va})(\text{Mn}^{2+}, \text{Mn}^{3+}, \text{Mn}^{4+}, \text{Va})(\text{O}^{2-}, \text{Va})_3$ with considering anti-site of Mn ion species on A-site. Grundy's database can successfully re-produce phase diagrams while it presents a good match with experimental data. It also provides reliable simulations on defect analysis with changes in temperature and oxygen partial pressure.

The original database for La-Mn-Y-Zr-O has been developed by Chen [25]. He developed Thermodynamic descriptions for the La-Mn-Y-Zr-O system through ideal extrapolations of subsystems of La-Mn-Y-Zr-O, Mn-Y-Zr-O, La-Zr-O, La-Y-O, Mn-Zr-O, Mn-Y-O, La-Mn-O, and Mn-Y-Zr. By applying the same approach, the La-Mn-Y-Zr-O database has been expanded to La-Sr-Mn-Y-O-Zr [26].

Likewise, La-Mn-Y-Zr-O, the database for Zr-Y-O, has been assessed by Chen [25]. In his database, he has provided Gibbs energy descriptions for monoclinic, tetragonal, and cubic phases of ZrO_2 , $\alpha\text{-Y}_2\text{O}_3$, $\beta\text{-Y}_2\text{O}_3$, solid solution of $\text{Zr}_3\text{Y}_4\text{O}_{12}$, and the liquid phase. The sublattice model for ZrO_2 phases is $(\text{Y}^{3+}, \text{Zr}^{4+})_1(\text{O}^{2-}, \text{Va})_2$. Here is the description of Gibbs energy for the cubic, monoclinic, and tetragonal solution phases:

$$G_m = y_{\text{Y}^{3+}}y_{\text{O}^{2-}} \overset{\circ}{G}_{\text{Y}^{3+}\text{O}^{2-}} + y_{\text{Zr}^{4+}}y_{\text{O}^{2-}} \overset{\circ}{G}_{\text{Zr}^{4+}\text{O}^{2-}} + y_{\text{Y}^{3+}}y_{\text{Va}} \overset{\circ}{G}_{\text{Y}^{3+}\text{Va}} + y_{\text{Zr}^{4+}}y_{\text{Va}} \overset{\circ}{G}_{\text{Zr}^{4+}\text{Va}} + RT[y_{\text{Y}^{3+}}\ln y_{\text{Y}^{3+}} + y_{\text{Zr}^{4+}}\ln y_{\text{Zr}^{4+}} + 2(y_{\text{O}^{2-}}\ln y_{\text{O}^{2-}} + y_{\text{Va}}\ln y_{\text{Va}})] + {}^E G_m$$

Where y_i is the fraction of the species i in a particular sublattice. Further information about Gibbs energies of other phases, interaction parameters, etc. can be found in Chen's thesis and Asadikiya's papers [27, 28].

1.5. La-Sr-Cr-Fe-Ar-H-O and La-Sr-Cr-Fe-O-H-Ar-Zr-Y-O Systems

In the current study, the focus is on La-Sr-Cr-Fe-O and its perovskite phases. Accordingly, a database on La-Sr-Cr-Fe-O has been utilized to examine the stability of the perovskite phase with changes in temperature, oxygen partial pressure, and composition [29]. Instead of assessing the whole sub-systems, this database has been merged with previously available databases as they have been introduced above. Since experimental tests have been conducted under wet forming gases (4% and 0.1% H₂-Ar) and pure Ar gas, Gibbs energy terms from SSUB-5 have been added for H and Ar [30].

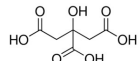
2. Experimental Approach

This part includes information about raw materials, synthesis procedures, and implementation of the experimental setup. An experimental approach has been conducted in three different sections. The first section has been dedicated to synthesizing LSCrF perovskite composition. The second section explains sample preparations for bulk sintering and stability tests. The third section includes the design and implementation of stability tests under controlled atmospheric conditions at elevated temperatures. Details of each part have been explained separately as below.

2.1. Synthesis

Different compositions of LSCrF perovskite has been synthesized by the Sol-Gel synthesis, wet chemical, and Pechinic methods [31-36]. Nitrate salts of La, Sr, Cr, and Fe have been provided from Sigma-Aldrich, Inc. Table 2-1 shows information about raw materials for the synthesis procedure. The La: Sr and Cr: Fe ratios and A-site deficiency in a final perovskite structure have been carefully controlled through the precise measuring of original raw materials and controlling their ratios in solutions batches.

Table 2-1. The list of raw materials for the Sol-Gel synthesis procedure.

Raw Materials	Formula	CAS Number
Lanthanum (III) nitrate hexahydrate	La(NO ₃) ₃ .6H ₂ O	10277-43-7
Chromium (III) nitrate nonahydrate	Cr(NO ₃) ₃ .9H ₂ O	7789-02-8
Iron (III) nitrate nonahydrate	Fe(NO ₃) ₃ .9H ₂ O	7782-61-8
Strontium nitrate	Sr(NO ₃) ₂	10042-76-9
Ethylene glycol	HOCH ₂ CH ₂ OH	107-21-1
Citric Acid		77-92-9

The processes of forming sol and its conversion to gel have been carefully examined so that no precipitations can be formed during the two stages. Dried gels have been calcinated in a box furnace at 900°C under air for 4 hours to remove organic compounds. The remaining powders have been sintered at 1100°C under ambient air for 4 hours. The sintering temperature has been chosen as no secondary phases can be formed. The flowchart summarized the whole Sol-Gel process (Figure 2-2).

Based on this method three different compositions of (La_{0.8}Sr_{0.2})_{0.98}Cr_{0.7}Fe_{0.3}O₃ (LSCrF73), (La_{0.8}Sr_{0.2})_{0.98}Cr_{0.5}Fe_{0.5}O₃ (LSCrF55), and (La_{0.8}Sr_{0.2})_{0.98}Cr_{0.3}Fe_{0.7}O₃ (LSCrF37) have been prepared. The quality of all perovskite compositions has been examined by XRD.

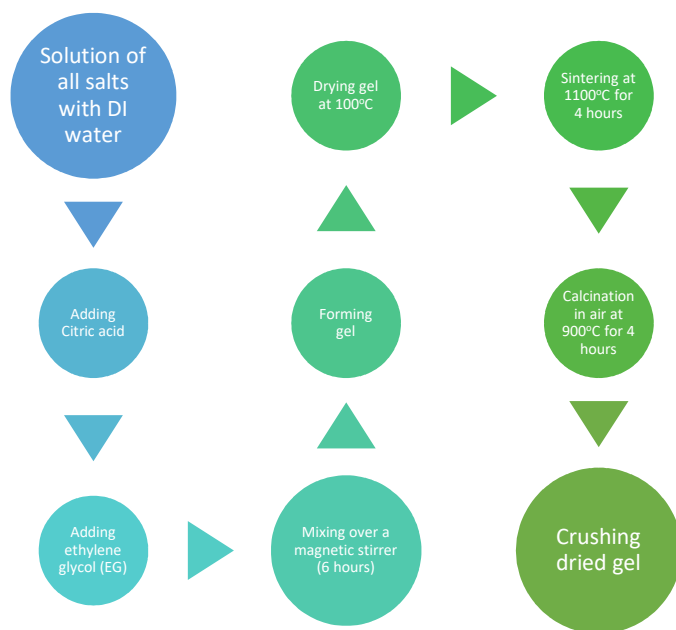


Figure 2-2. Flowchart for the Sol-Gel synthesis procedure.

2.2. Sample Preparation

Synthesized and as-received powders have been pressed by an isostatic press up to 12 torr. The diameter of the pressing die is 12.7 mm (1/2 inches).

Dual-Phase composite samples of LSCF and 8%(Y₂O₃)-ZrO₂ (yttria-stabilized Zirconia, 8YSZ), 10Sc1CeSZ (Scandia-doped Ceria stabilized Zirconia), and 10Sc1YSZ (Scandia-doped yttria-stabilized zirconia) have been prepared by mechanical mixing of two powders with equal weight ratios. The Saint-Gobain ZirPro ceramic grinding media (Zirmil®Y) has been used during milling. The milling for each composition has been proceeded for at least 6 hours. Similar sizes of pellets have been prepared after removing the grinding media. Thermal treatments include pre-sinter and stability test procedures for the dual-phase composites. They are like the single-phase perovskite samples.

The thickness of pellets for both single and dual-phase samples is less than 1 mm after sintering. The below picture shows one of the pellets for dual-phase composite samples (Figure 2-3).



Figure 2-3. A pellet of a dual-phase composite sample after sintering at 1150°C for 2 hours under air.

2.3. Stability Tests

The stability tests have been conducted in tube furnaces with different atmospheres and at elevated temperatures. The tube furnace is a 1500°C three-zone split tube furnace with ± 1 °C accuracy from MTI corporation. It has three zones with 200 mm/ each length, as its total heating zone is 600 mm. The used tubes include alumina and mullite tubes with 82 and 84 inches for outer diameter.

The applied thermal programs include heating up to 100°C, hold for 60 min to remove moisture in samples, and heating up to final temperatures. The final temperatures are 850 and 1400°C. The holding time for all temperatures is 10 hours. Due to the technical limits of the furnace, the heating rate for all stability and sintering procedures is 5 °C/min. The fast cooling procedure consists of taking out samples at high temperatures at the end of their holding times and keep them on a cold alumina wafer.

The utilized atmospheres include ambient air, Argon (99.999%, Grade: Ultra High Purity), forming gas #1 (4% H_2 -balanced via Ar) with $\pm 0.2\%$ analytical error for hydrogen, forming gas #2 (0.1% H_2 -balanced via Ar). All gases have been provided through Airgas, an Air Liquide Company. Before introducing forming gases into the furnace, they have passed through deionized water (DI water). This has been designed through the installment of a humidity bottle between gas cylinders and the furnace. The humidity inside tubes has then been controlled by controlling the temperature of the humidity bottle. As the temperature of the humidity bottle increases, more water vapor can be delivered to the furnace with gases. Further information about this method can be found in this

reference [37]. Oxygen partial pressure ($p(\text{O}_2)$) inside the tube of the furnace has been constantly monitored by Rapidox 2100 Gas Analyzer. The below picture shows one of these setups (Figure 2-4).



Figure 2-4. Experimental setup for heat treatment and stability tests.

2.4. Materials Characterizations

Chemical stability and crystal symmetries of samples have been examined by the X-ray diffraction method before and after thermal treatments. The collected spectra have been later refined by the Rietveld refinement method via HighScore Plus (version 4.8). The quality of produced spectra has been controlled by X-ray optics. Only high-quality patterns have been refined by the Rietveld method.

Phase quantities of different phases and changes in crystal symmetries and lattice parameters have been examined with the use of the Rietveld refinement method. The implement of the method has been handled by the HighScore Plus software. XRD reference cards have been provided by using the ICDD database. Phase refinement procedure has been started with the use of reference cards as their elemental contents and Wyckoff positions have been considered for the refinement. Besides, their site fractions of atoms have been modified based on sintered samples. However, Site fractions and atomic coordination have not been refined in this study. The refinement procedure has been conducted by applying a cluster analysis profile, which enables us to refine several patterns with different phases fast. It has been applied for background, zero shift, specimen displacement, lattice parameters, wave functions, and asymmetrical parameters. The

accuracy and validity of refined parameters have been double-checked based on available literature and reliability factors.

Based on refined results, new XRD reference cards have been produced for both perovskite and fluorite phases, which later have been utilized to refine structures after stability tests. The below tables show the reference structures for initial perovskite, fluorite, and secondary phases (Table 2-2).

Table 2-2. Reference structures for fluorite, perovskite, and secondary phases.

8YSZ		ICDD Card Number: 01-077-2286					
Radiation: CuK α 1 (1.5406 Å)		d-Spacing: Calculated		Intensity: Calculated - Peak		I/Ic: 9.91	I/Ic - CW ND: 0.9
Crystal System: Cubic		SPGR: Fm-3m (225)					
Author's Unit Cell [a: 5.1482 Å		Volume: 136.45 Å ³		Z: 4.00		MolVol: 34.11]	
Structural Density: 5.74 g/cm ³		SS/FOM: F(14) = 999.9(0.0001, 14)		R-factor: 0.035			
Space Group: Fm-3m (225)		Molecular Weight: 117.93 g/mol					
Crystal Data [a: 5.148 Å		b: 5.148 Å		c: 5.148 Å		$\alpha:$ 90.00°	
XtlCell Z: 4.00		a/b: 1.000		c/b: 1.000]		$\beta:$ 90.00°	
Reduced Cell [a: 3.640 Å		b: 3.640 Å		c: 3.640 Å		$\alpha:$ 60.00°	
						$\beta:$ 60.00°	
						$\gamma:$ 60.00°	
						RedCell Vol: 34.11 Å ³]	
Space Group Symmetry Operators:							
Seq	Operator	Seq	Operator	Seq	Operator	Seq	Operator
1	x,y,z	9	y,x,z	17	y,-z,-x	25	-x,y,-z
2	-x,-y,-z	10	-y,-x,-z	18	-y,z,x	26	x,-y,z
3	z,x,y	11	z,y,x	19	x,-z,-y	27	-z,x,-y
4	-z,-x,-y	12	-z,-y,-x	20	-x,z,y	28	z,-x,y
5	y,z,x	13	x,-y,-z	21	y,-x,-z	29	-y,z,-x
6	-y,-z,-x	14	-x,y,z	22	-y,x,z	30	y,-z,x
7	x,z,y	15	z,-x,-y	23	z,-y,-x	31	-x,z,-y
8	-x,-z,-y	16	-z,x,y	24	-z,y,x	32	x,-z,y
						33	-y,x,-z
						34	y,-x,z
						35	-z,y,-x
						36	z,-y,x
						37	-x,-y,z
						38	x,y,-z
						39	-z,-x,y
						40	z,x,-y
						41	-y,-z,x
						42	y,z,-x
						43	-x,-z,y
						44	x,z,-y
						45	-y,-x,z
						46	y,x,-z
						47	-z,-y,x
						48	z,y,-x
ADP Type: B							
Atomic Coordinates:							
Atom	Num	Wyckoff	Symmetry	x	y	z	SOF
Zr	1	4a		0.0	0.0	0.0	0.786
Y	2	4a		0.0	0.0	0.0	0.214
O	3	8c		0.25	0.25	0.25	0.34
O	4	48g		0.3	0.25	0.25	0.085
							1.43
							1.43
							1.15
							1.15
Crystal (Symmetry Allowed): Centrosymmetric							
AC Space Group: FM3-M (225)							
AC Unit Cell [a: 5.1482 Å							
b: 5.1482 Å							
c: 5.1482 Å							
$\alpha:$ 90°							
$\beta:$ 90°							
$\gamma:$ 90°]							

10Sc1YSZ

ICDD Card Number: 04-016-6138

Radiation: CuK α 1 (1.5406 Å) d-Spacing: Calculated Intensity: Calculated - Peak I/Ic: 9.52 I/Ic - CW ND: 1.23

Crystal System: Cubic SPGR: Fm-3m (225)

Author's Unit Cell [a: 5.089(1) Å Volume: 131.79 Å³ Z: 4.00 MolVol: 32.95] Calculated Density: 6.004 g/cm³
Structural Density: 6 g/cm³ SS/FOM: F(14) = 999.9(0.0001, 14)

Space Group: Fm-3m (225) Molecular Weight: 119.13 g/mol

Crystal Data [a: 5.089 Å b: 5.089 Å c: 5.089 Å α : 90.00° β : 90.00° γ : 90.00° XtlCell Vol: 131.79 Å³
XtlCell Z: 4.00 a/b: 1.000 c/b: 1.000]Reduced Cell [a: 3.598 Å b: 3.598 Å c: 3.598 Å α : 60.00° β : 60.00° γ : 60.00° RedCell Vol: 32.95 Å³]

Space Group Symmetry Operators:

Seq	Operator	Seq	Operator	Seq	Operator	Seq	Operator	Seq	Operator	Seq	Operator
1	x,y,z	9	y,x,z	17	y,-z,-x	25	-x,y,-z	33	-y,x,-z	41	-y,-z,x
2	-x,-y,-z	10	-y,-x,-z	18	-y,z,x	26	x,-y,z	34	y,-x,z	42	y,z,-x
3	z,x,y	11	z,y,x	19	x,-z,-y	27	-z,x,-y	35	-z,y,-x	43	-x,-z,y
4	-z,-x,-y	12	-z,-y,-x	20	-x,z,y	28	z,-x,y	36	z,-y,x	44	x,z,-y
5	y,z,x	13	x,-y,-z	21	y,-x,-z	29	-y,z,-x	37	-x,-y,z	45	-y,-x,z
6	-y,-z,-x	14	-x,y,z	22	-y,x,z	30	y,-z,x	38	x,y,-z	46	y,x,-z
7	x,z,y	15	z,-x,-y	23	z,-y,-x	31	-x,z,-y	39	-z,-x,y	47	-z,-y,x
8	-x,-z,-y	16	-z,x,y	24	-z,y,x	32	x,-z,y	40	z,x,-y	48	z,y,-x

Atomic Coordinates:

Atom	Num	Wyckoff	Symmetry	x	y	z	SOF	IDP	AET
Zr	1	4a	m-3m	0.0	0.0	0.0	0.885		
Sc	2	4a	m-3m	0.0	0.0	0.0	0.066		
Y	3	4a	m-3m	0.0	0.0	0.0	0.049		
O	4	8c	-43m	0.25	0.25	0.25	0.971		

Crystal (Symmetry Allowed): Centrosymmetric AC Space Group: Fm-3m (225)

AC Unit Cell [a: 5.089(1) Å b: 5.089(1) Å c: 5.089(1) Å α : 90° β : 90° γ : 90°]

10Sc1CeSZ

ICDD Card Number: 04-022-1613

Radiation: CuK α 1 (1.5406 Å) d-Spacing: Calculated Intensity: Calculated - Peak I/Ic: 8.8 I/Ic - CW ND: 1.12

Crystal System: Cubic SPGR: Fm-3m (225)

Author's Unit Cell [a: 5.09437(8) Å Volume: 132.21 Å³ Z: 4.00 MolVol: 33.05]
Calculated Density: 5.724 g/cm³ Structural Density: 5.72 g/cm³ SS/FOM: F(14) = 999.9(0.0001, 14)
R-factor: 0.036

Space Group: Fm-3m (225) Molecular Weight: 113.94 g/mol

Crystal Data [a: 5.094 Å b: 5.094 Å c: 5.094 Å α : 90.00° β : 90.00° γ : 90.00° XtlCell Vol: 132.21 Å³
XtlCell Z: 4.00 a/b: 1.000 c/b: 1.000]Reduced Cell [a: 3.602 Å b: 3.602 Å c: 3.602 Å α : 60.00° β : 60.00° γ : 60.00° RedCell Vol: 33.05 Å³]

Space Group Symmetry Operators:

Seq	Operator	Seq	Operator	Seq	Operator	Seq	Operator	Seq	Operator	Seq	Operator
1	x,y,z	9	y,x,z	17	y,-z,-x	25	-x,y,-z	33	-y,x,-z	41	-y,-z,x
2	-x,-y,-z	10	-y,-x,-z	18	-y,z,x	26	x,-y,z	34	y,-x,z	42	y,z,-x
3	z,x,y	11	z,y,x	19	x,-z,-y	27	-z,x,-y	35	-z,y,-x	43	-x,-z,y
4	-z,-x,-y	12	-z,-y,-x	20	-x,z,y	28	z,-x,y	36	z,-y,x	44	x,z,-y
5	y,z,x	13	x,-y,-z	21	y,-x,-z	29	-y,z,-x	37	-x,-y,z	45	-y,-x,z
6	-y,-z,-x	14	-x,y,z	22	-y,x,z	30	y,-z,x	38	x,y,-z	46	y,x,-z
7	x,z,y	15	z,-x,-y	23	z,-y,-x	31	-x,z,-y	39	-z,-x,y	47	-z,-y,x
8	-x,-z,-y	16	-z,x,y	24	-z,y,x	32	x,-z,y	40	z,x,-y	48	z,y,-x

ADP Type: U

Atomic Coordinates:

Atom	Num	Wyckoff	Symmetry	x	y	z	SOF	Uiso	AET
Zr	1	4a	m-3m	0.0	0.0	0.0	0.81	0.0167	
Sc	2	4a	m-3m	0.0	0.0	0.0	0.18	0.0167	
Ce	3	4a	m-3m	0.0	0.0	0.0	0.01	0.0167	
O	4	8c	-43m	0.25	0.25	0.25	0.953	0.0327	

Crystal (Symmetry Allowed): Centrosymmetric AC Space Group: Fm-3m (225)

AC Unit Cell [a: 5.09437(8) Å b: 5.09437(8) Å c: 5.09437(8) Å α : 90° β : 90° γ : 90°]

(La,Sr)(Cr,Fe)O_{3-δ} (Rhombohedral)**ICDD Card Number: 04-013-5267****Radiation:** CuKα1 (1.5406 Å) **d-Spacing:** Calculated **Intensity:** Calculated - Peak **I/Ic:** 4.92 **I/Ic - CW ND:** 0.68**Crystal System:** Rhombohedral **SPGR:** R-3c (167)
Author's Unit Cell [a: 5.4973(1) Å c: 13.4088(2) Å **Volume:** 350.93 Å³ **Z:** 6.00 **MolVol:** 58.49 c/a: 2.439]
Calculated Density: 5.996 g/cm³ **Structural Density:** 6 g/cm³ **SS/FOM:** F(30) = 331.1(0.0028, 32)
R-factor: 0.025**Space Group:** R-3c (167) **Molecular Weight:** 211.21 g/mol
Crystal Data [a: 5.497 Å b: 5.497 Å c: 13.409 Å α: 90.00° β: 90.00° γ: 120.00° **XtlCell Vol:** 350.93 Å³
XtlCell Z: 6.00 c/a: 2.439 a/b: 1.000 c/b: 2.439]
Reduced Cell [a: 5.482 Å b: 5.482 Å c: 5.482 Å α: 60.19° β: 60.19° γ: 60.19° **RedCell Vol:** 116.98 Å³]**Warning: Metric Symmetry Exceeds Crystal Symmetry** **Warning: Metric Symmetry Exceeds Crystal Symmetry****Crystal Data Bravais Lattice =** RH **Reduced Cell Bravais Lattice =** CF **Matrix (Initial To CF):** 1.3 0.7-0.3/-0.7-1.3-0.3/-0.7 0.7-0.3
CF Cell Parameters: 7.763 7.763 7.763 90.16 90.16 90.16**Space Group Symmetry Operators:**

Seq	Operator	Seq	Operator	Seq	Operator	Seq	Operator
1	x,y,z	4	y,-x+y,-z	7	-y,-x,z+1/2	10	-x,-x+y,-z+1/2
2	-x,-y,-z	5	-x+y,-x,z	8	y,x,-z+1/2	11	-x+y,y,z+1/2
3	-y,x-y,z	6	x-y,x,-z	9	x,x-y,z+1/2	12	x-y,-y,-z+1/2

Atomic Coordinates:

Atom	Num	Wyckoff	Symmetry	x	y	z	SOF	IDP	AET
Sr	1	6a	32	0.0	0.0	0.25	0.6		
La	2	6a	32	0.0	0.0	0.25	0.4		
Fe	3	6b	-3.	0.0	0.0	0.0	0.8		
Cr	4	6b	-3.	0.0	0.0	0.0	0.2		
O	5	18e	.2	0.529	0.0	0.25	1.0		

Crystal (Symmetry Allowed): Centrosymmetric **AC Space Group:** R-3cH (167)
AC Unit Cell [a: 5.4973(1) Å b: 5.4973(1) Å c: 13.4088(2) Å α: 90° β: 90° γ: 120°]**(La,Sr)(Cr,Fe)O_{3-δ}****ICDD Card Number: 04-013-5265****Radiation:** CuKα1 (1.5406 Å) **d-Spacing:** Calculated **Intensity:** Calculated - Peak **I/Ic:** 7.55 **I/Ic - CW ND:** 0.36**Crystal System:** Orthorhombic **SPGR:** Pnma (62)
Author's Unit Cell [a: 5.5212(1) Å b: 7.8080(2) Å c: 5.5464(1) Å **Volume:** 239.10 Å³ **Z:** 4.00
MolVol: 59.77 c/a: 1.005 a/b: 0.707 c/b: 0.710] **Calculated Density:** 6.437 g/cm³
Structural Density: 6.44 g/cm³ **SS/FOM:** F(30) = 137.3(0.0055, 40) **R-factor:** 0.029**Space Group:** Pcnm (62) **Molecular Weight:** 231.72 g/mol
Crystal Data [a: 5.546 Å b: 7.808 Å c: 5.521 Å α: 90.00° β: 90.00° γ: 90.00° **XtlCell Vol:** 239.10 Å³
XtlCell Z: 4.00 c/a: 0.995 a/b: 0.710 c/b: 0.707]
Reduced Cell [a: 5.521 Å b: 5.546 Å c: 7.808 Å α: 90.00° β: 90.00° γ: 90.00° **RedCell Vol:** 239.10 Å³]**Space Group Symmetry Operators:**

Seq	Operator	Seq	Operator	Seq	Operator	Seq	Operator
1	x,y,z	3	x+1/2,-y+1/2,-z+1/2	5	-x,y+1/2,-z	7	-x+1/2,-y,z+1/2
2	-x,-y,-z	4	-x+1/2,y+1/2,z+1/2	6	x,-y+1/2,z	8	x+1/2,y,-z+1/2

Atomic Coordinates:

Atom	Num	Wyckoff	Symmetry	x	y	z	SOF	IDP	AET
La	1	4c	.m.	0.0174	0.25	-0.0042	0.8		
Sr	2	4c	.m.	0.0174	0.25	-0.0042	0.2		
Fe	3	4b	-1	0.0	0.0	0.5	0.8		
Cr	4	4b	-1	0.0	0.0	0.5	0.2		
O	5	8d	1	0.265	0.0261	0.723	1.0		
O	6	4c	.m.	0.495	0.25	0.075	1.0		

Crystal (Symmetry Allowed): Centrosymmetric **AC Space Group:** Pnma (62)
AC Unit Cell [a: 5.5212(1) Å b: 7.8080(2) Å c: 5.5464(1) Å α: 90° β: 90° γ: 90°]

LaFeO_{3-δ} (Orthorhombic)

ICDD Card Number: 01-084-6534

Radiation: CuKα1 (1.5406 Å) d-Spacing: Calculated Intensity: Calculated - Peak I/Ic: 8.11 I/Ic - CW ND: 0.43

Crystal System: Orthorhombic SPGR: Pbnm (62)
 Author's Unit Cell [a: 5.542(2) Å b: 5.5596(2) Å c: 7.8561(9) Å Volume: 242.06 Å³ Z: 4.00
 MolVol: 60.52 c/a: 1.418 a/b: 0.997 c/b: 1.413] Calculated Density: 6.661 g/cm³
 Structural Density: 6.658 g/cm³ SS/FOM: F(30) = 29.2(0.0184, 56) R-factor: 0.058

Space Group: Pnma (62) Molecular Weight: 242.75 g/mol
 Crystal Data [a: 5.560 Å b: 7.856 Å c: 5.542 Å α: 90.00° β: 90.00° γ: 90.00° XtlCell Vol: 242.06 Å³
 XtlCell Z: 4.00 c/a: 0.997 a/b: 0.708 c/b: 0.705]
 Reduced Cell [a: 5.542 Å b: 5.560 Å c: 7.856 Å α: 90.00° β: 90.00° γ: 90.00° RedCell Vol: 242.06 Å³]

Atomic parameters are cross-referenced from PDF entry 04-011-7994

Space Group Symmetry Operators:

Seq	Operator	Seq	Operator	Seq	Operator	Seq	Operator
1	x,y,z	3	x+1/2,-y+1/2,-z+1/2	5	-x,y+1/2,-z	7	-x+1/2,-y,z+1/2
2	-x,-y,-z	4	-x+1/2,y+1/2,z+1/2	6	x,-y+1/2,z	8	x+1/2,y,-z+1/2

ADP Type: B

Atomic Coordinates:

Atom	Num	Wyckoff	Symmetry	x	y	z	SOF	Biso	AET
La	1	4c	.m.	0.028	0.25	-0.007	1.0	0.5	
Fe	2	4b	-1	0.0	0.0	0.5	1.0	0.26	
O	3	4c	.m.	0.488	0.25	0.066	1.0	0.6	
O	4	8d	1	0.287	0.465	-0.284	1.0	0.55	

Crystal (Symmetry Allowed): Centrosymmetric AC Space Group: Pnma (62)
 AC Unit Cell [a: 5.5594(4) Å b: 7.8498(7) Å c: 5.5509(5) Å α: 90° β: 90° γ: 90°]

SrZrO₃ (SZO)

ICDD Card Number: 01-076-0167

Radiation: CuKα1 (1.5406 Å) d-Spacing: Calculated Intensity: Calculated - Peak I/Ic: 11.45
 I/Ic - CW ND: 0.57

Crystal System: Cubic SPGR: Pm-3m (221)
 Author's Unit Cell [a: 4.094(2) Å Volume: 68.62 Å³ Z: 1.00 MolVol: 68.62] Calculated Density: 5.489 g/cm³
 Structural Density: 5.49 g/cm³ SS/FOM: F(23) = 999.9(0.0001, 23)

Space Group: Pm-3m (221) Molecular Weight: 226.84 g/mol
 Crystal Data [a: 4.094 Å b: 4.094 Å c: 4.094 Å α: 90.00° β: 90.00° γ: 90.00° XtlCell Vol: 68.62 Å³
 XtlCell Z: 1.00 a/b: 1.000 c/b: 1.000]
 Reduced Cell [a: 4.094 Å b: 4.094 Å c: 4.094 Å α: 90.00° β: 90.00° γ: 90.00° RedCell Vol: 68.62 Å³]

Atomic parameters are cross-referenced from PDF entry 04-001-7315

Space Group Symmetry Operators:

Seq	Operator	Seq	Operator	Seq	Operator	Seq	Operator	Seq	Operator
1	x,y,z	9	y,x,z	17	y,-z,-x	25	-x,y,-z	33	-y,x,-z
2	-x,-y,-z	10	-y,-x,-z	18	-y,z,x	26	x,-y,z	34	y,-x,z
3	z,x,y	11	z,y,x	19	x,-z,-y	27	-z,x,-y	35	-z,y,-x
4	-z,-x,-y	12	-z,-y,-x	20	-x,z,y	28	z,-x,y	36	z,-y,x
5	y,z,x	13	x,-y,-z	21	y,-x,-z	29	-y,z,-x	37	-x,-y,z
6	-y,-z,-x	14	-x,y,z	22	-y,x,z	30	y,-z,x	38	x,y,-z
7	x,z,y	15	z,-x,-y	23	z,-y,-x	31	-x,z,-y	39	-z,-x,y
8	-x,-z,-y	16	-z,x,y	24	-z,y,x	32	x,-z,y	40	z,x,-y

Atomic Coordinates:

Atom	Num	Wyckoff	Symmetry	x	y	z	SOF	IDP	AET
Sr	1	1a	m-3m	0.0	0.0	0.0	1.0		12-b
Zr	2	1b	m-3m	0.5	0.5	0.5	1.0		6-a
O	3	3c	4/mmm	0.0	0.5	0.5	1.0		2#b

Crystal (Symmetry Allowed): Centrosymmetric AC Space Group: Pm-3m (221)
 AC Unit Cell [a: 4.088 Å b: 4.088 Å c: 4.088 Å α: 90° β: 90° γ: 90°]

Spinel

ICDD Card Number: 01-0844061

Radiation: CuKα1 (1.5406 Å) d-Spacing: Calculated Intensity: Calculated - Peak I/Ic: 4.79 I/Ic - CW ND: 1.08

Crystal System: Cubic SPGR: Fd-3m (227)

Author's Unit Cell [a: 8.3792(1) Å Volume: 588.31 Å³ Z: 8.00 MolVol: 73.54]

Calculated Density: 5.141 g/cm³ Structural Density: 5.14 g/cm³ SS/FOM: F(30) = 999.9(0.0001, 30)

R-factor: 0.056

Space Group: Fd-3m (227) Molecular Weight: 227.68 g/mol

Crystal Data [a: 8.379 Å b: 8.379 Å c: 8.379 Å α: 90.00° β: 90.00° γ: 90.00° XtlCell Vol: 588.31 Å³

XtlCell Z: 8.00 a/b: 1.000 c/b: 1.000]

Reduced Cell [a: 5.925 Å b: 5.925 Å c: 5.925 Å α: 60.00° β: 60.00° γ: 60.00° RedCell Vol: 147.08 Å³]

Space Group Symmetry Operators:

Seq	Operator	Seq	Operator	Seq	Operator	Seq	Operator	Seq	Operator
1	x,y,z	11	z,-x+1/4,-y+1/4	21	-y+1/4,z,-x+1/4	31	-x+1/4,-z+1/4,y	41	z,y,x
2	-x,-y,-z	12	-z,x+3/4,y+3/4	22	y+3/4,-z,x+3/4	32	x+3/4,z+3/4,-y	42	-z,-y,-x
3	x,-y+1/4,-z+1/4	13	-z+1/4,x,-y+1/4	23	-y+1/4,-z+1/4,x	33	y,x,z	43	z,-y+1/4,-x+1/4
4	-x,y+3/4,z+3/4	14	z+3/4,-x,y+3/4	24	y+3/4,z+3/4,-x	34	-y,-x,-z	44	-z,y+3/4,x+3/4
5	-x+1/4,y,-z+1/4	15	-z+1/4,-x+1/4,y	25	x,z,y	35	y,-x+1/4,-z+1/4	45	-z+1/4,y,-x+1/4
6	x+3/4,-y,z+3/4	16	z+3/4,x+3/4,-y	26	-x,-z,-y	36	-y,x+3/4,z+3/4	46	z+3/4,-y,x+3/4
7	-x+1/4,-y+1/4,z	17	y,z,x	27	x,-z+1/4,-y+1/4	37	-y+1/4,x,-z+1/4	47	-z+1/4,-y+1/4,x
8	x+3/4,y+3/4,-z	18	-y,-z,-x	28	-x,z+3/4,y+3/4	38	y+3/4,-x,z+3/4	48	z+3/4,y+3/4,-x
9	z,x,y	19	y,-z+1/4,-x+1/4	29	-x+1/4,z,-y+1/4	39	-y+1/4,-x+1/4,z		
10	-z,-x,-y	20	-y,z+3/4,x+3/4	30	x+3/4,-z,y+3/4	40	y+3/4,x+3/4,-z		

Atomic Coordinates:

Atom	Num	Wyckoff	Symmetry	x	y	z	SOF	IDP	AET
Fe	1	8a		0.125	0.125	0.125	1.0		
Fe	2	16d		0.5	0.5	0.5	0.5		
Cr	3	16d		0.5	0.5	0.5	0.5		
O	4	32e		0.259	0.259	0.259	1.0		

Crystal (Symmetry Allowed): Centrosymmetric AC Space Group: FD3-MZ (227)

AC Unit Cell [a: 8.3792(1) Å b: 8.3792(1) Å c: 8.3792(1) Å α: 90° β: 90° γ: 90°]

(La_{0.5}Zr_{0.5})O_{1.75} (LZO)

ICDD Card Number: 01-085-6856

Radiation: CuKα1 (1.5406 Å) d-Spacing: Calculated Intensity: Calculated - Peak I/Ic: 11.1 I/Ic - CW ND: 0.67

Crystal System: Cubic SPGR: Fm-3m (225)

Author's Unit Cell [a: 5.385(2) Å Volume: 156.16 Å³ Z: 4.00 MolVol: 39.04]

Calculated Density: 6.085 g/cm³ Structural Density: 6.084 g/cm³ SS/FOM: F(16) = 999.9(0.0001, 16) R-factor: 0.034

Space Group: Fm-3m (225) Molecular Weight: 143.06 g/mol

Crystal Data [a: 5.385 Å b: 5.385 Å c: 5.385 Å α: 90.00° β: 90.00° γ: 90.00° XtlCell Vol: 156.16 Å³

XtlCell Z: 4.00 a/b: 1.000 c/b: 1.000]

Reduced Cell [a: 3.808 Å b: 3.808 Å c: 3.808 Å α: 60.00° β: 60.00° γ: 60.00° RedCell Vol: 39.04 Å³]

Atomic parameters are cross-referenced from PDF entry 04-001-9196

Space Group Symmetry Operators:

Seq	Operator	Seq	Operator	Seq	Operator	Seq	Operator	Seq	Operator		
1	x,y,z	9	y,x,z	17	y,-z,-x	25	-x,y,-z	33	-y,x,-z	41	-y,-z,x
2	-x,-y,-z	10	-y,-x,-z	18	-y,z,x	26	x,-y,z	34	y,-x,z	42	y,z,-x
3	z,x,y	11	z,y,x	19	x,-z,-y	27	-z,x,-y	35	-z,y,-x	43	-x,-z,y
4	-z,-x,-y	12	-z,-y,-x	20	-x,z,y	28	z,-x,y	36	z,-y,x	44	x,z,-y
5	y,z,x	13	x,-y,-z	21	y,-x,-z	29	-y,z,-x	37	-x,-y,z	45	-y,-x,z
6	-y,-z,-x	14	-x,y,z	22	-y,x,z	30	y,-z,x	38	x,y,-z	46	y,x,-z
7	x,z,y	15	z,-x,-y	23	z,-y,-x	31	-x,z,-y	39	-z,-x,y	47	-z,-y,x
8	-x,-z,-y	16	-z,x,y	24	-z,y,x	32	x,-z,y	40	z,x,-y	48	z,y,-x

Atomic Coordinates:

Atom	Num	Wyckoff	Symmetry	x	y	z	SOF	IDP	AET
Zr	1	4a	m-3m	0.0	0.0	0.0	0.5		8-a
La	2	4a	m-3m	0.0	0.0	0.0	0.5		8-a
O	3	8c	-43m	0.25	0.25	0.25	0.875		10-a

Crystal (Symmetry Allowed): Centrosymmetric AC Space Group: Fm-3m (225)

AC Unit Cell [a: 5.394 Å b: 5.394 Å c: 5.394 Å α: 90° β: 90° γ: 90°]

La₂O₃**ICDD Card Number: 03-065-3185**

Radiation: CuK α 1 (1.5406 Å) d-Spacing: Calculated Intensity: Calculated - Peak I/Ic: 13.48
 I/Ic - CW ND: 0.54

Crystal System: Cubic SPGR: Ia-3 (206)
 Author's Unit Cell [a: 11.42 Å Volume: 1489.36 Å³ Z: 16.00 MolVol: 93.08] Calculated Density: 5.812 g/cm³
 Structural Density: 5.81 g/cm³ SS/FOM: F(30) = 999.9(0.0001, 30)

Space Group: Ia-3 (206) Molecular Weight: 325.81 g/mol
 Crystal Data [a: 11.420 Å b: 11.420 Å c: 11.420 Å α : 90.00° β : 90.00° γ : 90.00°
 XtlCell Vol: 1489.36 Å³ XtlCell Z: 16.00 a/b: 1.000 c/b: 1.000]
 Reduced Cell [a: 9.890 Å b: 9.890 Å c: 9.890 Å α : 109.47° β : 109.47° γ : 109.47° RedCell Vol: 744.68 Å³]

Space Group Symmetry Operators:

Seq	Operator	Seq	Operator	Seq	Operator	Seq	Operator	Seq	Operator	Seq	Operator
1	x,y,z	5	-x+1/2,y,-z	9	z,x,y	13	-z+1/2,x,-y	17	y,z,x	21	-y+1/2,z,-x
2	-x,-y,-z	6	x+1/2,-y,z	10	-z,-x,-y	14	z+1/2,-x,y	18	-y,-z,-x	22	y+1/2,-z,x
3	x,-y,-z+1/2	7	-x,-y+1/2,z	11	z,-x,-y+1/2	15	-z,-x+1/2,y	19	y,-z,-x+1/2	23	-y,-z+1/2,x
4	-x,y,z+1/2	8	x,y+1/2,-z	12	-z,x,y+1/2	16	z,x+1/2,-y	20	-y,z,x+1/2	24	y,z+1/2,-x

ADP Type: B**Atomic Coordinates:**

Atom	Num	Wyckoff	Symmetry	x	y	z	SOF	Biso	AET
La	1			0.97	0.0	0.25	1.0	0.5	
La	2			0.25	0.25	0.25	1.0	0.5	
O	3			0.385	0.145	0.38	1.0	0.5	

Crystal (Symmetry Allowed): Centrosymmetric AC Space Group: Ia-3 (206)
 AC Unit Cell [a: 11.4200 Å b: 11.4200 Å c: 11.4200 Å α : 90.0° β : 90.0° γ : 90.0°]

Microstructural study on samples has been conducted by Scanning Electron Microscope (SEM) (JEOL JSM-7000F) coupled with Energy-dispersive X-ray Spectroscopy (EDS) (Oxford Instrument X-MAX^N). Line scan, quantitative line scan, and map analysis have been performed on samples based on analysis needs. Sample preparation also includes using pin stubs, carbon and copper tapes, and sputter coating with Au/Pd target. The presences of Au and Pd have been removed from all EDS analysis. The cross-section microstructural analysis has been conducted on the fracture surface of pellets with a secondary electron detector.

Chapter 3 : Thermodynamic Assessment of the Chemical Stability of $(\text{La}_{0.8}\text{Sr}_{0.2})_{0.98}\text{Cr}_x\text{Fe}_{1-x}\text{O}_{3\pm\delta}$ under Oxygen Transport Membrane Fabrication and Operation Conditions

Published in Solid State Ionic, Volume 310, 1 November 2017, Pages 1-9.

Abstract

A comprehensive thermodynamic study by applying the Calculation of Phase Diagram (CALPHAD) approach on $(\text{La}_{0.8}\text{Sr}_{0.2})_{0.98}\text{Cr}_x\text{Fe}_{1-x}\text{O}_{3\pm\delta}$ ($x=0.3, 0.5, 0.7$) (LSCrF) has been carried out to investigate the effect of atmosphere, temperature, and B-site dopant concentration on phase stability, solid and liquid phase formation, and microstructural evolution in LSCrF. The simulation results for the chemical stability of LSCrF, exposed to oxygen partial pressure (PO_2) from 0.21 to 10^{-10} atm and temperature from 1000 to 1400°C, reveal the formation of solid corundum, spinel, $\text{La}_2\text{SrFe}_2\text{O}_7$, and the liquid phase. The simulations also show the chemical reactions of solid secondary phases with the liquid and perovskites under both equilibrium cooling and fast cooling conditions. The phase stabilities of the LSCrF samples under oxygen transport membrane (OTM) sintering and operation conditions are predicted. The study provides guidance on the densification enhancement of the LSCrF bulk materials during the sintering process through the control of the liquid phase concentration and the perovskite phase separation. In addition, the concerns of the release of the genotoxic carcinogens, i.e. chromium hexavalent (Cr^{6+}) gas species from LSCrF to the environment under the sintering and operation conditions are addressed for the first time.

Keywords: Iron doped lanthanum strontium, Computational thermodynamic, Phase stability, oxygen transport membrane

1. Introduction

LaCrO₃-based perovskites have been extensively used in high-temperature electrochemical systems [11, 38-41]. LaCrO₃ doped with transition metals are used as anode, cathode, and electrolyte in SOFCs and SOEC's, oxygen transport membrane (OTM), oxy-combustion of fossil fuels, syngas production [38-40, 42, 43] as these doped structures can maintain their superior properties under extreme operating conditions including elevated temperatures (>950°C), oxidizing and reducing gas atmospheres, presence of gas-phase contaminants, high carbon activity as well as simultaneous exposure to oxygen potential gradient. It is required that the perovskite maintain its high ionic-electronic conductivity, chemical and structural stability, and high oxygen flux for more than 40,000 hours [11, 44].

The general perovskite formula is represented as ABO₃, where A and B are two cations with different sizes and O (oxygen) as anion bonds to both [7]. The primary purpose of adding transition metals as A/B-site dopants to LaCrO₃-based perovskite is to tune its Physico-chemical and electrical properties such as coefficient of thermal expansion (CTE), densification, oxygen stoichiometry, electrical conductivity, and high temperature stability, out of which strontium (Sr) is one of the most common the A-site dopant [3]. The role of Fe as the B-site dopant for (La,Sr)CrO_{3±δ} has attracted a lot of attention recently owing to its ability to adjust CTE and enhance electrochemical, oxygen flux, polarization resistance, catalytic properties, and ionic conductivity [3, 45, 46].

The chemical stability of Fe-doped (La,Sr)CrO_{3±δ}, however, remains a concern during the device fabrication (densification) and the device operation (electrochemical) condition for OTM application [3, 42, 43, 45, 47]. Besides, the formation of the genotoxic carcinogens, i.e., chromium hexavalent (Cr⁶⁺) and its ability to be released to the environment during the sintering or device operating are a concern [48].

The current research presents the first comprehensive thermodynamic simulation on the (La_{0.8}Sr_{0.2})_{0.98}Cr_xFe_{1-x}O_{3±δ} (x=0.3, 0.5, and 0.7) perovskites (LSCrF) by using the CALculation of PHase Diagram (CALPHAD) approach. It considers the effects of P(O₂), temperature, and Cr:Fe ratio on the chemical stability of LSCrF. It provides a pathway to develop new LSCrF perovskite candidates for the OTM application with optimum phase stability, thermomechanical properties, and electrochemical performance.

2. Previous Investigation on the LSCrF Perovskite

The main research on $(\text{La,Sr})(\text{Cr,Fe})\text{O}_{3\pm\delta}$ perovskites has focused on improvements in the electrical properties (the mixed ionic-electronic conductivity) and electrochemical performance by varying the Fe content [42, 43, 46, 49, 50]. The increase in Fe content in B site from $x=0.3$ to 0.4 in $(\text{La}_{0.75}\text{Sr}_{0.25})_{0.95}\text{Cr}_x\text{Fe}_{1-x}\text{O}_{3\pm\delta}$ increases the oxygen site vacancies. Consequently, more chemical adsorption/desorption occurs, and oxygen ion conductivity is improved from 0.056 to 0.79 S/cm at 950°C and $P(\text{O}_2) = 10^{-17}$ atm [43, 51]. The Fe-dopant provides mixed ionic-electronic conductivities at high temperatures with increased oxygen permeation flux from 1.25×10^{-7} to 2.5×10^{-7} mol $\text{cm}^{-2}\text{s}^{-1}$ [45]. The $(\text{La}_{0.75}\text{Sr}_{0.25})\text{Cr}_x\text{Fe}_{1-x}\text{O}_{3\pm\delta}$ perovskite also shows good stability and catalytic properties for the oxidation of CH_4 [52].

The chemical stability of LSCrF is critical for all the applications as mentioned above [11]; however, there are contradictory reports on its chemical stability. While Lü et al. has reported no secondary phase being formed for $(\text{La}_{0.75}\text{Sr}_{0.25})_{0.95}\text{Cr}_{1-x}\text{Fe}_x\text{O}_{3\pm\delta}$ ($x=0.3$ and 0.4) for an investigation at 1000°C under $P(\text{O}_2)=10^{-18}$ atm [43], He et al. has reported the decomposition of $(\text{La}_{0.8}\text{Sr}_{0.2})\text{Cr}_{0.5}\text{Fe}_{0.5}\text{O}_{3\pm\delta}$ to metallic iron and some unknown phases after exposing the perovskite to undiluted H_2 gas at 950°C for 30h [45]. In a separate thermodynamic study on $(\text{La,Sr})(\text{Cr,M})_{3-\delta}$ ($\text{M}=\text{Ti, Mn, and Fe}$), oxygen nonstoichiometry, and defect analysis of $(\text{La}_{0.75}\text{Sr}_{0.25})\text{Cr}_{0.5}\text{Fe}_{0.5}\text{O}_{3-\delta}$ revealed the formation of $(\text{La,Sr})_2\text{FeO}_4$ secondary phase for LSCrF quenched at 900°C in $P(\text{O}_2)=10^{-20}$ bar [47]. Three recent publications by Gupta have also investigated the effect of the B site dopants, including Mn and Fe on the chemical stability of the LSCrM and LSCrF perovskites concerning its OTM application [53-55]. Their experimental results show the complexity of the high-temperature phase stability of the LSCrM and LSCrF perovskites. The decomposition of $(\text{La}_{0.8}\text{Sr}_{0.2})_{0.95}\text{Cr}_{0.7}\text{Fe}_{0.3}\text{O}_{3\pm\delta}$ to FeO_x and $\text{Fe}_{1+x}\text{Cr}_{2-x}\text{O}_4$ was observed at room temperature. The formation of FeO_x refers to the reduction of $\text{Fe}^{4+} \rightarrow \text{Fe}^{3+} \rightarrow \text{Fe}^{2+}$ and the exsolution of Fe^{+2} as FeO_x [56]. However, the formation mechanism of $\text{Fe}_{1+x}\text{Cr}_{2-x}\text{O}_4$ remained unclear [54]. For the first time, they could also detect the microstructure of the liquid phase, which has been formed at 1400°C under $\text{Ar-3\%H}_2\text{-3\%H}_2\text{O}$ atmosphere [54].

La-Sr-Cr-Fe-O system has been reported to show different crystal symmetries for a similar perovskite phase. Lü et al. reports a rhombohedral \leftrightarrow orthorhombic phase transition for $(\text{La}_{0.75}\text{Sr}_{0.25})_{0.95}\text{Cr}_{1-x}\text{Fe}_x\text{O}_{3-\delta}$ ($x=0.3$ and 0.4) structures after sintering at 1700°C in air, followed by

annealing at 1200°C in air and subsequently reducing at 1000°C in H₂-H₂O-N₂ atmosphere [43]. In separate research, the effect of P(O₂) on the oxygen nonstoichiometry (δ) has been investigated for (La_{0.75}Sr_{0.25})Cr_{0.5}Fe_{0.5}O_{3- δ} by thermogravimetry analysis from air to 10⁻²⁰ bar [47]. The P(O₂) at which the hysteresis behavior of oxygen nonstoichiometry (δ) is observed is below the equilibrium P(O₂) for the reaction between FeO and Fe. Hence, the hysteresis behavior of oxygen nonstoichiometry (δ) can only be related to phase separation resulting from the reduction in Fe ions under reducing atmosphere [47]. Gupta et al. have also reported two rhombohedral and cubic symmetries for (La_{0.8}Sr_{0.2})_{0.95}Cr_{0.7}Fe_{0.3}O_{3- δ} annealed at 1400°C in 10⁻¹⁰ atm [54].

Although related literature search includes critical experimental findings for the La-Sr-Cr-Fe-O system, they also raise further questions associated with the formation of secondary phases and their subsequent interactions with the LSCrF perovskite. Also, there are no data regarding the formation/decomposition temperature and P(O₂) for secondary phases and the composition change of LSCrF. Such information is critical for both the sintering and operation process of LSCrF.

Computational methods in materials science present a novel, interdisciplinary research approach, which has the potential to simulate thermal, electrical, and chemical properties in realistic situations [57-62]. The current research utilizes the CALPHAD approach for the thermodynamic investigation of the LSCrF system. Critical issues related to processing and application in OTM have been addressed, especially the overall Thermodynamic and kinetic concerns during the sintering process and the environmental concern of the release of Cr⁶⁺.

3. Computational Thermodynamic

The CALPHAD approach models complex phase equilibria in multicomponent materials through the computational coupling of phase diagrams and thermochemistry. Thermodynamic database of higher-order systems, such as ternary and quaternary systems, can be assessed based on a combination of thermodynamic data of unary/binary systems. Figure 3-1 schematically shows the flowchart of the computational steps and methods.

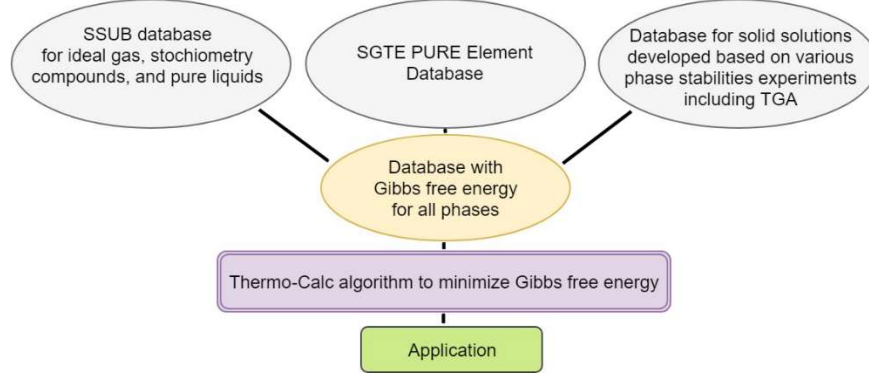


Figure 3-1. The diagram of the computational thermodynamic with using of Thermo-Calc.

a. Thermodynamic Database and Models

The database development effort has started from the La-Sr-O-H, La-Sr-Fe-O, La-Sr-Cr-O, and Cr-Fe-O systems [19, 21, 24, 63] and a five-element La-Sr-Cr-Fe-O thermodynamic database has been developed [29], which considers phase stability, stoichiometry, and defect chemistry analysis in different conditions. For instance, the perovskite was modeled with the three sublattice model:



Va stands for the vacancy.

Its Gibbs energy definition as:

$$G_m = \sum_{i,j,k} y_i y_j y_k {}^\circ G_{i;j:k}^{\text{Perov}} + RT. \left(\sum y_i \ln y_i + \sum y_j \ln y_j + 3 \sum y_k \ln y_k \right) + E_{G_m}^{\text{Perov}}$$

where y_i represents the A-site cations site fraction, y_j is the B-site cations site fraction, y_k represents the site fraction of species in the oxygen site, ${}^\circ G_m^{\text{Perov}}$ is the Gibbs energy of perovskite endmembers and $E_{G_m}^{\text{Perov}}$ is the excess Gibbs energy of the solid solution perovskite phase. The current simulation is based on 1 mole per formula of the LSCrF perovskite, i.e., 1 mole of the A-site, 1 mole of the B-site and 3 moles on the oxygen site, for a total of 5 moles of atoms for $(\text{La}_{0.8}\text{Sr}_{0.2})_{0.98}\text{Cr}_x\text{Fe}_{1-x}\text{O}_{3\pm\delta}$ ($x=0.3, 0.5, 0.7$). However, the total moles of atoms can be different from 5 due to the existence of A-site, B-site, and oxygen site deficiencies.

Also, there are two other critical stable solid solution phases from the thermodynamic simulations, i.e., spinel and corundum. Both are Cr- and Fe- rich oxides. The spinel phase is modeled with three sublattices, i.e. $(\text{Cr}^{2+}, \text{Cr}^{3+}, \text{Fe}^{2+}, \text{Fe}^{3+})_1(\text{Cr}^{3+}, \text{Fe}^{2+}, \text{Fe}^{3+}, \text{Va})_2(\text{O}^{2-})_4$, while the corundum phase is modeled with two sublattices, i.e. $(\text{Cr}^{2+}, \text{Cr}^{3+}, \text{Fe}^{3+})_2(\text{O}^{2-})_3$.

b. Current La-Sr-Cr-Fe-O + H database

To investigate the combined effect of hydrogen and oxygen on La-Sr-Cr-Fe-O system, the assessed La-Sr-Cr-Fe-O database was merged with the Scientific Group Thermodata Europe Substances Database (SSUB-5) similar to the work performed by Darvish et al. [13, 64]. The Gibbs energies of stoichiometric compounds and the gas phase from SSUB-5 were added to the La-Sr-Cr-Fe-O database.

The gas-phase has been modeled to include all the gas species in the La-Sr-Cr-Fe-O-H system from the SSUB-5 database so that it can simulate dry (4% H_2 -96%Ar) and wet (3% H_2O -4% H_2 -96%Ar) atmospheres. There is no water vapor content in the dry gas, while there is 3% water vapor in the wet gas, which is around the maximum solubility of H_2O in the air at room temperature.

c. Simulated Conditions

Several LSCrF compositions, $(\text{La}_{0.8}\text{Sr}_{0.2})_{0.98}\text{Cr}_x\text{Fe}_{1-x}\text{O}_{3\pm\delta}$ ($x=0.3, 0.5, 0.7$) have been selected to investigate the chemical stability of LSCrF under a range of oxygen partial pressure and temperature. It has been reported that the increase in Sr content in the A site improves densification [65], while too much Sr content reduces the electrical conductivity [66], flexural strength [3, 67], and CTE match with YSZ, the most commonly used solid electrolyte [66]. As a result, the Sr content in A-site is chosen at 0.2 moles in the current work. Besides, the commonly adopted 2% A-site deficiency is selected by default in the current work. The choice of the composition range for the B-site focuses on the effect of Fe on the chemical stability of the perovskite. The different compositions of LSCrF are named by their Cr:Fe ratios; for example, LSCrF-55 represents $(\text{La}_{0.8}\text{Sr}_{0.2})_{0.98}\text{Cr}_{0.5}\text{Fe}_{0.5}\text{O}_{3\pm\delta}$ ($x=0.5$). Similarly, LSCrF-37 and LSCrF-73 present $(\text{La}_{0.8}\text{Sr}_{0.2})_{0.98}\text{Cr}_{0.3}\text{Fe}_{0.7}\text{O}_{3\pm\delta}$ ($x=0.3$) and $(\text{La}_{0.8}\text{Sr}_{0.2})_{0.98}\text{Cr}_{0.7}\text{Fe}_{0.3}\text{O}_{3\pm\delta}$ ($x=0.7$), respectively. The temperature range has been chosen on the basis of the previous thermal analysis studies of $\text{La}_{0.7}\text{Sr}_{0.3}\text{Cr}_{0.5}\text{Fe}_{0.5}\text{O}_{3\pm\delta}$, which shows that there was no phase transformation in 5% H_2 - N_2 dry gas

below 950°C [51]. The focus of the current research is on the temperature range of 1000-1400°C, which covers the sintering and operation conditions.

The simulation for the formation of Cr⁶⁺ species has been carried out in dry and humid air atmospheres. Four different gas species as sources of the Cr⁶⁺ ion have been considered in the simulations, i.e., CrH₆O₆, CrO₃, CrH₄O₅, and CrH₂O₄.

4. Predictions from the Computational Thermodynamic

LSCrF-55 has been selected as the baseline in the current research. Similar investigations have been considered for LSCrF-37 and 73 with the change in temperature (1000-1400°C) and oxygen partial pressure (0.21-10⁻¹⁰atm).

a. Solid/Liquid Phase Stability at 1400°C

In the current investigation, the phase stabilities of 1 mole per formula of LSCrF at 1400°C has been simulated with the change of P(O₂) in Figure 3-2-(a), (b), and (c) for the LSCrF-37/55/73, respectively. LSCrF partially decomposes to the corundum, i.e. (Fe,Cr)₂O₃, spinel, i.e. Fe(Fe,Cr)₂O₄, La₂SrFe₂O₇, and the liquid phase at 1400°C with the reduction of P(O₂). The concentration of Fe on the B-site influences the formation of all the secondary phases; especially the formation of the liquid phase can be promoted with the increase of the Fe content. It is observed that a limited amount of corundum and spinel solid solution phases precipitate out first from LSCrF with the reduction of P(O₂) as shown in Figure 3-2. Their compositions have been calculated as shown in Table 3-1. Both phases are Fe and Cr-rich oxides, where Cr content increases with the increase of the Cr content in the initial LSCrF.

Table 3-1. The composition for the corundum ((Fe_xCr_y)₂O₃) (P(O₂)=0.1atm) and spinel (Fe(Fe,Cr)_{2-σ}O₄) phases (P(O₂)=10⁻² atm) at 1400°C for each perovskite composition.

Perovskite Samples	Phases	Corundum ((Fe _x Cr _y) ₂ O ₃)	Spinel (Fe ₁ (Fe,Cr) _{2-σ} O ₄)
LSCrF-37		(Fe _{0.9} ,Cr _{0.1}) ₂ O ₃	Fe ₁ (Fe _{0.92} ,Cr _{0.08}) _{1.84} O ₄ σ=0.03
LSCrF-55		(Fe _{0.76} ,Cr _{0.24}) ₂ O ₃	Fe ₁ (Fe _{0.74} ,Cr _{0.26}) _{1.83} O ₄ σ=0.06
LSCrF-73		(Fe _{0.53} ,Cr _{0.47}) ₂ O ₃	Fe ₁ (Fe _{0.45} ,Cr _{0.55}) _{1.81} O ₄ σ=0.07

With the further reduction of P(O₂), the spinel converts into the liquid phase. Also, further decomposition of the perovskite leads to the formation of more liquid. The formations of the liquid

phase and other solid secondary phases is in good agreement with the previous findings by Gupta et al. and He et al. [45, 53]. The composition of the liquid at 1400°C and $P(O_2) = 10^{-10}$ atm shows no Cr and mainly composed of La, Sr, and Fe (Table 3-2). It is compatible with previous scanning electron microscopy (SEM) elemental distribution mapping for $(La_{0.8}Sr_{0.2})_{0.95}Cr_{0.7}Fe_{0.3}O_{3-\delta}$ after heating at 1400°C under reducing atmosphere (Ar-3%H₂-3%H₂O) [54].

Table 3-2. The predicted composition of the liquid phase formed from LSCrF-37, 55, and 73 at 1400°C and under $P(O_2) = 10^{-10}$ atm.

Perovskite samples	Element	Liquid Phase Composition (mol.%)				
		La	Sr	Cr	Fe	O
LSCrF-37		0.15	0.08	8.51×10^{-5}	0.23	0.54
LSCrF-55		0.11	0.11	1.84×10^{-4}	0.24	0.53
LSCrF-73		0.06	0.16	5.62×10^{-4}	0.25	0.52

Another secondary phase worth noting is $La_2SrFe_2O_7$. $La_2SrFe_2O_7$ is a Ruddlesden-Popper (RP) phase, which is a form of layered perovskite structure [68]. Darvish et al. has predicted it in the La-Sr-Co-Fe-O system [13]. The physical evidence of the formation of LaSrFeO-based phases for $(La_{0.3}Sr_{0.7})Cr_{0.3}Fe_{0.7}O_{3-\delta}$ and $(La_{0.75}Sr_{0.25})Cr_{0.5}Fe_{0.5}O_{3-\delta}$ are also reported by Chen et al. and Ishi et al. in separate studies and through high-temperature in-situ XRD under reducing atmosphere [47, 69]. In the current simulation, $La_2SrFe_2O_7$ only forms in the simulation of LSCrF-37 and 55. According to Figure 3-2, its formation is dependent on the Fe content in the initial LSCrF perovskite and $P(O_2)$ range. More discussion on the chemical interaction of this phase is being addressed in **Section 5**.

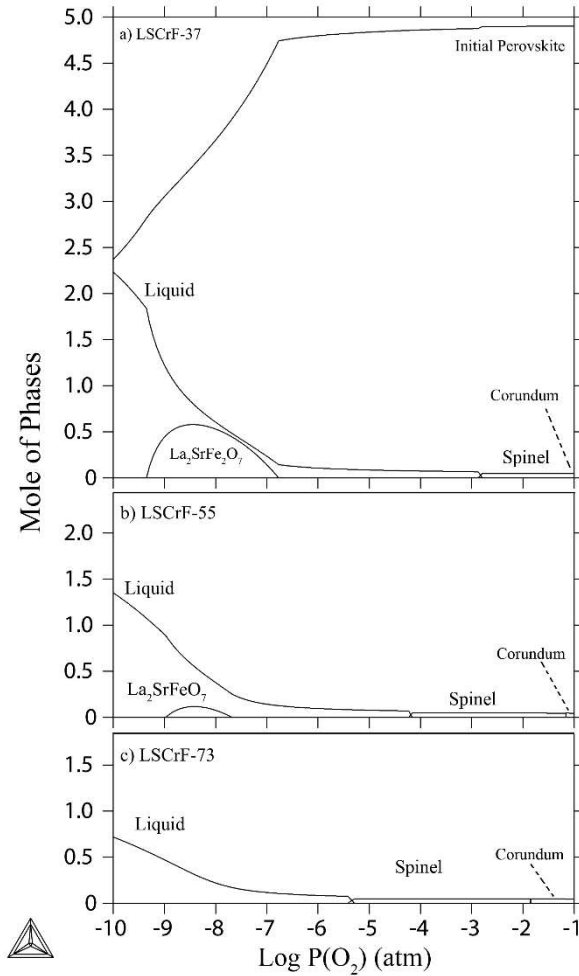


Figure 3-2. Chemical stability of a) LSCrF-37, b) LSCrF-55, and c) LSCrF-73 with reduction in $P(O_2)$ at 1400°C .

b. Thermodynamic Cooling Simulations

To simulate the phase stability of LSCrF during the cool down (decrease of temperature), the chemical stability of LSCrF at $P(O_2) = 10^{-10}$ atm was examined under both equilibrium cooling and fast cooling from 1400 to 1000°C with the assumption that the temperature range includes main phase transformations for LSCrF. Such assumption is supported by the previous thermal analysis study on $\text{La}_{0.7}\text{Sr}_{0.3}\text{Cr}_{0.5}\text{Fe}_{0.5}\text{O}_{3-\delta}$ under reducing atmospheres [51] and define cooling process boundary conditions for the La-Sr-Cr-Fe-O system. In the current work, the $P(O_2) = 10^{-10}$ atm has been chosen as the most reducing condition to study the cooling simulation. At this $P(O_2)$, there is enough liquid phase at 1400°C to show how it behaves and chemically interacts with the perovskite phase as the temperature is lowered.

i. Simulations Representing Equilibrium Cooling (Slow Cooling Rate)

Figure 3-3 shows the phase equilibria for LSCrF-37/55/73 during the cooling process from 1400 to 1000°C when $P(O_2)$ is fixed at 10^{-10} atm, and the cooling rate is defined as infinitely slow. The perovskite and the liquid phases are the only stable phases for all the three LSCrF compositions at 1400°C, indicating that a large fraction of the LSCrF perovskite phase decomposes and forms the liquid phase. Also, the formation of a much more liquid phase is observed with the increase of the Fe content in the initial LSCrF composition.

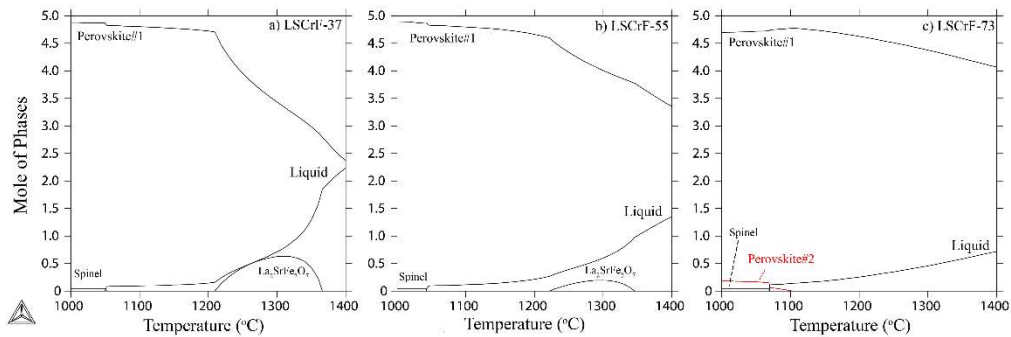


Figure 3-3. The chemical stability of a) LSCrF-37, b) LSCrF-55, and c) LSCrF-73 during equilibrium cooling at $P(O_2)=10^{-10}$ atm.

With the decrease of temperature, it is observed that the liquid phase will mainly transform back to the initial perovskite (Perovskite #1) as shown in Figure 3-3. Besides, several other solid phases will form during the cooling process. It is observed from Figure 3-3.a and b that the $La_2SrFe_2O_7$ phase becomes temporarily stable between ~ 1250 - $1350^\circ C$ for LSCrF-55 and LSCrF-37 during the cooling process. The spinel phase will precipitate from all three compositions when the temperature is lower than $1100^\circ C$. Besides, it is interesting to note that a small amount of a new perovskite structure (Perovskite #2 in Figure 3-3.c) is formed at $1100^\circ C$ besides the initial perovskite structure (Perovskite #1) during the cooling process for LSCrF-73. The compositions of these two perovskites are calculated as shown in Table 3-3. It shows Perovskite #1 has a similar composition to the starting perovskite, while Perovskite #2 is Sr and Fe rich with essentially no Cr content. It can be concluded that LSCrF-73 perovskite has a higher tendency of phase separation to form Perovskite #2. The perovskite phase separation has been briefly addressed in the literature by reporting two coexistent crystal symmetries of perovskite [43, 47, 56]. The perovskite phase separation may introduce the stress in perovskite structure due to their different CTE and volume expansion. Gupta et al. and Lü et al. pointed out that phase transitions may induce chemically

strain on redox/cooling cycling during applications and leave the effect on the thermo-physical properties of LSCrF [3, 43].

Table 3-3. The compositions of the perovskite #1,2, and 3 for LSCrF-73 at 1000°C and $P(O_2) = 10^{-10}$ atm.

Initial Perovskite Composition	Phase	Composition	δ
LSCrF-73	Perovskite #1	$La_{0.83}Sr_{0.17}Cr_{0.73}Fe_{0.27}O_{3-\delta}$	0.0002
	Perovskite #2	$La_{0.13}Sr_{0.87}FeO_{3-\delta}$	0.438
	Perovskite #3	$La_{0.65}Sr_{0.35}FeO_{3-\delta}$	0.175

ii. Simulations Representing Fast Cooling Process

The fast cooling simulation draws another boundary condition to predict the phase stability of LSCrF. The concept of the current fast cooling simulation stands close to the concept of the Scheil simulation, which is widely adopted in the cooling process of alloys [70]. It is assumed that the liquid phase at 1400°C will not have any mass exchange with the current solid perovskite phase, i.e., the solidification simulation will be carried out with only the liquid phase at 1400°C. In the present work, the compositions, as shown in Table 3-2 have been adopted as the initial liquid compositions at 1400°C. The cooling behavior from 1400 to 1000°C has been simulated as shown in Figure 3-4. $La_2SrFe_2O_7$ is the first solid phase solidifying with the decrease of temperature. It is a temporary phase and will decompose with a further reduction in temperature. The dominant solid secondary phase is Perovskite #3, along with a small amount of spinel when the temperature is below 1200°C. The composition of Perovskite #3 is also shown in Table 3-3.

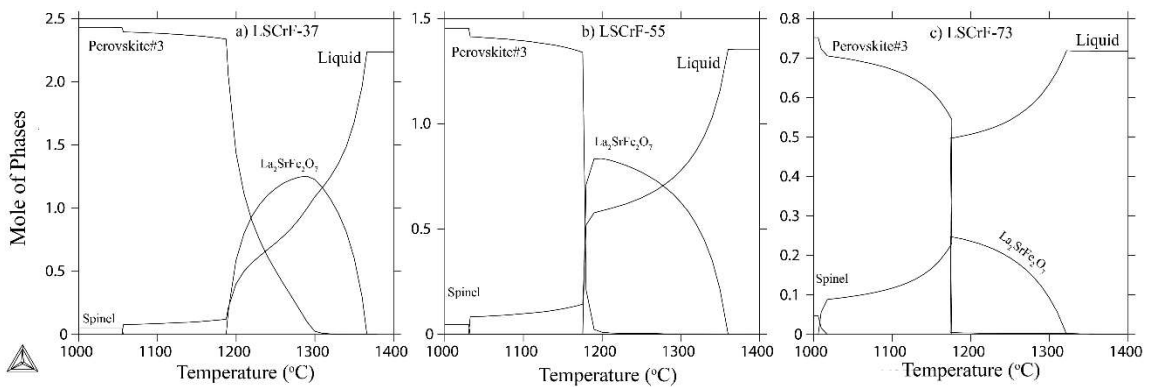


Figure 3-4. The fast cooling simulation for the liquid phase for a) LSCrF-37, b) LSCrF-55, and c) LSCrF-73 at $P(O_2)=10^{-10}$ atm.

c. Thermodynamic Equilibria with Gas

High-temperature equilibria between the solid/liquid phases with the gas phase have been simulated, including the capability of the system to release Cr^{6+} containing gas species in the presence and absence of H_2O for LSCrF-55 (Figure 3-5 and Figure 3-6). In the current database, CrO_3 is the only Cr^{6+} gas species is under dry atmosphere (Figure 3-5), while CrO_3 , CrH_2O_4 , CrH_4O_5 , and CrH_6O_6 are the Cr^{6+} gas species under wet atmosphere (Figure 3-6). Figure 5.a, b, and c represent the species concentration as a function of $P(\text{O}_2)$, temperature, and Cr concentration in LSCrF, respectively. It shows that all the Cr^{6+} species partial pressure decreases with the decrease of $P(\text{O}_2)$ (Figure 3-5.a). The partial pressure of the Cr^{6+} containing gas species vs. temperature is presented in Figure 3-5.b. The concentration of the CrH_2O_4 and CrH_4O_5 species increases as temperature decreases, while the concentration of CrO_3 declines with the reduction of temperature. The concentration of the Cr^{6+} containing gas species vs. Cr content in LSCrF is also illustrated in Figure 3-5.c.

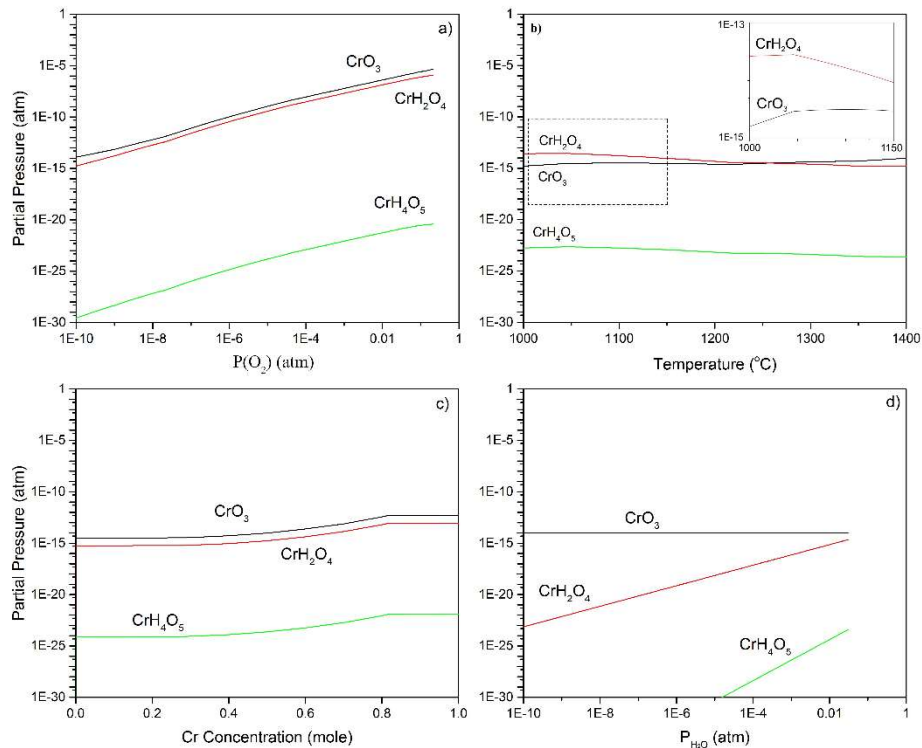


Figure 3-5. The Cr^{6+} species in gas a) with change in $P(\text{O}_2)$ at 1400 $^{\circ}\text{C}$ for the LSCrF-55, b) with change in temperature at $P(\text{O}_2)=10^{-10}$ atm for the LSCrF-55, and c) with change in Cr concentration at 1400 $^{\circ}\text{C}$ and $P(\text{O}_2)=10^{-10}$ atm, and d) with change in H_2O concentration for LSCrF-55 at 1400 $^{\circ}\text{C}$ and $P(\text{O}_2)=10^{-10}$ atm.

In the wet atmosphere, CrO_3 remains dominant species of Cr^{6+} and independent of changes in $P(\text{H}_2\text{O})$; however, the concentration of the CrH_2O_4 and CrH_4O_5 increases as $P(\text{H}_2\text{O})$ goes up (Figure 3-5.d).

5. Discussions

There are two critical issues in the application of OTM, i.e., the stability of the liquid phase and its control at sintering temperature and cooling conditions and the release of Cr^{6+} gas species under the sintering and operating conditions. Based on the previous experimental observations and the current prediction from computational Thermodynamic, we can have a more comprehensive understanding of the LSCrF sintering process and the Cr^{6+} gas species emission.

a. Thermodynamic Consideration of the Sintering

The sintering of doped- LaCrO_3 structures with high densification is a well-known challenge [7]. There have been experimental investigations regarding the Thermodynamic and kinetics during the LSCrF sintering process at high temperature [47, 53, 54]. It is reported that the microstructure of the sintered samples varies depending on the LSCrF composition, the sintering temperature, and $P(\text{O}_2)$ [53, 54]. A key point in these studies is the formation of the liquid phase at 1400°C and only under a reducing atmosphere [53, 54], which has also been predicted in the current study (Figure 3-2). The observation of liquid at high temperatures sheds some light on a new method to improve the densification of LSCrF during the sintering process. It is worthwhile to have a comprehensive understanding of the high-temperature phase stabilities and phase transformations during the cooling process, as shown below.

b. Liquid Phase Stability at High Temperature

It has been reported that the presence of 5 to 15 vol.% liquid would help to enhance the densification during the liquid phase sintering (LPS) process through increased anionic or cationic species transport, grains rearrangement, and filling of voids among particles, which can also reduce the time required for sintering [71, 72]. The same trend has been reported for LSCrF sintering. Indeed, there is experimental evidence on the formation of the liquid phase for the sintering of LSCrF under nitrogen and dilute hydrogen gas [54]. Meanwhile, it has been observed that the density has increased from 65.6% under air to 96.3% under dilute hydrogen ($\text{Ar}-3\%\text{H}_2-3\%\text{H}_2\text{O}$) after sintering at 1400°C for 10 hours soaking time. The experimentally observed liquid formation may be the reason for the densification improvement.

On the other hand, the formation of the excessive liquid phase during the sintering process may also have a negative impact on the concentration of the dopants in the perovskite structure, which affects the stability and the electrical properties of LSCrF. The effect of the formation of the excessive liquid phase is observed after sintering at 1400°C under dilute hydrogen gas [56]. It is postulated that the excessive liquid phase forming at high temperatures may drain dopant elements from the perovskite structure into the liquid phase. When the temperature decreases during the cooling process, it is predicted that most portion of the liquid phase solidifies as Fe-rich secondary phases and does not re-form perovskite structure. This trend may make a chemical composition gradient in LSCrF perovskite structures and also change microstructure. Hence, it is preferred to have only a small amount of liquid at the sintering temperature of LSCrF, as it may improve the densification and have the minimal side effects.

As demonstrated schematically in Figure 3-6, the thermodynamic stability of the liquid phase is determined by $P(O_2)$ and the temperature. It is based on the prediction of the liquid phase thermodynamic stabilities at 1400°C for all these three LSCrF compositions in Figure 3-2. It shows that there are two stages for the liquid phase with all the three LSCrF compositions selected. By using the LSCrF-55 as an example, a limited amount of the liquid phase is formed between the LSCrF grains and the concentration of the liquid phase is not sensitive to the change of $P(O_2)$ in the first stage, where $P(O_2)$ is higher than 10^{-7} atm. It is called Stage I in the current work. With the $P(O_2)$ lower than 10^{-7} atm, much more liquid is formed between the LSCrF grains, and the trend of the liquid phase formation is changed. The concentration of the liquid phase becomes very sensitive to the change of $P(O_2)$, which is called Stage II in the current work. The liquid phase grows sharply to ~ 1.35 mole at $P(O_2) = 10^{-10}$ atm. It has been determined that the boundary of these two stages is around 0.2 to 0.4 mole of the liquid phase.

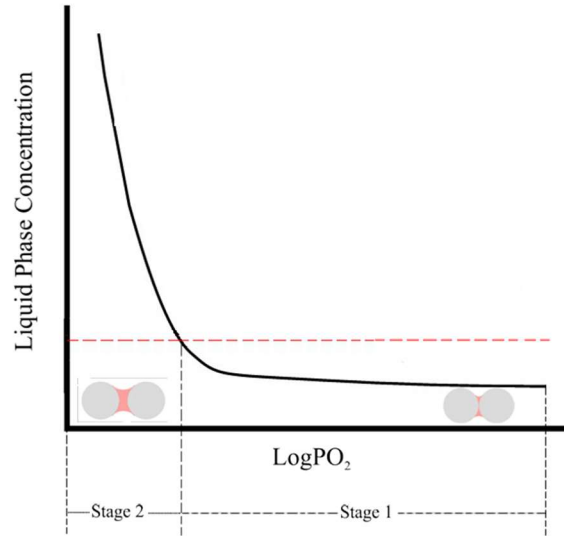


Figure 3-6. Sketch of the liquid phase stability with the change of $P(O_2)$ at 1400°C.

By comparing these two stages as demonstrated in Figure 3-6, staying in Stage I may be much more preferred than in Stage II during the sintering of LSCrF. Firstly, the formation of a high concentration of the liquid phase from LSCrF may increase volume expansion and reduce the flexure strength of the material at high temperatures. Secondly, since the liquid phase is predicted to be Sr and Fe rich comparing with their initial perovskite composition as shown in Table 3-2, the excessive amount of the liquid phase formed in Stage II may make the remaining perovskite structure lacking dopant elements (Sr, Fe). Since these elements may adjust the physico-thermal properties of the perovskite, it is expected that the remaining perovskite structure presents different thermal and electrical properties. However, the formation of limited concentration of the liquid phase in Stage I may have a minor impact on the chemical stability and stoichiometry of the perovskite. Thirdly, it may be easier to control the liquid phase concentration in Stage I, while a small change of $P(O_2)$ in Stage II may cause a dramatic concentration to change for the liquid phase.

i. The Liquid Phase Concentration Threshold Diagram

The behavior of the liquid phase, especially the change in the concentration of the liquid phase with temperature and $P(O_2)$ during the sintering process, may help provide guidance on the choice of the sintering parameters, including the soaking temperature and $P(O_2)$ for LSCrF. With the help of computational Thermodynamic, we have developed a liquid phase concentration threshold diagram with a fix concentration of the liquid phase, which shows the change of $P(O_2)$

and the temperature for each LSCrF composition. It is assumed that a maximum of 0.2 moles of liquid will be beneficial to the densification for 1 mole per formula LSCrF, which is around 4mol.% liquid. Such liquid concentration threshold (0.2 moles of liquid) has been chosen as shown in Figure 3-7 for all three LSCrF compositions to ensure that the system is still in Stage I. Furthermore, each threshold line for a LSCrF composition divides the diagram into two regions. Above the threshold lines, there are more than 0.2 moles of the liquid phase forms. Below the lines, the liquid phase is either unstable or less than 0.2 moles.

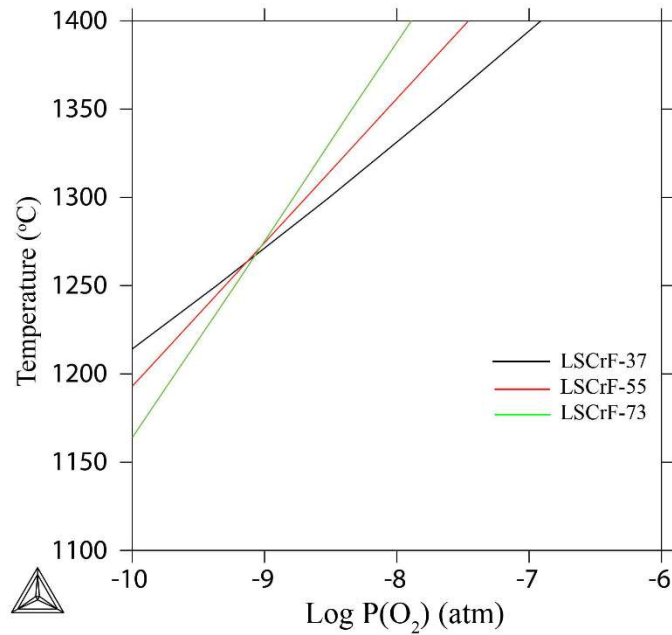


Figure 3-7. Threshold diagram for 0.2 moles of the liquid phase with the change in temperature and $P(O_2)$.

For a specific composition of LSCrF, the threshold $P(O_2)$ reduces with the decrease of temperature in the threshold diagram. For example, it is predicted that 0.2 moles of the liquid phase form at 1400°C for $P(O_2) \sim 10^{-7.5}$ atm for LSCrF-55 as shown in Figure 3-7. To have the same concentration of the liquid phase forms at $P(O_2) \sim 10^{-10}$ atm, the temperature should drop to $\sim 1190^\circ\text{C}$. A similar trend is observed for the other two LSCrF concentrations. It can be concluded that a more reducing condition is needed to reduce the sintering temperature.

Besides, the diagrams with different thresholds can be easily produced with the same approach accordingly. If the concentration of the liquid phase is more than needed, it is suggested to reduce the sintering temperature following the trend predicted in Figure 3-7. If less liquid than needed, it is suggested changing the A site deficiency of LSCrF to tune the concentration of the

liquid phase instead of changing the $P(O_2)$ to move to Stage II. Figure 3-7 depicts the simulation of the changes in the liquid phase concentration with a change in A-site deficiency of LSCrF-55. It can be observed the liquid phase concentration increases with the increase of A-site deficiency under both 1400°C and 1200°C. For example, the liquid phase can reach ~12 mol.% at 1200°C with $P(O_2) = 10^{-10}$ atm for the 10% A-site deficiency LSCrF-55. Of course, the typical A site deficiency is chosen between 2% to 5%. It clearly shows the feasibility of changing the liquid phase formation with the change of the A-site deficiency. Meanwhile, the concentration of the liquid in Stage II is very sensitive to $P(O_2)$ and should be avoided, a tiny change of $P(O_2)$ may change the liquid formation at the sintering condition.

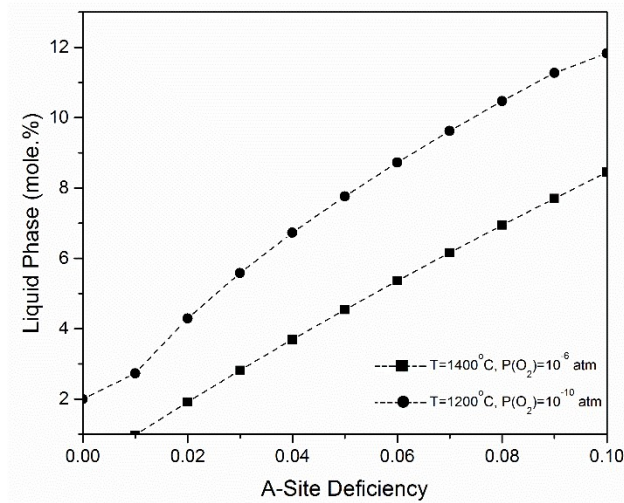


Figure 3-8. The liquid phase volume percentage with the A-site deficiency for $(La_{0.8}Sr_{0.2})_{1-y}Cr_xFe_{1-x}O_{3\pm\delta}$ ($x=0.5$, and $0 \leq y \leq 0.9$) at 1400°C and $P(O_2)=10^{-6}$ atm and 1200°C and $P(O_2)=10^{-10}$ atm.

It is worth noting that the prediction from computational Thermodynamic only provides a trend for the thermodynamic predictions instead of the accurate numbers on temperature, $P(O_2)$, and liquid concentration, not to mention the effect of kinetics is not considered. It is not guaranteed that the exact amount of the liquid phase, as predicted, will be observed in real sintering experiments. Further experimental verification is still needed. However, the expected trend of the liquid phase thermodynamic stability should guide further investigation.

ii. Microstructure Evolution During Cooling Process

The microstructure evolution during the LPS sintering process may be very different from the solid-state sintering.

Figure 3-9 schematically shows the formation of the liquid phase during the heating process and the solidification process under the two extreme cooling conditions, which applies to all three LSCrF compositions as shown in Figure 3-3 and Figure 3-4.

Figure 3-9.a and b show the liquid phase formation is promoted between two grains of the initial perovskite as temperature increases.

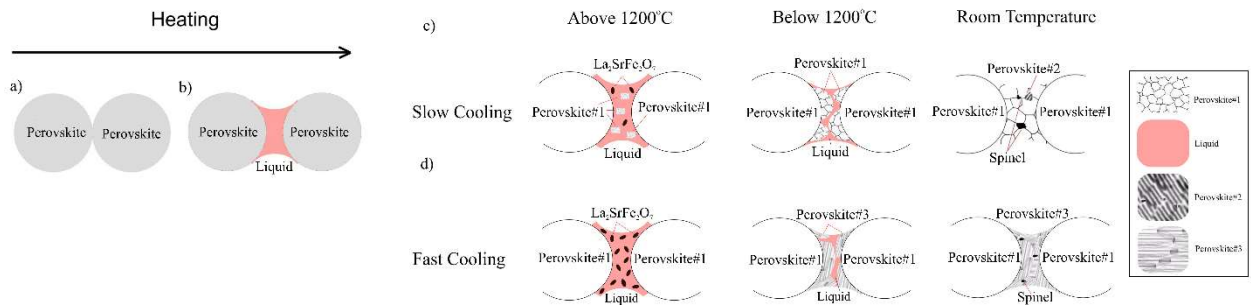


Figure 3-9. The schematic of the liquid phase (a, b) formation and (c, d) solidification.

The microstructure evolution during the cooling process may be very different from the different cooling rates, as shown in

Figure 3-9.c, and d. With the prolonged cooling rate, the perovskite with a composition similar to the initial perovskite composition (Perovskite #1) may precipitate out along with a small amount of the temporary $\text{La}_2\text{SrFe}_2\text{O}_7$ phase. With the further drop of the temperature, the temporary $\text{La}_2\text{SrFe}_2\text{O}_7$ phase may disappear, and much more perovskite may precipitate out. At the end of the solidification process, a small amount of the spinel phase may form. On the contrary, the cooling process of the fast cooling rate may be very different. With the drop-in temperature, much more the temporary $\text{La}_2\text{SrFe}_2\text{O}_7$ phase may precipitate out. With the further decrease of temperature, the temporary $\text{La}_2\text{SrFe}_2\text{O}_7$ phase may disappear while Perovskite #3 may form, which is significantly different from the original perovskite composition (Perovskite #1) as shown in Table 3-3. At the end of the solidification process, a small amount of the spinel phase may form.

The above analysis is based on the two extreme cooling conditions, it is expected that the phases at room temperature after the typical cooling process should be between these two predicted microstates, i.e., small amount of spinel/corundum may be observed in the grain boundary; slight perovskite composition difference may be observed across the grain boundary. Such perovskite

composition difference will cause the change of the chemical and electrical properties, which is another reason to choose to stay in Stage I during the sintering process.

c. Emission of Cr⁶⁺ Containing Gas Species

Besides the phase stability during the sintering process, formation and transport of gaseous Cr⁶⁺ remains a concern for LSCrF. Cr⁶⁺ is listed as number 17 in the Agency for Toxic Substance and Disease Registry, Priority List of Hazardous substances (ATSDR, 2015) [73]. The total Cr contamination for soil screening levels is 390 mg/kg for ingestion, 270 mg/kg for inhalation, and 2.0 mg/kg for migration to groundwater (USEPA) [74].

CrO₃ is typically the dominant Cr⁶⁺ gas species; however, the partial pressure of CrH₂O₄ in wet atmosphere dominates at lower temperatures and remains very close to CrO₃ at elevated temperatures indicating the release of Cr⁶⁺ to the environment. Based on the prediction from Figure 3-5.a, the concentrations of all the Cr⁶⁺ gas species increase with the increase of P(O₂). The concentration of Cr⁶⁺ species in gas for LSCrF-55 is 32 mg/kg at 1400°C with P(O₂) = 10⁻¹ atm, which is much lower than the USEPA limit for inhalation. The concentration of Cr⁶⁺ species at 1400°C with P(O₂) = 10⁻¹⁰ atm significantly drops to 3.09×10⁻⁸ mg/kg. Meanwhile, the partial pressure of CrH₂O₄ will be much higher than CrO₃ at low temperatures. CrH₂O₄ in the wet atmosphere becomes dominant with the decrease of temperature (Figure 3-5.b). Specifically, P(CrH₂O₄) is ~16 times higher than P(CrO₃) at 1000°C where the total concentrations of Cr⁶⁺ gas species are 7.63×10⁻⁸ mg/kg. Furthermore, the effect of H₂O partial pressure (P(H₂O)) on the formation of various Cr⁶⁺ gas species is predicted in Figure 3-7.d. The concentration of the CrH₂O₄ and CrH₄O₅ species rises with an increase in the H₂O concentration in the gas, while CrO₃ concentration remains essentially constant with the change of water vapor concentration.

Overall, the total emission of Cr⁶⁺ is well below the inhalation limit, especially under the OTM operation and sintering conditions. It conveys that the emission of Cr⁶⁺ for LSCrF is not a concern during the operation and sintering process.

6. Conclusions

Thermodynamic investigation of (La_{0.8}Sr_{0.2})_{0.98}Cr_xFe_{1-x}O_{3±δ} (x=0.3, 0.5, 0.7) under oxidizing and reducing atmosphere (10⁻¹⁰ ≤ P(O₂) ≤ 0.21 atm) and 1000-1400°C has been comprehensively carried out utilizing the CALPHAD approach and pertinent thermodynamic database. Our findings include:

1. The phase equilibria at 1400°C shows the formation of corundum, spinel, $\text{La}_2\text{SrFeO}_7$, and the liquid phase. The liquid phase formation is preferred in reducing atmospheres at high temperatures. Besides, more liquid is observed with the increase of the Fe content in LSCrF.
2. The liquid phase concentration threshold diagram provides guidance on the choice of the sintering parameters, including the sintering temperature and $P(\text{O}_2)$ for different LSCrF compositions. Also, it shows that tuning the A site deficiency is effective to achieve the desired liquid phase concentration at high temperature.
3. It is suggested to form a limited amount of the liquid phase during the sintering process to improve the densification and minimize the side effect on the change of chemical and electrochemical properties.
4. The equilibrium (slow) cooling and the fast cooling simulations indicate the dependence of the microstructure on the cooling rate. Besides the possible formation of corundum and spinel in the grain boundary, it primarily shows that the fast cooling rate may cause the formation of new perovskite with different compositions in the grain boundary. Besides, the predicted microstructural evolution under the effective cooling rate shows good agreement with experimental observations.
5. The capability of the La-Sr-Cr-Fe-O system to form Cr^{6+} containing gas species in the sintering or device exposure environment has been scrutinized for the first time under the dry and wet atmosphere. The concentrations of all the Cr^{6+} containing gas species formed under sintering and operation conditions are much lower than the inhalation limit from ATSDR.

Chapter 4 : The Origin of Phase Separation in $(\text{La}_{0.8}\text{Sr}_{0.2})_{0.95}(\text{Cr}_x\text{Fe}_{1-x})\text{O}_{3\pm\delta}$ Perovskites

Plan to publish in: Physical Chemistry Chemical Physics

Abstract

The current research investigates the phase separation phenomenon in $(\text{La}_{0.8}\text{Sr}_{0.2})_{0.95}(\text{Cr}_x\text{Fe}_{1-x})\text{O}_{3\pm\delta}$ (LSCrF) under the fabrication and processing conditions of Oxygen Transport Membranes (OTM). The research employs two experimental and computational Thermodynamic approaches with the focus on changes in crystal structures and phase stability on Cr-rich perovskites. The chemical stability has been examined under high temperatures (700-1400°C) with different oxygen partial pressures ($p(\text{O}_2)$) (0.21 to 10^{-19} atm). The phase stability of the samples has been studied by X-ray diffraction, scanning electron microscopy, and Rietveld refinement methods. The results reveal complicated correlations among dopant disintegrations in phase separation of the perovskite phase. The research provides predictions and practical procedures in the purpose of extending the lifetime of OTMs under processing conditions. The results for the perovskite phase have also been extended to design dual-phase composite of Yttria-stabilized ZrO_2 (YSZ) and LSCrF for high-temperature ceramic membranes.

1. Introduction

Lanthanum chromite-based perovskites are prime candidates for high-temperature electrochemical devices such as gas sensors, Oxygen Transport Membranes (OTM), and electrodes in Solid Oxide Fuel Cells (SOFC) [3, 8, 12, 75-77]. In these applications, they can provide both high electronic and ionic conductivity at elevated temperatures while they face sharp oxygen partial pressure ($p(\text{O}_2)$) gradients [4, 78]. However, failure in chemical stability is one of the significant obstacles for the realization of these applications [3, 8, 79, 80]. The chemical stability over both fabrication and processing conditions is so critical so that it can lead to 1) failure in mass transport properties 2) mismatch in coefficient of thermal expansion (CTE) for adjacent phases, and 3) detrimental solid-state phase transitions during thermal cycles [3]. A combination of these effects can result in the failure of the materials in the electrochemical devices.

Co-doping on both A- and B-sites is a technique to tune the ultimate properties of perovskites [15, 18, 44, 81-85]. In LaCrO_3 , the method is widely used to enhance its oxygen permeation, thermal expansion, sinterability, and electrical properties [3, 12, 82, 86, 87]. Using Sr^{2+} as A-site dopants promote the formation of oxygen vacancies and oxygen ion conduction while using B-site cations with multiple valance states like Fe^{3+} enhance electronic conduction [45, 88]. Accordingly, doped structures of $\text{LaCrO}_{3\pm\delta}$ as $(\text{La,Sr})(\text{Cr,Fe})\text{O}_{3\pm\delta}$ (LSCrF) with high electrical conductivity deliver reliable oxygen permeation rates over wide ranges of temperature (T) and $p(\text{O}_2)$ [46, 89]. Outstanding features of LSCrF has recently attracted lots of attention. However, complex chemical stability of the La-Sr-Cr-Fe-O system leads to contradictory results in the literature, especially for highly doped structures under low $p(\text{O}_2)$ [16, 52, 85, 90, 91]

One of the effects of adding dopants is to control the crystal structure of LSCrF. The crystal structure of $\text{LaCrO}_{3\pm\delta}$ can transform from orthorhombic (Pnma) via rhombohedral ($R\bar{3}c$) to cubic ($\text{Pm}\bar{3}m$) with dopants and temperature [92, 93]. The orthorhombic \leftrightarrow rhombohedral phase transition occurs $\sim 271^\circ\text{C}$ for $\text{LaCrO}_{3\pm\delta}$ [94]. Its volume will be shrunk to -0.138% due to the phase transition, which it comes with an anomaly in CTE [94, 95]. As Sr increases on A-site, the rhombohedral structure will be stabilized at ambient temperature [92]. However, the increase in Fe on B-site stabilizes the orthorhombic structure at room temperature [96]. Regardless of crystal symmetries, the chemical stability of the LSCrF becomes complicated due to the appearance of secondary phases [16, 45, 54, 56].

One of the phenomena in LSCrF is the co-existence of two rhombohedral and orthorhombic structures. There are limited reports on this occurrence in separate studies by Oishi, Gupta, and Lü [43, 56, 85]. Lü has studied the phase stability of LSCrF samples at 1000°C under the $\text{H}_2\text{-H}_2\text{O-N}_2$ atmosphere for 44 hours. In the study, the XRD patterns present single-phase perovskite structures after the stability test. However, due to the chemically induced strains in redox cycling, they have postulated the existence of the orthorhombic \leftrightarrow rhombohedral phase transition in the samples after considering XRD and Mössbauer spectra. In a separate study, Oishi et al. investigated the hysteresis behavior of the oxygen nonstoichiometry (δ) in $(\text{La}_{0.75}\text{Sr}_{0.25})(\text{Cr}_{0.5}\text{Fe}_{0.5})\text{O}_{3\pm\delta}$ under reducing atmospheres between 700 to 1000°C . They assumed that the hysteresis behavior in δ with $p(\text{O}_2)$ for $(\text{La}_{0.75}\text{Sr}_{0.25})(\text{Cr}_{0.5}\text{Fe}_{0.5})\text{O}_{3\pm\delta}$ can be justified by the occurrence of phase separation due to the reduction of Fe ions under the reducing atmospheres. Gupta and Sabarou also mentioned the

formation of a second perovskite by Thermodynamic simulations in a separate investigation. However, there is no comprehensive study to examine the phase separation in LSCrF and investigate its involved parameters and mechanisms. The phase separation is also necessary since it can lead to stoichiometry deviations and result in the formation of two rhombohedral and orthorhombic structures. As mentioned before, the related phase transition comes with the volume change, which can build up stress in bulk materials and make abnormal changes in CTE [92, 93, 95]. Also, both ionic and electronic conductivities in LSCrF benefit from high crystal symmetry (cubic) [8]. Degradation in crystal symmetry (from rhombohedral to orthorhombic) due to the phase separation can reduce electrical conductivity.

In the current research, two experimental and computational Thermodynamic approaches have been utilized to study the perovskite phase separation in LSCrF. Different compositions of LSCrF have been examined under both fabrication and processing conditions. Besides, the results have been extended to a new area of dual-phase composite ceramic oxide membranes, where the composites are made of two fluorite and perovskite phases. The focus of the research is on the structural integrity of LSCrF and involved mechanisms. It also presents the potential of computational Thermodynamic in predicting and designing new materials based on LSCrF.

2. Experimental

Different compositions of lanthanum chromite-based perovskites have been provided by Praxair Inc. In these powders, Sr and Fe are A- and B-site dopants, respectively. The compositions include $(\text{La}_{0.8}\text{Sr}_{0.2})_{0.95}\text{Cr}_x\text{Fe}_{1-x}\text{O}_3$ ($x=0.9, 0.8, \text{ and } 0.5$). It is referred as LSCrF through the paper. The last two digits address the Cr: Fe ratio on the B-site. For examples, LSCrF91 is to refer to $(\text{La}_{0.8}\text{Sr}_{0.2})_{0.95}\text{Cr}_{0.9}\text{Fe}_{0.1}\text{O}_{3\pm\delta}$. To investigate the thermal behavior of different compositions, separate pellets have been prepared for each composition. The diameter and thickness of the initial pellets are less than 13 and 1 mm, respectively. The pellets have been pre-sintered at 1150°C for 2 hours under air. They have been heated at 850°C for 10 hours under wet forming gas (4% H_2 -96%Argon) in a tube furnace (MTI Corporation), and then quenched in the air on a cold alumina surface. Owing to their thin thickness and small diameters, the pellets can get cold fast. It is referred as the stability test throughout the paper. Temperatures and atmospheres ($p(\text{O}_2)$) have been chosen as they can represent the fabrication and processing conditions of OTMs and SOFCs [3, 8, 40, 77].

The oxygen partial pressure inside the furnace has been constantly monitored by Rapidox 2100 Gas Analyzer. To control $p(\text{O}_2)$ inside the furnace, wet-forming gas has been introduced to the furnace by using a humidity bottle. The temperature of the humidity bottle has been controlled so that the $p(\text{O}_2)$ inside the furnace remains constant during the tests. Further information about this technique can be found in the literature [37].

Crystal structures of the samples have been examined by X-ray Diffraction with Cu tube (PANalytical EMPYREAN) in the range of 20-120°. Also, the structural changes have been scrutinized by the Rietveld refinement method and HighScore Plus software (version 4.8). All samples including initial powders, pre-sintered, and heat-treated have been examined by the Rietveld refinement method. The refinement analysis has been applied for background, zero shift, specimen displacement, lattice parameters, wave functions, and asymmetrical parameters. Site fractions and atomic coordination have not been refined in this study. The microstructure of the sample has been studied by Scanning Electron Microscopy (SEM) (JEOL JSM-7000F) coupled with Energy-dispersive X-ray Spectroscopy (EDS) (Oxford Instrument X-MAX^N).

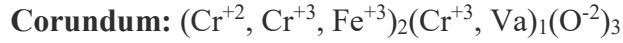
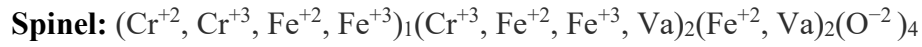
Dual-Phase composite samples of LSCF and 8%(Y₂O₃)-ZrO₂ (yttria-stabilized Zirconia, 8YSZ) have been prepared by mechanical mixing of two powders with equal weight ratios. The Saint-Gobain ZirPro ceramic grinding media (Zirmil®Y) has been used during milling. The milling for each composition has been proceeded for at least 6 hours. Similar sizes of pellets have been prepared after removing the grinding media. The pre-sinter and stability test procedures for the dual-phase composites are identical to the single-phase perovskite samples.

3. Computational Thermodynamic

The simulations have been conducted based on the CALPHAD (CALculation of PHase Diagrams) approach for multi-component materials. To perform simulations, a database for the La-Sr-Cr-Fe-O system has been employed with the consideration of available databases on simple systems [19, 21, 24, 97]. Further details on the simulation parts and its implementation can be found in this reference [16]. However, it is necessary to review the sublattice models for the most important phases and solid solutions in the current study. For the perovskite phase, the structure has been modeled with three sublattice models:



Where Va stands for the vacancy. The current simulation is based on 5 moles of perovskite with considering 1 mole for A-site, 1 mole for B-site, and 3 moles for the oxygen site. Owing to have 0.05 deficiency on A-site ((La_{0.8}Sr_{0.2})_{0.95}Cr_{0.9}Fe_{0.1}O₃), the total mole is 4.95 moles in simulations results. The presence of Ar in the forming gas has also been considered and balanced, but it has not been shown in simulations due to its unvarying status in the gas phase. Among secondary phases, two solid solutions of spinel and corundum have been considered with four and three sublattices, respectively:



The spinel phase has been simulated with one model, but it can be rich from either Cr or Fe. The formations of Sr-oxide and SrCr_mO_n phases have been considered as stoichiometric compounds.

4. Results

Simulation conditions have been chosen based on two concerns. Firstly, they should reflect the fabrication and processing conditions for OTM and SOFC applications. These include a temperature range from 700 to 1400°C, and a p(O₂) range from 10⁻²² atm up to ambient atmosphere (0.21 atm). However, due to the high discrepancy among simulations and previously reported experimental results, the simulation has been limited to the range of 0.21 to 10⁻¹⁹ atm and 700-1300°C. Secondly, after defining the framework conditions, we have focused on conditions that help to investigate the system and unravel involved mechanisms. The results have been examined so that they can explain the behavior of the system for the whole range of temperature and p(O₂). Later, the simulated results have been utilized to design experimental conditions regarding instrumental limits, challenges to control p(O₂), and kinetic effects. The focus is on reducing atmospheres where the chemical stability of the material has been compromised by formations of several secondary phases.

4.1 Thermodynamic Simulations

Several secondary phases can form during the fabrication and processing of LSCrF. Figure 4-1 shows simulation results for formations of secondary phases for LSCrF91 over changes in temperature (Figure 4-1.a) and $p(\text{O}_2)$ (Figure 4-2.a). In general, secondary phases can be categorized into Fe-Cr phases (corundum and spinel), Sr-Cr phases (SrCr_mO_n), and liquid phases. Their stabilities depend on temperature and $p(\text{O}_2)$. The existence and thermal behavior of these phases have been already investigated [16, 50, 54, 56]. Notably, the formation of SrO and spinel will be addressed later in the discussion part due to their critical influences.

The most interesting feature of these results is the separation of the initial perovskite into two perovskite structures: perovskite #1 and perovskite #2. It seems that the initial perovskite structure (LSCrF91) has been separated into two different perovskite structures, in which the perovskite #2 cannot survive temperatures higher than 1000°C .

To examine compositions of the perovskite structures, the distribution of elements among phases has been simulated with changes in temperature and $p(\text{O}_2)$. The elemental distributions can show how elements partition among phases over changes in temperature and $p(\text{O}_2)$. Figure 4-1.b and Figure 4-2.b show the distribution of Fe as the B-site dopant with changes in temperature and $p(\text{O}_2)$ under Thermodynamic equilibrium conditions.

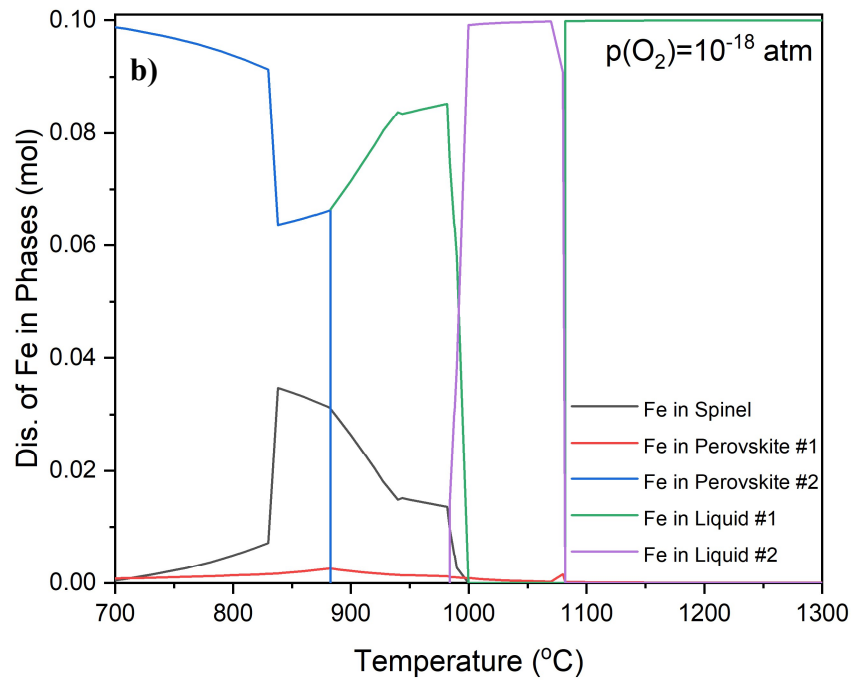
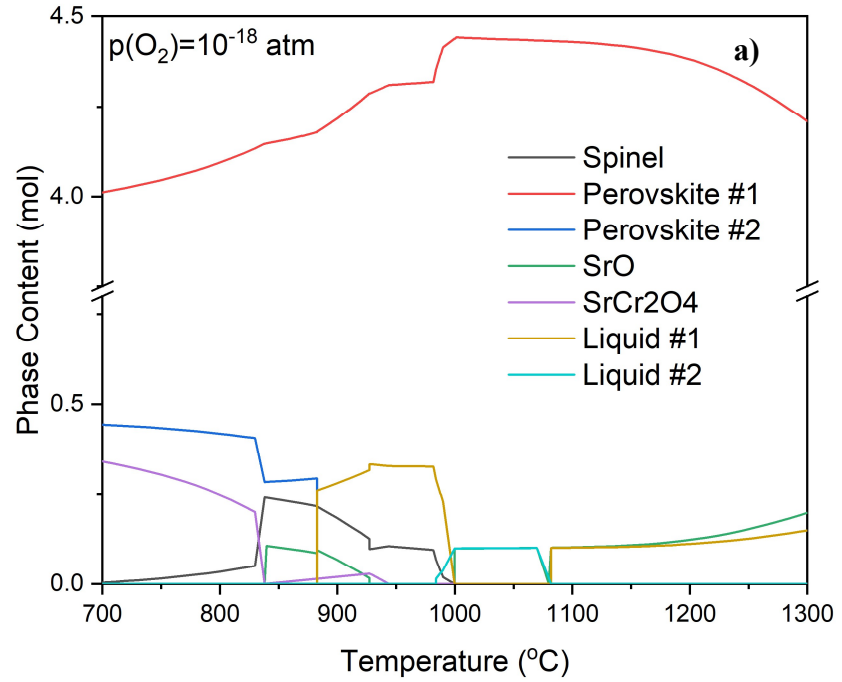


Figure 4-1 Changes in a) phases stability and b) distribution of Fe in phases in $(\text{La}_{0.8}\text{Sr}_{0.2})_{0.95}\text{Cr}_{0.9}\text{Fe}_{0.1}\text{O}_3$ between 700 to 1300°C at $p(\text{O}_2)=10^{-18}\text{atm}$

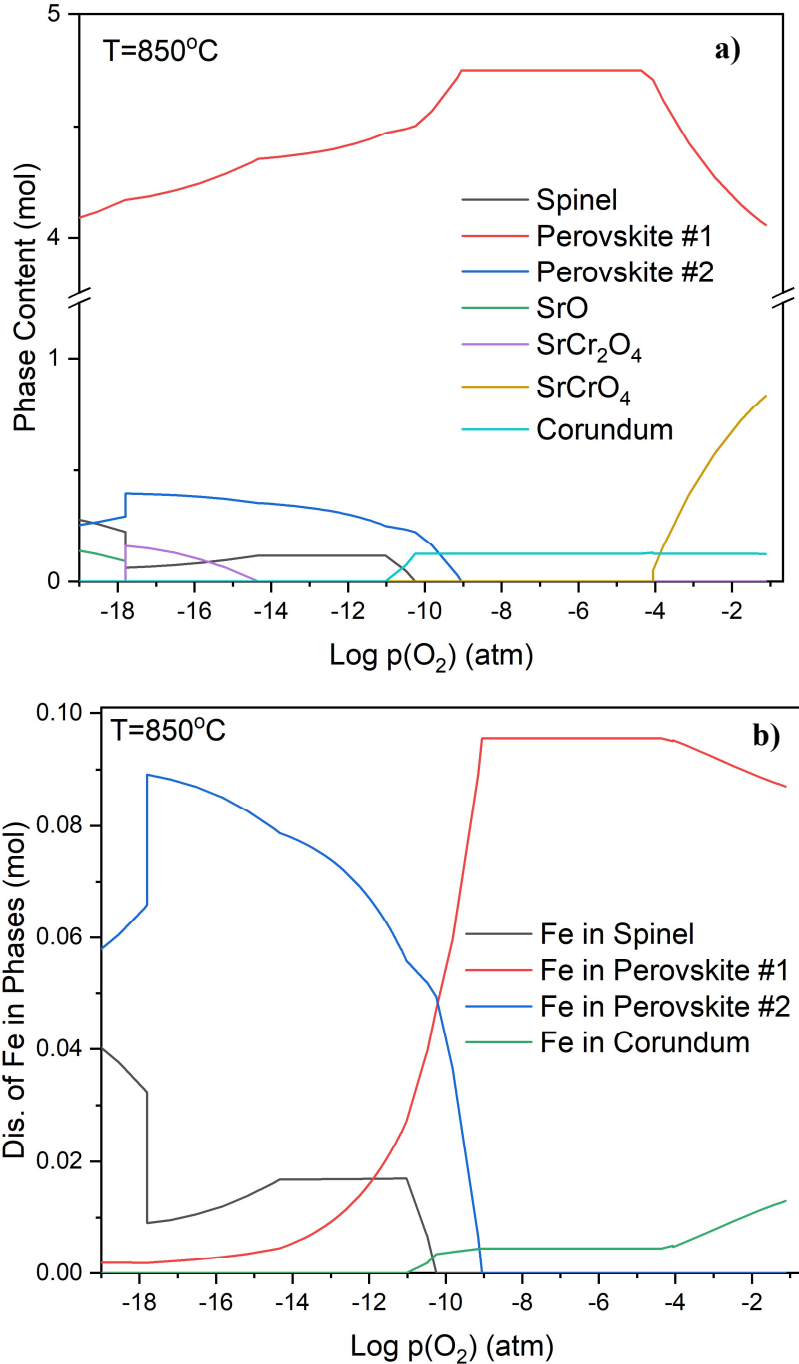


Figure 4-2. Changes in a) phase stability and b) distribution of Fe in phases in $(\text{La}_{0.8}\text{Sr}_{0.2})_{0.95}\text{Cr}_{0.9}\text{Fe}_{0.1}\text{O}_{3+\delta}$ with changes in $p(\text{O}_2)$ (10^{-19} to 0.21 atm) at 850°C.

Based on Figure 4-1.b, Fe has been partitioned among a spinel and two perovskite structures (perovskite#1 and perovskite #2) at low temperatures. With further increase in temperature, liquid phases form and contain more portions of Fe content (Liquid #1 and #2). This trend shows that perovskite #2 with a lower phase amount (<0.5 mol- Figure 4-1) has almost the entire content of Fe.

It is stable at lower temperatures up to 1000°C and becomes richer from Fe when $p(\text{O}_2)$ drops (Figure 4-1.b).

The point calculations at several fixed temperatures and $p(\text{O}_2)$ conditions indicate that the perovskite#1 is mainly rich from Cr, while the perovskite#2 is rich from Sr and Fe. Perovskite #1 has a closer composition toward the initial LSCrF91, while perovskite #2 represents a new perovskite composition. It seems that perovskite #2 has been formed due the exposure to harsh conditions and through a stoichiometric deviation. This deviation can be examined by plotting site fractions over the temperature range. Figure 4-3 shows the summation of site fractions of all Fe ion species (Fe^{+2} , Fe^{+3} , and Fe^{+4}) in the B-site of the two perovskite structures. Based on this figure and the defined sublattice model for the perovskite phase, the B-site of the perovskite #2 is rich from Fe till its decomposition below 1000°C. It can also be inferred that the perovskite #1 remains rich from Cr on B-site.

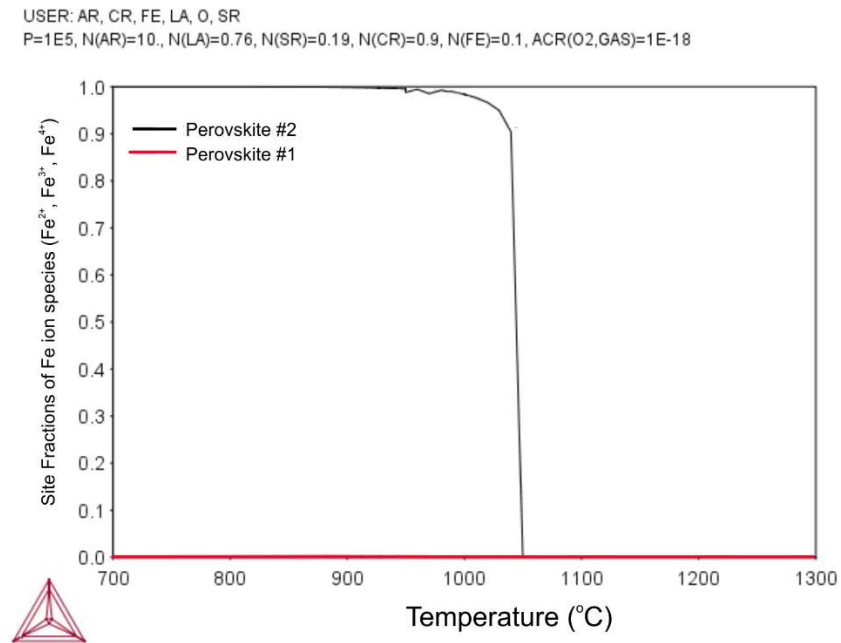


Figure 4-3. The partitioning of Fe ion species (Fe^{2+} , Fe^{3+} , and Fe^{4+}) in Perovskite #1 and Perovskite #2 with changes in temperature at $p(\text{O}_2)=10^{-18}$ atm for $(\text{La}_{0.8}\text{Sr}_{0.2})_{0.95}\text{Cr}_{0.9}\text{Fe}_{0.1}\text{O}_{3\pm\delta}$.

Based on the results, it is assumed that the initial content of Fe in the perovskite plays a critical role in the perovskite phase separation. To find out the correlation between Fe and the phase separation, the simulation has been repeated as the Fe content in the perovskite can change

between 0 to 0.5 (Figure 4-4). The results have been narrowed down to the temperature/ $p(\text{O}_2)$ window where the phase separation has been observed. At $T=850^\circ\text{C}$ and $p(\text{O}_2)=10^{-18}$ atm, it shows that increase in the Fe content up to ~ 0.40 mol promotes the formation of the perovskite#2 up to ~ 1 mol, but there is a threshold for Fe as further increase in Fe leads to lower content for the perovskite#2 (Figure 4-4. – redline). The occurrence of this threshold is concurrent with the formation of the liquid phase at the same conditions (Figure 4-4 -redline). The formation of the liquid phase with a decrease in the Cr: Fe ratio has been already reported for LSCrF perovskites [16, 50, 54, 56]. If temperature reduces or $p(\text{O}_2)$ becomes more oxidizing, the threshold behavior gets disappeared in Figure 4-4 due to the disappearance of the liquid phase in these conditions. Accordingly, the perovskite #2 can continuously increase with the decrease of the Cr: Fe ratio.

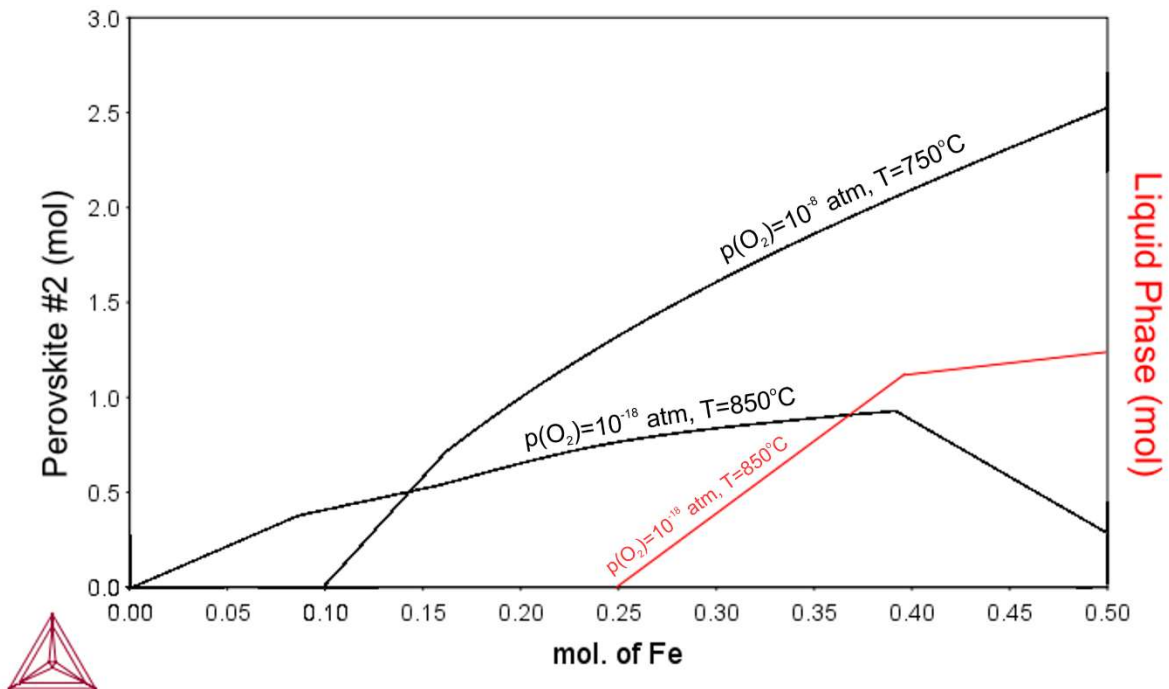


Figure 4-4. The formation of the perovskite#2 and liquid phase with changes in the Fe content in $(\text{La}_{0.8}\text{Sr}_{0.2})_{0.95}\text{Cr}_{0.9}\text{Fe}_{0.1}\text{O}_{3\pm\delta}$ at two different temperatures and oxygen partial pressures.

4.2 Crystal Structure and Ceramic Microstructure

The crystal structure of the LSCrF91 sample has been examined after the stability test. The refined results show that the perovskite structure has the rhombohedral structure with $R\bar{3}c$ crystal symmetry. No sign of the phase separation has been detected for this sample. However, high-

resolution X-ray diffraction reveals small peaks for the SrO phase at ~ 29.5 and 58.5° (Figure 4-5, and Table 4-1). Adding SrO as the second phase to the LSCrF91 improves its reliability factor (R_{wp}) from 12.2511 to 6.9217%. According to refined results, the content of SrO is less than 1 Wt.%.

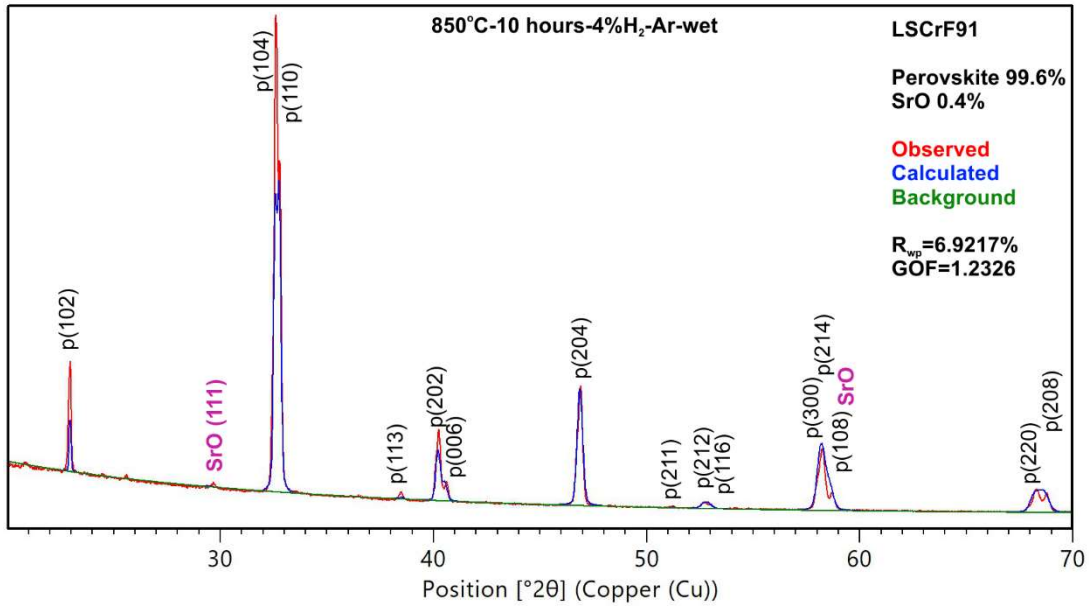


Figure 4-5. The XRD patterns of $(La_{0.8}, Sr_{0.2})_{0.95}Cr_{0.9}Fe_{0.1}O_{3\pm\delta}$ perovskite after heating at 850°C for 10 hours under wet forming gas (4% H_2 -96%Ar).

Table 4-1 The refined parameters for $(La_{0.8}Sr_{0.2})_{0.95}Cr_xFe_{1-x}O_{3\pm\delta}$ perovskites after the heat-treatment at 850°C for 10 hours under wet forming gas (4% H_2 -96%Ar).

Refined parameters for LSCrF91 phase

Atoms	Site	X	Y	Z	U (\AA^2)	SOF
La	6a	0.0	0.0	0.25	0.5	0.76
Sr	6a	0.0	0.0	0.25	0.5	0.19
Cr	6b	0.0	0.0	0.0	0.5	0.9
Fe	6b	0.0	0.0	0.0	0.5	0.1
O	18e	0.529	0.0	0.25	0.5	1.0

Crystal Structure: Rhombohedral, Space group: $R\bar{3}c$; Unit cell parameters: $a=b=5.496 \text{ \AA}$, $c=13.34483 \text{ \AA}$, $\alpha=\beta=90^\circ$, $\gamma=120^\circ$; Unit cell volume: 349.0899 \AA^3 ; Chemical formula: $(La_{0.8}Sr_{0.2})_{0.95}(Cr_{0.9}Fe_{0.1})O_{3\pm\delta}$; ICDD 04-013-5267.

Refined parameters for SrO Phase

Atoms	Site	X	Y	Z	U (Å ²)	SOF
Sr	4a	0.0	0.0	0.0	0.5	1.0
O	4b	0.5	0.5	0.5	0.5	1.0
Reliability Factors	R _{wp} =6.9208%	R _p =5.1654%	R _{exp} =5.2791%	GOF=1.3110		

Crystal Structure: Cubic, Space group: Fm-3m; Unit cell parameters: a=b=c=5.16866 Å, $\alpha=\beta=\gamma=90^\circ$; Unit cell volume: 138.0807 Å³; SOF: site of fraction; x, y, z: Fractional coordinates; U: Isotropic atomic displacement parameter; Chemical formula: SrO; ICDD 00-006-0520.

Figure 4-6 presents SEM images for the same heat-treated LSCrF91. The investigations into the morphology of grains show that the LSCrF91 is composed of grains with different morphologies (Figure 4-6.a). Further, EDS analysis of these morphologies reveals that they are grains that are rich from Cr and Fe (Figure 4-6 .b). They can represent the formation of the spinel phase. The same grains can also be detected for the LSCrF82.

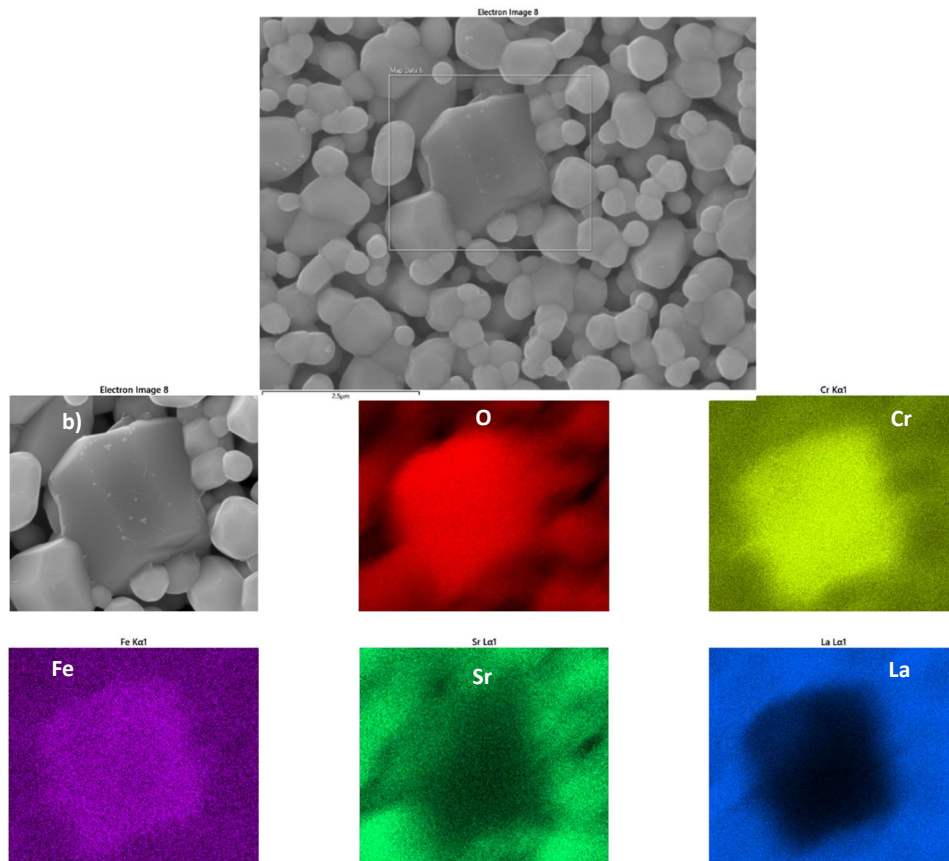


Figure 4-6. The microstructural analysis on the LSCrF91 after heating at 850°C for 10 hours under wet forming gas (4% H₂-96%Ar): (a) the formation of the spinel phase (b) EDS map analysis.

Also, a quantitative line scan analysis on different morphologies from one grain to adjacent grain has also been provided in Figure 4-7. Figure 4-7.a shows the formation of new morphologies in nanoscale for the heat-treated LSCrF82, which is rare across the sample. Figure 4-7.b presents elemental fluctuations across the line as the rate of the variations for each element has been indicated next to elements. The rates of the variations are severe so that they can reach 18 and 13.6 Wt% for La and Cr, respectively. Compared to the initial content of Sr (0.19 mol in 4.95 mol perovskite) and Fe (0.2 mol) in the LSCrF82, these fluctuations are also intense for Sr and Fe. The anomaly in morphology, together with elemental variations, has also been detected for the heat-treat LSCrF91 sample, as shown in Figure 4-7. c and d. There is a general trend for La and Cr as their contents counteract along with the line scan in both LSCrF91 and 82 (Figure 4-7 .b and d). However, it seems that the elemental fluctuations for Sr and O in the LSCrF91 (Figure 4-7. d) follows the same trend. Their weight percentages increase and decrease together across the line. The same pattern has been characterized by other grains in this sample.

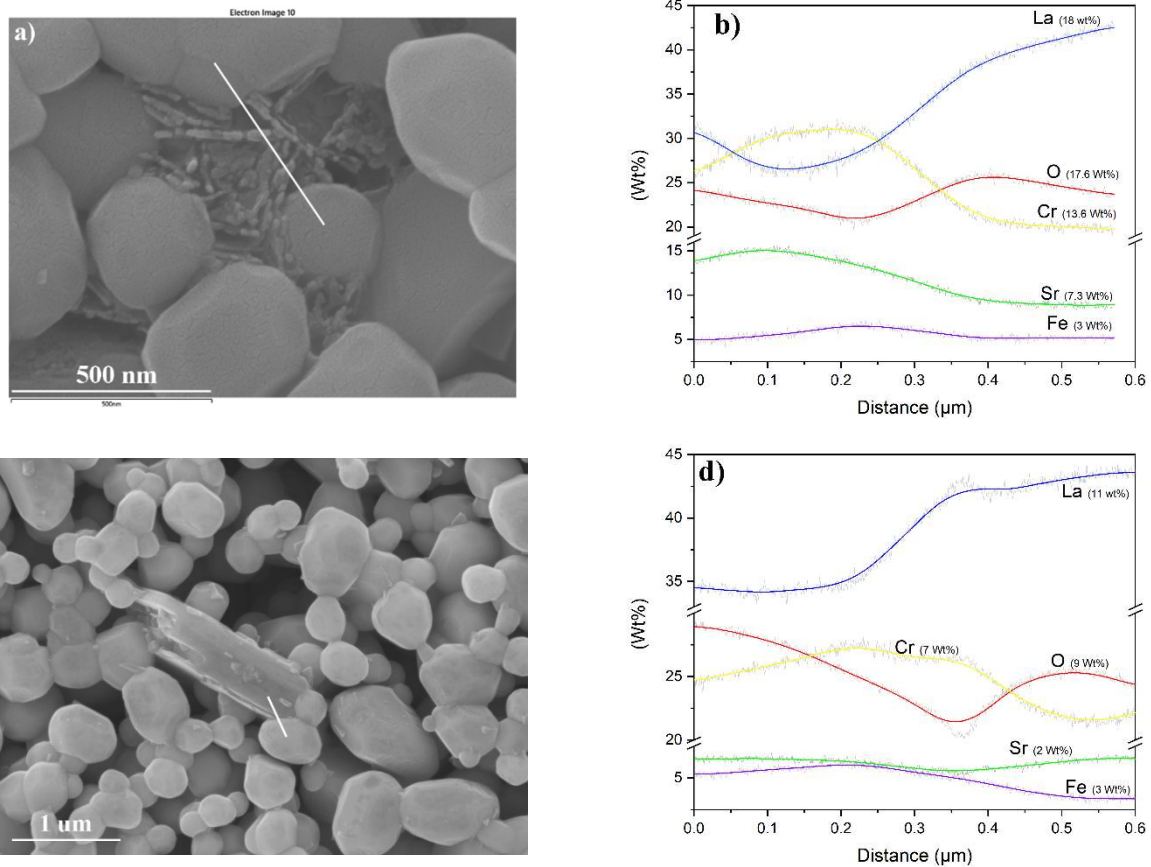


Figure 4-7. The SEM pictures of the heat-treated (a) LSCrF81 and (c) and (e) LSCrF91 together with their corresponding quantitative line scan analyses.

4. Discussion

4. 1) The Perovskite Phase Separation

The simulations in Figure 4-1 indicate that the phase separation in the perovskite phase can temporarily occur below 1000°C under reducing atmospheres. The initial perovskite structure is separated into two perovskite #1 and perovskite#2. It has also been shown that the occurrence of the phase separation can be affected by changes in temperature, $p(\text{O}_2)$, and Fe content (Figure 4-1, Figure 4-2, and Figure 4-4). This phenomenon can be explained by the disintegration of Sr and Fe dopants over changes in T and $p(\text{O}_2)$.

For the LSCrF91, the evidence for the formation of SrO in Figure 4-5.b and Figure 4-7.c and d can be referred to the formation of SrCrO_4 as an intermediate phase, which is liquid under $<1200^\circ\text{C}$ and acts as a sintering aid for LSCrF [96]. It can dissolve back to the perovskite structure as temperature and $p(\text{O}_2)$ change. However, a different mechanism is involved during the stability tests. The liquid phase of SrCrO_4 (Sr-liquid) squeezes out of samples while it cannot survive, reducing atmospheres. Accordingly, it has been decomposed into SrO and a Cr-oxide. This behavior has been already reported for lanthanum-based perovskites [98-101]. The point calculations on liquid#1 in Figure 4-2. a show that the segregated Sr mainly goes into the Liquid#1 at elevated temperatures. The Cr-oxide is now used to form the spinel structure with Fe. It is believed that Fe is provided by the reduction of Fe^{3+} ions into Fe^{2+} ions under reducing atmospheres. This reduction for Fe ion species leads to an increase in ionic radii from 0.65 Å for Fe^{3+} to 0.78 Å for Fe^{2+} . This occurs when Fe^{2+} is still in the B-site of the perovskite. Due to the bigger size of the ionic radii for Fe^{2+} ion in B-site, a further increase in the Fe^{2+} concentration cannot be tolerated inside the perovskite structure and results in releasing Fe from the structure. Now the spinel forms with Cr-oxide and this releasing Fe. The spinel phase is, indeed, a solid solution of Fe, Cr, and O in $(\text{Fe}_z\text{Cr}_{1-z})_{3-y}\text{O}_4$ formula [102]. The solubilities of Fe and Cr in the solid solution changes with temperature, $p(\text{O}_2)$, and the Cr: Fe ratio. The Cr: Fe ratio refers to the initial composition of the perovskite. Higher Cr and $p(\text{O}_2)$ are in favor of the corundum structure, while higher Fe at low $p(\text{O}_2)$ stabilizes the spinel structure [102]. It is believed that a second liquid phase is formed from the Fe-Cr-O solid solution (Spinel-liquid, liquid#2 in Figure 4-2.b). In contrary to the Sr-liquid phase (Liquid#1 in Figure 4-2.a), this spinel-liquid phase has been considered to be a high-temperature phase when initial perovskite is Cr-rich. It is expected to form only during the

sintering process ($>1200^{\circ}\text{C}$). However, as Fe content increases in initial perovskite structure, the solid solution of Fe-Cr-O eventually gets enriched from Fe during the sintering process, and its melting point drops. It has been previously reported by Gupta for highly Fe-doped LSCrF perovskites [56]. Now this liquid phase forming from spinel can form during even processing conditions at lower temperatures ($<1200^{\circ}\text{C}$) and interact with the SrO formation and Sr-liquid phase (Liquid#1). Figure 4-8 shows a new simulation about the correlation between Fe content in initial perovskite and the formation of SrO during stability test. As it can be seen, the SrO formation decreases with further increase in Fe as the B-site dopant in the perovskite. It can also explain why SrO has been detected only for the LSCrF91 in XRD patterns (Figure 4-5 .b). In fact, instead of forming SrO, the disintegrated Sr can be dissolved into the Fe-rich liquid phase at elevated temperatures.

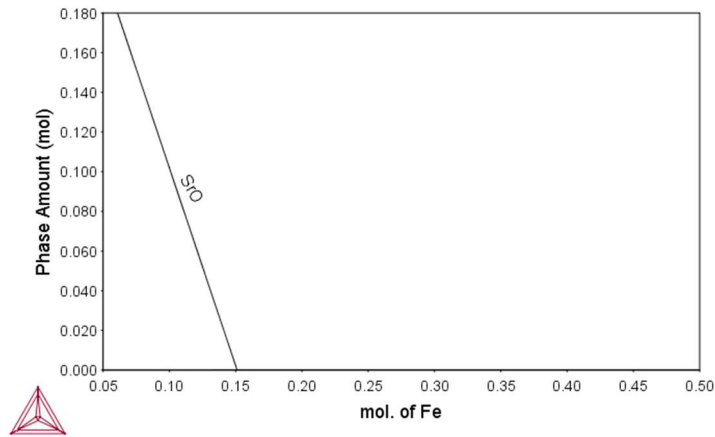


Figure 4-8. The formation of SrO with changes in the Fe content in the LSCrF91 ($T=850^{\circ}\text{C}$, $p(\text{O}_2)=10^{-18}$ atm).

Based on this mechanism, the total liquid phase will be enriched more from the dopants and leaves the initial perovskite depleted from Fe and Sr. This phenomenon can be the main reason for the phase separation. Indeed, the presence of Sr inside the perovskite structure is critical in defining its crystal structure and its orthorhombic \leftrightarrow rhombohedral phase transition [92]. Adding 0.1 mol of Sr to LaCrO_3 and LaFeO_3 can shift the phase transition temperature for ~ 200 and 700°C , respectively [92, 95]. Also, an increase in Fe on B-site of LSCrF changes its crystal symmetry from rhombohedral for high Cr: Fe ratios to orthorhombic for low Cr: Fe ratios at room temperature [43]. Owing to the importance of Fe and Sr dopants on crystal symmetries and phase transition

behavior of LSCrF, it is expected a dopant-depleted perovskite structure represents different crystal symmetry and phase transition behavior.

It is believed that the phase separation occurs for all compositions of LSCrF. However, the degradation in crystallographic symmetry from the rhombohedral to orthorhombic is only possible for Cr-rich LSCrF perovskites at room temperature. The reason is that, in these perovskites, the high-temperature rhombohedral symmetry has been stabilized at room temperature with the lowest possible amounts of dopants. Consequently, their crystal symmetries would be very sensitive to the disintegration in dopants. The current results show that this disintegration can occur during fabrication and processing conditions and leave a dopants-depleted perovskite structure. Later, after the cooling process, this new structure cannot adopt the high-temperature rhombohedral crystal symmetry at room temperature due to the shortage of dopants. It ends up in two perovskite structures: one is the major with initial stoichiometry and rhombohedral crystal symmetry at room temperature, the other is a secondary and new perovskite structure with deviation from the initial stoichiometry. Based on the simulation results in Figure 4-3, this new perovskite structure is rich from Fe in B-site. In this case, the new perovskite structure can be $\text{LaFeO}_{3-\delta}$, which has a rhombohedral symmetry at room temperature [95]. It means that Cr-rich LSCrF perovskite starts with the rhombohedral symmetry, but it will end up in two rhombohedral and orthorhombic symmetries after fabrication and processing conditions.

While the phase separation cannot be detected in XRD patterns (Figure 4-5), the anomaly in morphologies and elemental analysis in Figure 4-7 can be attributed to the solidification of the liquid phase with a different perovskite composition. It is believed that the grains with irregular shapes in Figure 4-7.c have been formed due to a fast cooling procedure. Severe elemental fluctuations in these grains can result in different perovskite structures. In the current research, they cannot be detected in XRD, probably due to either their low content or poor crystallizations. However, it is predicted that this phenomenon can be readily aggravated when LSCrF performs as an OTM, for example, with long working hours or when it is exposed to fast thermal cycles. This phase separation can promote a stoichiometric deviation through the perovskite structure.

4. 2) Dual-Phase Perovskite-Fluorite Composites

The investigation into the perovskite phase separation for the single-phase of LSCrF has been extended into dual-phase composites of LSCrF and 8YSZ. XRD pattern for the LSCrF91-8YSZ has been presented in Figure 4-9. a. Peaks for all phases have shifted to the left due to thermal and chemical expansions of unit cells. There are no peaks for the formations of SrZrO_3 (SZO), $\text{La}_2\text{Zr}_2\text{O}_7$ (LZO), or tetragonal YSZ phases in the LSCrF91-8YSZ sample. However, peaks attributed to the perovskite structure have left shoulders all along 2theta degrees (20-70°). Specifically, there are peak-splitting for the perovskite phase at ~32 and 47° (Figure 4-10. a and b). These two peaks are dedicated to the perovskite structure and have no overlaps with either the fluorite phase or other possible secondary phases. In comparison to the LSCrF91-8YSZ, the LSCrF55-8YSZ has no signs of the peak splitting (Figure 4-10. c. d). Further investigations by Reitveld refinement reveals that the perovskite structure in the LSCrF91-8YSZ has been composed of two major rhombohedral and minor orthorhombic structures after the stability test (Table 4-2). The strategy for the refinement is defined based on the SEM microstructural studies, XRD investigations, and simulated results. As the simulations results show that Fe content increases in the B-site of the perovskite#2 (Figure 4-2 and Figure 4-3), it has been assumed that the new perovskite structure is rich from Fe. Based on this, it is expected that it has an orthorhombic structure [95]. Accordingly, the perovskite #2 has been refined based on the $\text{LaFeO}_{3-\delta}$ structure (ICDD 01-084-6534). The reliability factors have been improved after considering this other orthorhombic perovskite structure for the LSCrF91-8YSZ sample (Table 4-2).

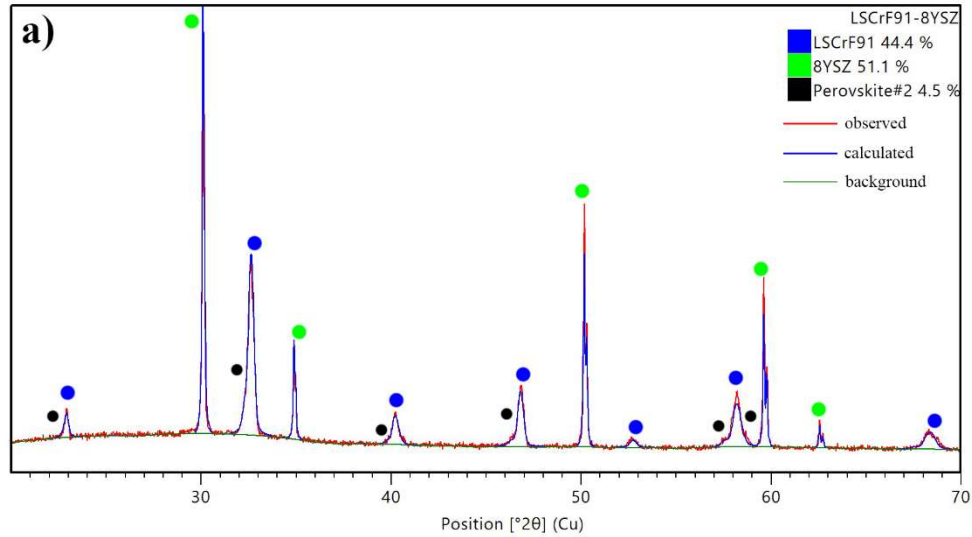


Figure 4-9. The XRD patterns for LSCrF91-8YSZ after heat-treating at 850°C for 10 hours under wet forming gas (4% H_2 -96%Ar).

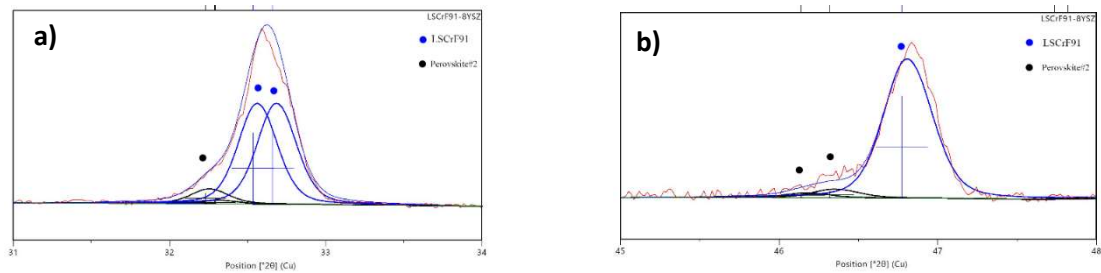


Figure 4-10. The analysis on peak shapes of LSCrF91-8YSZ after heat-treating at 850°C for 10 hours under wet forming gas (4% H_2 -96%Ar).

It is interesting because the existence of an orthorhombic symmetry for the LSCrF91 is not expected at room temperature. Indeed, the crystal structure for the LSCrF91 should remain as the rhombohedral symmetry ($R\bar{3}c$). The existence of the orthorhombic structure can be only explained by the perovskite phase separation phenomenon. It is believed that partitioning of dopants among secondary phases together with a fast cooling procedure leads to the formation and stabilization of a new perovskite structure with the orthorhombic symmetry. Since the orthorhombic \leftrightarrow rhombohedral phase transition is a first-order transition in the La-Sr-Cr-Fe-O system, these two phases can co-exist at one temperature. Fossdal has already reported that the appearance of the two-phase region for (La, Sr) FeO_3 depends on Sr content and temperature [95]. As temperature decreases, the area of the two-phase region becomes stable for a broader range of Sr content.

Table 4-2 The refined parameters for LSCrF91-8YSZ after the heat-treatment at 850°C for 10 hours under wet forming gas (4% H₂-96%Ar).

Refined parameters for LSCrF91 phase

Atoms	Site	X	Y	Z	U (Å ²)	SO F
La	6a	0.0	0.0	0.25	0.5	0.76
Sr	6a	0.0	0.0	0.25	0.5	0.19
Cr	6b	0.0	0.0	0.0	0.5	0.9
Fe	6b	0.0	0.0	0.0	0.5	0.1
O	18c	0.529	0.0	0.25	0.5	1.0

Crystal Structure: Rhombohedral, Space group: $R\bar{3}c$; Unit cell parameters: a=b=5.49837 Å, c=13.39407 Å, $\alpha=\beta=90^\circ$, $\gamma=120^\circ$; Unit cell volume: 350.6801 Å³; Chemical formula: (La_{0.8}Sr_{0.2})_{0.95}(Cr_{0.9}Fe_{0.1})O_{3±δ}; ICDD 04-013-5267.

Refined parameters for 8YSZ phase

Atoms	Site	X	Y	Z	U (Å ²)	SOF
Zr	4a	0.0	0.0	0.0	1.43	0.84
Y	4a	0.0	0.0	0.0	1.43	0.16
O	8c	0.25	0.25	0.25	1.15	0.34
O	48g	0.3	0.25	0.25	1.15	0.08 5

Crystal Structure: Cubic, Space group: Fm-3m; Unit cell parameters: a=b=c=5.1395 Å. Unit cell volume: 135.7571 Å³, $\alpha=\beta=\gamma=90^\circ$; Chemical formula: Zr_{0.786}Y_{0.214}O_{1.7}; ICDD 01-077-2286.

Refined parameters for Perovskite#2 phase

Atoms	Site	X	Y	Z	U (Å ²)	SOF
La	4c	0.028	0.25	-0.007	0.5	1.0
Fe	4b	0.0	0.0	0.5	0.26	1.0
O	4c	0.488	0.25	0.066	0.6	1.0
O	8d	0.287	0.465	-0.284	0.55	1.

Reliability Factors $R_{wp}=7.66\%$ $R_p=5.75\%$ $R_{exp}=5.22\%$ GOF=2.7972

Crystal Structure: Orthorhombic, Space group: Pbnm; Unit cell parameters: a=5.53871, b=7.86213, c=5.53946 Å, $\alpha=\beta=\gamma=90^\circ$; Unit cell volume: 241.2219 Å³; SOF: site of fraction; x, y, z: Fractional coordinates; U: Isotropic atomic displacement parameter; Chemical formula: LaFeO₃; ICDD 01-084-6534.

Furthermore, it is vital to study the difference in the chemical stability of the single-phase LSCrF91 and LSCrF91-8YSZ composite. The phase separation can be detected by XRD for dual-phase samples, but it cannot be recognized for XRD patterns of single-phase perovskites. Discrepancies in the chemical stability of single-phase LSCrF and dual-phase LSCrF-8YSZ have been already reported in separate studies by He and Liu [45, 103]. In the current research, it is believed that the capability of the perovskite phase to re-produce its structure during thermal cycles has been compromised due to the presence of 8YSZ as the adjacent phase.

Regardless of the characterizing the two-phase perovskite of the LSCrF91-8YSZ, it is very challenging to determine the dominant parameter for the phase separation. The final crystal symmetry in the LSCrF is defined by temperature, oxygen nonstoichiometry (δ), and compositions (dopants). An increase in temperature and δ is in favor of higher symmetries, while the effect of composition depends on contents and ionic radii of A-site and B-site dopants. Also, due to be constrained by YSZ grains, the level of stress for LSCrF-8YSZ samples is different, compared to single-phase LSCrF samples. Since both LaCrO_3 and LaFeO_3 are ferroelastic phases, the phase transition behavior can be affected by the ability to relieve stress. The differences have been previously investigated among fine grain powder, chunks, and bulk samples of $(\text{La, Sr}) \text{FeO}_{3\pm\delta}$ [95]. In the LSCrF-8YSZ samples, all these parameters are involved, and they can interact with each other. Hence, it would be very challenging to recognize which parameter is dominant to control the phase separation. This is the subject of the next investigation.

5. Conclusion

In this research, a new phenomenon as the perovskite phase separation has been investigated for LSCrF perovskites and dual-phase LSCrF-8YSZ composites. The results show that the disintegration of dopants and their partitioning among secondary phases occurs even for Cr-rich LSCrF perovskites. Owing to the simultaneous use of characterization methods and computational Thermodynamic, the mechanism, which leads to the phase separation, has been unraveled for the first time. It can explain the behavior of the perovskite when their structures are either lightly or heavily doped on A-site and B-site.

The simulation results for the perovskite reveal that the phase separation occurs between ~ 700 to $\sim 1000^\circ\text{C}$. The XRD patterns with Reitveld refinements prove the existence of the two rhombohedral and orthorhombic symmetries for the perovskite in the LSCrF91-8YSZ composites.

The extent and behavior of the phase separation can be manipulated by changes in T , $p(\text{O}_2)$, and the Cr: Fe ratio. It is vital because this is the processing temperature range for OTM and SOFC applications. It is predicted that the reported phase separation will be aggravated during applications of OTM with $>40,000$ hours lifelong. The phase separation can lead to a deviation in stoichiometry over thermal cycles so that it can make detrimental changes in thermal expansion behavior and mass transport properties.

The use of computational Thermodynamic enables us to examine wide ranges of temperature and $p(\text{O}_2)$. The approach helps to study the trend of the system with changes in the parameters. It can unravel complicated correlations of involved parameters to enhance the chemical stability of LSCrF. This provides the essential capability to design LSCrF materials and optimize their performance.

Chapter 5 : The Chemical Stability of Dual-Phase Composites of (La, Sr)(Cr, Fe)O_{3-δ}- 8YSZ, 10Sc1YSZ, and 10Sc1CeSZ

Plan to publish in Journal of Alloys and Compounds

Abstract

The chemical stability between perovskite and fluorite structure is a challenge for designing dual-phase ceramic membranes. The current research investigates the chemical stability of (La_{0.8}Sr_{0.2})_{0.95}Cr_{0.5}Fe_{0.5}O_{3-δ} with three fluorite phases of 8YSZ, 10Sc1YSZ, and 10Sc1CeSZ. The changes in the Sr-content and the Cr: Fe ratio in the perovskite phase have been also investigated under oxidizing and reducing atmospheres at elevated temperatures. The results show that SrZrO₃ as the dominant secondary phase together with limited formations of (La_{0.5}Zr_{0.5})O_{1.75} and La₂O₃. The experimental results have been incorporated into simulations performed by computational Thermodynamic. Involved mechanisms to improve the chemical stability have been discussed based on correlations among the content of dopants and applied conditions. The results enhance knowledge about designing dual-phase ceramic membranes.

1. Introduction

There is a high demand for oxygen as the most used gas in the modern industrial process [4, 6, 8]. While oxygen is available in air, the production of pure oxygen is still difficult and expensive, especially for massive scale productions. One of the state-of-the-art methods for oxygen production is to use materials that can conduct oxygen ions through their crystal lattices [6, 83, 104]. Perovskite structures with electronic and ionic conductivities have recently received lots of attention as oxygen transport membranes (OTM) [3, 8]. In this approach, a perovskite material with mixed ionic-electronic conductivity (MIEC) is subjected to two different atmospheres with distinct oxygen potentials. At high temperatures (700-1000°C), oxygen ions can transport from high oxygen side to low oxygen side while the total electrical charge neutrality in the crystal lattice is maintained with a counterbalance of electrons movement at the opposite direction [6, 8]. The mechanical advantage of the perovskite-based membranes is for integration in power generation cycles with carbon dioxide (CO₂) capture for oxy-fuel combustion [8, 105].

A perovskite structure for OTM applications should meet a long list of requirements to reliably act as an OTM [3, 76]. It should work in the temperature range of 700 to 1000°C under a sharp slope of oxygen partial pressure ($p(\text{O}_2)$) between 0.21 to 10⁻²² atm. The material should survive these conditions over 40,000 hours to be commercially successful [106]. While remarkable advances have been conducted to prepare perovskite structures for OTM applications, it is still challenging to find a single perovskite structure to

meet all the requirements. The main problems for the perovskite structures are related to maintaining their mechanical and chemical stabilities for long-term operation at high temperatures and reducing atmospheres. One strategy to tackle this issue is to design dual-phase composite membranes.

In dual-phase composite membranes, there is a highly stable phase with high oxygen ionic conduction and limited electronic conductivity. Its limited electronic conductivity is compensated by adding another electronic conductor phase. This promising design has received attention during the past years [87, 103, 107-109]. The next section provides a brief review of dual-phase ceramic membranes and indicates current challenges for this design.

2. Previous Investigations in Dual-Phase Ceramic Membranes

The advent of dual-phase composites with the close concept to current ceramic membranes can be traced back to investigations into “electrocatalytic cells for chemical reaction” [110]. They have used strips of Au and Pt for coating on YSZ to partially oxidize methane and to produce ethane. The trend of using ceramic ionic conductors with noble metals have been then followed with others in the following years [111]. Chen et al. reported dual-phase composites of YSZ-Pd, erbia-stabilized bismuth oxide with gold and silver, and measured oxygen permeation fluxes from airside to the helium side at elevated temperatures [112, 113]. The temperature range for YSZ was 800-1100°C and 650-850°C for bismuth oxides. Based on the reported results, bismuth oxide (δ -Bi₂O₃) presents the best oxygen permeation flux; however, it suffers from low chemical stability at high temperatures (~627°C). Plus, their performance degrades due to interactions between silver and the bismuth oxide. Also, owing to the high cost of noble metals, their usage as electronic conductors for dual-phase composites was not a promising approach for practical applications. At the beginning of the 2000s decade, there was a need for a new inexpensive material with reliable electronic conductivity at high temperatures, which is chemically stable over wide ranges of oxygen partial pressure ($p(\text{O}_2)$). La-based perovskite structures with transition metals on B-site are one of the structures which can cope with these criteria. Based on this, the approach for materials development in dual-phase composites was bent toward fluorite-perovskite composites. Kharton et al. studied Ce_{0.8}Gd_{0.2}O_{2- δ} -La_{0.7}Sr_{0.3}MnO_{3- δ} composite membranes with a focus on oxygen permeation [17]. They reported a decrease in oxygen permeation due to diffusion of metallic cations (Mn, La, and Sr) from the perovskite side to CGO and formations of secondary phases in grain boundary areas. Regardless of these problems, overall results for using of La-based perovskites with fluorite phases seemed to be a promising combination for dual-phase ceramic membranes. In the following years, many kinds of research have been conducted to find the best compositions of perovskites which are compatible with fluorite phases [103, 113-117].

Lanthanum chromite-based perovskite has been a prime candidate for dual-phase composites, as well. One of the first investigations into this field has been conducted by Wang et al. [118]. They designed tubular dual-phase composite membranes with $Zr_{0.8}Y_{0.2}O_{0.9}-La_{0.8}Sr_{0.2}CrO_{3-\delta}$ and measured oxygen permeation at 1000°C for 500 hours. The feeding gas was ambient air, and the fuel gases were alternated between pure helium and helium-diluted CO. While the membrane could chemically survive the condition, they reported oxygen surface exchange stage as the rate-limiting stage for oxygen permeation flux. In the following years, further investigations revealed that the surface oxygen exchange acts as a key step for oxygen permeation in perovskite-fluorite dual-phase membranes. In fact, in these membranes, the surface oxygen exchange only occurs at the tree phase boundaries (TPB) of gas/ oxygen ion conductor/ electron conductor. Compared to YSZ-Pd membranes, the surface process for perovskite-fluorite dual-phase membranes is low because the perovskite phase has only electronic conductivity and remains inactive toward the surface reaction. To tackle this problem, two approaches have been conducted. The first approach is to improve the surface oxygen activity of the perovskite phase by performing some surface modifications. This includes changes in the design, such as scaffold structures or hollow fibers, coating with nanoparticles, or infiltration techniques [103, 116, 119, 120]. The second approach is to enhance the ionic conductivity feature of the perovskite phase by adding dopants [8, 119, 121]. In some works of literature, both techniques have been deployed simultaneously to boost oxygen permeation [87]. The approach of using dopants is desirable because it promotes the ionic conduction of the perovskite phase not only on its surface but also inside its bulk. In general, as oxygen ions transfer inside the membrane, they will have the perovskite phase as an alternative passage for their movement. This concept has been schematically shown in Figure 5-1.

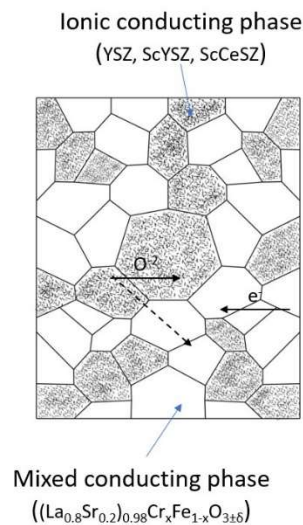


Figure 5-1. A schematic microstructure of a dual-phase composite of LSCrF-YSZ and transporting electrons and oxygen ions through different grains. Inspired by [8].

Adding Fe as B-site dopants to (La, Sr)CrO_{3-δ} increases oxygen vacancy inside the perovskite structure under reducing atmospheres, so it improves the ionic conductivity of the perovskite [43]. Accordingly, many kinds of research on dual-phase composites have been narrowed down on (La,Sr)(Cr,Fe)O_{3-δ} and fluorite phases. There are interesting researches on oxygen permeation of LSCrF/YSZ dual-phase membranes [42, 86, 87, 89, 103, 114, 121, 122]. Liu et al. measured the oxygen permeation rate in La_{0.8}Sr_{0.2}Cr_{0.5}Fe_{0.5}O_{3-δ}-Zr_{0.84}Y_{0.16}O_{1.92} dual-phase composite hollow fiber membrane under air/CO atmosphere and at 950°C [103]. The hollow fibers could survive 500 h without apparent changes in microstructure. Liu and Wu designed a tri-layered “porous|dense|porous” OTM from La_{0.8}Sr_{0.2}Cr_{0.5}Fe_{0.5}O_{2-δ}-Zr_{0.84}Y_{0.16}O_{2-δ} to enhance oxygen permeability under air/CH₄ atmosphere [123]. To reach reasonable oxygen permeation under low temperatures (650-800°C), they applied the nano-scale catalyst coating of La_{0.6}Sr_{0.4}Co_{0.2}Fe_{0.8}O_{3-δ} (airside) and Ce_{0.8}Sm_{0.2}O_{1.9-δ}/Ni (methane side) on porous layers. However, LSCrF/c-YSZ (cubic-YSZ) as a dual-phase composite for OTM usages has faced some challenges, as well. Fang et al. examined the oxygen permeability of the asymmetric membrane of La_{0.8}Sr_{0.2}Cr_{0.5}Fe_{0.5}O_{2-δ}-Zr_{0.8}Y_{0.2}O_{2-δ} under oxidizing and reducing atmospheres in the temperature range of 750-900°C[86]. Their results reveal acceptable oxygen permeability under air/CO and CO₂/H₂ gradient; however, oxygen flux is lower than expected. It is suggested that a better understanding of the chemical defect of the membrane is needed. Cheng et al. made composites of LSF-YSZ and LSCrF-YSZ electrode scaffolds and reported detrimental migration of Zr into LSF structure[120]. They showed that reducing Sr content and adding Cr in B-site could minimize this deleterious migration. However, the poor sintering characteristics due to adding Cr caused incomplete densification in electrolyte (YSZ) and poor electrode microstructure. On the perovskite side alone, it has been also reported that increase in Fe in LSCrF improves ionic conductivity, oxygen permeation, and densification [43, 54, 56]. However, as Fe content increases in the perovskite, some undesirable phases like spinel, iron oxides, and even liquid phase can be formed depending on applied p(O₂), composition, and temperature [54, 56]. Hence, one of the current challenges in designing LSCrF/c-YSZ is to optimize LSCrF composition regarding to applied conditions and to find the best ratio between these two phases. Investigation into thermochemical stability between these two phases is a pertinent approach to address these challenges.

Thermochemical stability in the dual-phase composites of LSCrF-fluorite can be investigated in three levels: bulk chemical stability, interface chemical stability, and surface segregation. In the current research, we have focused on the bulk thermochemical stability with changes in p(O₂), temperature, Sr content, Cr: Fe ratio, and fluorite phases of YSZ, ScYSZ, and ScCeSZ. Two approaches of experimental and computational Thermodynamic have been conducted to examine the quality of chemical stability and formations of secondary phases. The use of computational Thermodynamic helps to reduce the number of experimental tests and examine different conditions/ compositions. This trend together with experimental

observations, provides a comprehensive understanding of involved degradation mechanisms and solid-state interactions between the perovskite and fluorite phases. The results can develop fabrication and processing techniques for dual-phase ceramic membranes.

3. Experiments

In the current research, the raw powders of perovskites and fluorites have been provided by Praxair, Inc. Five different compositions of $(\text{La}_{0.8}\text{Sr}_{0.2})_{0.95}\text{Cr}_x\text{Fe}_{1-x}\text{O}_{3-\delta}$ (LSCrF) ($x=0.9, 0.8, 0.7,$ and 0.5) and three different compositions of stabilized zirconia have been investigated in this study. The examined compositions have been listed in Table 5-1. The compositions of LSCrF changes with the Cr: Fe ratio and Sr-content. Two different Sr-content have been examined. As the fluorite phase, dopants to the stabilized cubic phase of ZrO_2 changes among Ytria, Scandia-Ytria, and Scandia-Ceria.

Table 5-1. The list of examined compositions of perovskite and fluorite.

	Composition	Abbreviation
Perovskites	$(\text{La}_{0.9}\text{Sr}_{0.1})_{0.95}\text{Cr}_{0.7}\text{Fe}_{0.3}\text{O}_3$	LS1CrF73
	$(\text{La}_{0.8}\text{Sr}_{0.2})_{0.95}\text{Cr}_{0.9}\text{Fe}_{0.1}\text{O}_3$	LS2CrF91
	$(\text{La}_{0.8}\text{Sr}_{0.2})_{0.95}\text{Cr}_{0.8}\text{Fe}_{0.2}\text{O}_3$	LS2CrF82
	$(\text{La}_{0.8}\text{Sr}_{0.2})_{0.95}\text{Cr}_{0.7}\text{Fe}_{0.3}\text{O}_3$	LS2CrF73
	$(\text{La}_{0.8}\text{Sr}_{0.2})_{0.95}\text{Cr}_{0.5}\text{Fe}_{0.5}\text{O}_3$	LS2CrF55
Fluorites	8mol% (Y_2O_3) -(ZrO_2) (Tosoh)	8YSZ
	10mol% (Sc_2O_3) -1mol% (CeO_2) - ZrO_2	10Sc1CeSZ
	10mol% (Sc_2O_3) -1mol% (Y_2O_3) - ZrO_2	10Sc1YSZ

The dual-phase composite samples have been prepared by milling perovskites and fluorite in acetone together with Saint-Gobain ZirPro ceramic grinding media (Zirmil®Y). The milling has been continued for over 6 hours. The resultant powders have been screened and pressed by a uniaxial press. The sizes of the disk-like pellets are 13 and 1 mm for their diameter and thickness, respectively. In order to minimize the effect of thermal history in the samples, they have been only sintered at 1150°C under air for 2 hours to have enough densification and mechanical stability for further analysis.

The chemical stability of the pellets has been examined under the fabrication and processing conditions of OTMs and SOFCs [3, 8, 16, 40, 77]. For fabrication conditions, the samples have been passed heat treatments at 1400°C for 10 hours under three different $p(\text{O}_2)$: pure argon (99.999%), 0.1% H_2 -Ar (forming gas 1), and ambient air. All reducing gases have been provided by the Airgas company. For

processing conditions, the temperature is 850°C under 4%H₂-Ar gas (forming gas 2) with 10 hours as the soaking time. This is called the “stability test” through the paper. For heating the samples, a tube furnace from MTI Corporation with three different heating zones have been utilized. All samples have been cooled fast through removing them from the furnace above 1300 and 750°C in the heat treatments and the stability test, respectively. After removing the pellets, they have been set on cold alumina wafers to reach room temperature. Oxygen partial pressure (p(O₂)) for all heating procedures has been continuously tracked by monitored by Rapidox 2100 Gas Analyzer until the samples have been removed from the furnace. The flow rate of gases is set to 100 mL/min for all tests. Before sending gases into the furnace, the reducing gases have passed through deionized water in a humidity bottle in order to control p(O₂). Further information on this technique can be found in this reference [37].

The crystal structure of the samples has examined with X-ray Diffraction with a Cu tube (PANalytical EMPYREAN) in the range of 20-120°. Changes in crystal symmetry, formations of secondary phases, and phase contents have been studied by the Rietveld X-ray refinement method and HighScore Plus software (version 4.8). The phase structures have been analyzed using the International Center for Diffraction Data (ICDD) and PDF-4+ database. This procedure has been deployed for all sintered and heat-treated samples. Refined parameters include background, zero shift, specimen displacement, lattice parameters, wave functions, and asymmetrical parameters. Oxidation states of ions have been also factored in, and the peak shape has been modeled by pseudo-Voigt functions. Occupancy of atoms and their coordination have not been refined. Throughout the paper, phases are called by their first letter in XRD patterns. According to this coding procedure, P, F, S, and L are using to refer to perovskite, fluorite, SrZrO₃ (SZO), and La₂Zr₂O₇/ (La_{0.5}Zr_{0.5})O_{1.75} (LZO) phases, respectively.

The microstructure of the sample has been studied by Scanning Electron Microscopy (SEM) (JEOL JSM-7000F) coupled with Energy-dispersive X-ray Spectroscopy (EDS) (Oxford Instrument X-MAX^N). The samples have been lightly coated by a sputter coating device with the Au/Pd target. SEM and EDS results have been analyzed by Aztec software from the Oxford instrument. The contributions of Au and Pd elements have been removed from EDS analyses by software.

4. Computational Thermodynamic

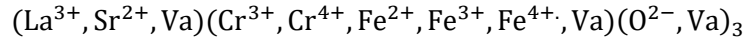
In the current research, computational Thermodynamic has been conducted by the CALPHAD approach. In the CALPHAD approach, first-principle calculations as theoretical data and experimental Thermodynamic data are deployed to define Gibbs energy descriptions, develop databases, and extend them

to higher-order systems. Further information about the CALPHAD approach can be found in these references [16, 124].

a. Thermodynamic databases and models

The database in the current research has been developed from previously published databases for sub-systems of La, Sr, Fe, Cr, O, Zr, and Y elements [20, 21, 24, 25, 97, 125]. Accordingly, only interactions between LSCrF and YSZ have been modeled in this study. The databases have been specially developed for SOFC applications based on phase stability, stoichiometry, and defect chemistry analysis in different conditions. The assessed database of La-Sr-Cr-Fe-O-Y-Zr has been merged with the Scientific Group Thermodata Europe Substances Database (SSUB-5) similar to the work performed by Darvish et al. and Sabarou et al. [13, 16].

The perovskite structure has been modeled based on the three sublattices:

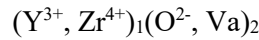


Where Va represents vacancy in different sublattices. The Gibbs energy definition for the perovskite phase is defined based on the below term:

$$G_m = \sum_{i,j,k} y_i y_j y_k \circ G_{i,j,k}^{\text{Perov}} + RT \cdot \left(\sum y_i \ln y_i + \sum y_j \ln y_j + 3 \sum y_k \ln y_k \right) + {}^E G_m^{\text{Perov}}$$

where y_i represents the A-site cations site fraction, y_j is the B-site cations site fraction, y_k represents the site fraction of species in the oxygen site, $\circ G_m^{\text{Perov}}$ is the Gibbs energy of perovskite endmembers and ${}^E G_m^{\text{Perov}}$ is the excess Gibbs energy of the solid solution perovskite phase.

The YSZ fluorite phase has been modeled based on two sublattices [26]:



The Gibbs energy term for the fluorite phase has been defined as below:

$$G_m = y_{\text{Y}^{3+}} y_{\text{O}^{2-}} \circ G_{\text{Y}^{3+}\text{O}^{2-}} + y_{\text{Zr}^{4+}} y_{\text{O}^{2-}} \circ G_{\text{Zr}^{4+}\text{O}^{2-}} + y_{\text{Y}^{3+}} y_{\text{Va}} \circ G_{\text{Y}^{3+}\text{Va}} + y_{\text{Zr}^{4+}} y_{\text{Va}} \circ G_{\text{Zr}^{4+}\text{Va}} \\ + RT [y_{\text{Y}^{3+}} \ln y_{\text{Y}^{3+}} + y_{\text{Zr}^{4+}} \ln y_{\text{Zr}^{4+}} + 2(y_{\text{O}^{2-}} \ln y_{\text{O}^{2-}} + y_{\text{Va}} \ln y_{\text{Va}})] + {}^E G_m$$

where y_i is the fraction of the species i in a particular sublattice.

Also, there are other phases in the system as the secondary phase. Spinel as a solid solution among Cr-Fe-O is modeled with three sublattices, i.e. $(\text{Cr}^{2+}, \text{Cr}^{3+}, \text{Fe}^{2+}, \text{Fe}^{3+})_1(\text{Cr}^{3+}, \text{Fe}^{2+}, \text{Fe}^{3+}, \text{Va})_2(\text{O}^{2-})_4$. SrZrO_3 has been modeled by three sublattices, i.e. $(\text{Sr}^{2+})_1(\text{Zr}^{4+})_1(\text{O}^{2-})_3$.

The contributions of Ar, H₂, and H₂O have been also added to the La-Sr-Cr-Fe-O-Y-Zr database. It includes Gibbs energies of stoichiometric compounds and the gas phase from SSUB-5. To simulate wet forming gases, saturated water vapor has been considered based on the temperature of the humidity bottle in the experiments [37].

5. Results

The investigation into the chemical stability of the samples has been initially examined by X-ray diffraction. It has been then completed with performing Reitveld refinement on each sample and operating SEM and EDS. This combination of analytical techniques provides a comprehensive image of the chemical stability on the dual-phase composite samples.

Based on XRD and Rietveld refinement results, the crystal symmetry of the perovskite phase is the rhombohedral ($R\bar{3}c$) for the Cr: Fe ratio of 9:1 and 8:2. It changes to the orthorhombic symmetry (Pnma) for the Cr: Fe ratio of 7:3 and 5:5. This is in a good agreement with previous reports and findings in the previous chapter [96]. No cubic phase for the perovskite structure has been observed in this study. The refinement process for the fluorite phases has been conducted with special attention toward formations of the tetragonal and monoclinic phases in 8YSZ and the rhombohedral phase in 10Sc1YSZ and 10Sc1CeSZ. According to high angle investigations, no sign of the secondary phases can be detected for the fluorite phases.

Figure 5-2 presents the XRD pattern of the LS2CrFe73-8YSZ after the heat treatment under forming gas 1. This sample represents one of the structures, which can successfully tolerate harsh conditions without forming secondary phases or decomposing. Accordingly, it can be considered as an example of a prepared structure in its ideal condition.

Its microstructure has been also presented in Figure 5-3 together with its EDS map analysis. This microstructure is exemplified the schematic pattern in Figure 5-1. Pink grains present the fluorite phase while yellow grains are for the perovskite phase. The perovskite grains seem to be partially corroded, compared to the grains of the fluorite phase. This microstructure has been used through the paper as the ideal and expected structure. Later, it also acts as criteria to examine the extent of deviations from expected microstructures for these systems.

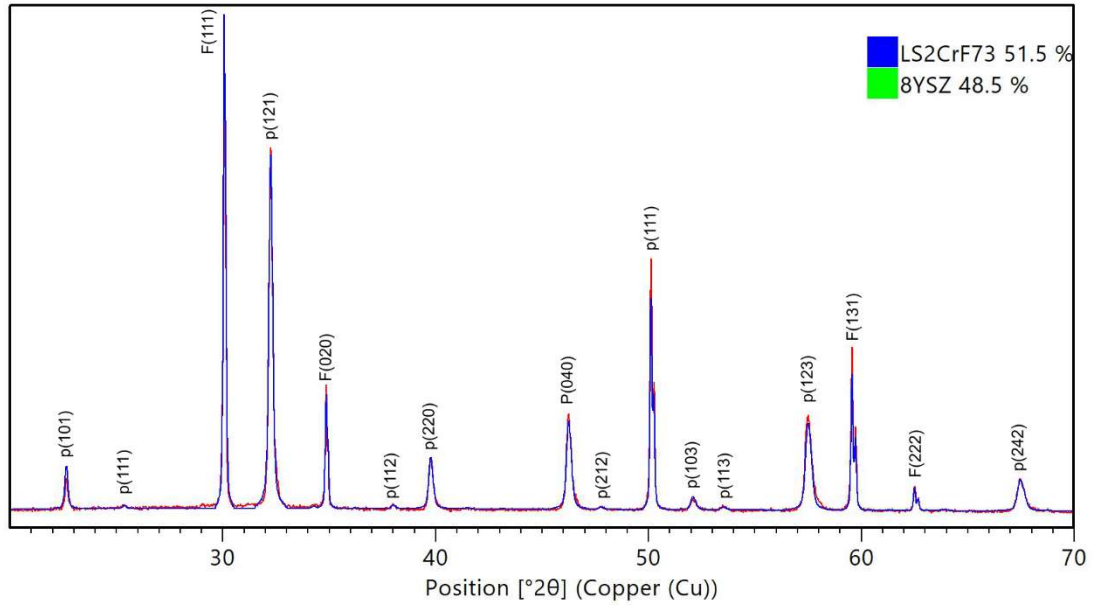


Figure 5-2. The XRD pattern for $(\text{La}_{0.8}, \text{Sr}_{0.2})_{0.95}\text{Cr}_{0.7}\text{Fe}_{0.3}\text{O}_{3-\delta}$ -8YSZ after heating at 1400°C for 10 hours under forming gas 1 (wet-0.1% H_2 -Ar).

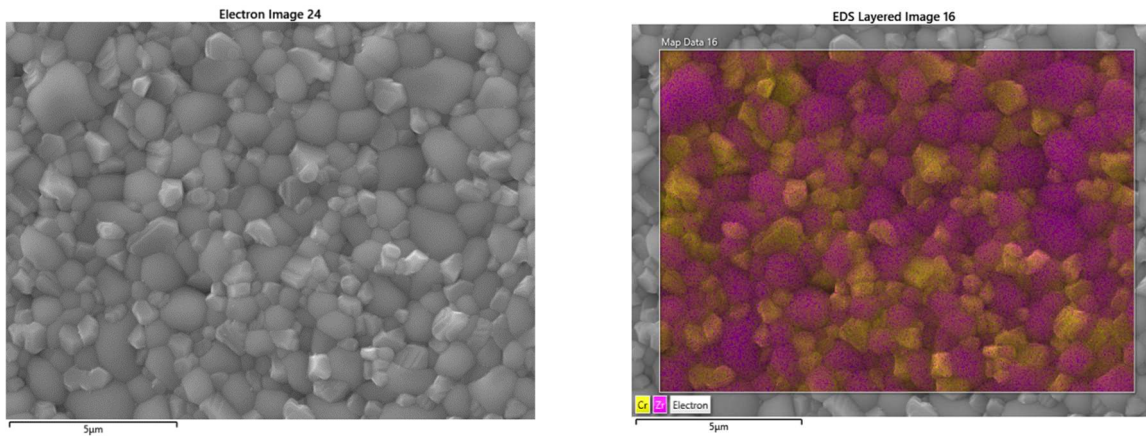


Figure 5-3. The Microstructure analysis for $(\text{La}_{0.8}, \text{Sr}_{0.2})_{0.95}\text{Cr}_{0.7}\text{Fe}_{0.3}\text{O}_{3-\delta}$ -8YSZ after heating at 1400°C for 10 hours under forming gas 1 (wet-0.1% H_2 -Ar).

Regardless of samples with reliable chemical stabilities, there are some samples with formations of secondary phases. The most common secondary phases are SrZrO_3 (abbr. SZO) and spinel solid solution of Fe-Cr-O. SZO has not been detected for samples of heat-treated under air. Also, it is rare to see the spinel phase in XRD patterns, but its grains can be found under SEM.

There are also few samples with $(\text{La}_{0.5}\text{Zr}_{0.5})\text{O}_{1.75}$ (abbr. LZO) and La_2O_3 . Formations of spinel, SZO, and LZO phases have been already reported for either single-perovskite systems or similar $(\text{La}, \text{Sr})\text{MnO}_{3-\delta}$ – YSZ systems [16, 50, 54, 56]. The formation of a liquid phase and phase separation in perovskite have been also detected and investigated for some samples. The second perovskite has been

analyzed based on $\text{LaFeO}_{3-\delta}$ with the orthorhombic structure. Further information on the perovskite phase separation can be found in the previous chapter. The list of all analyzed phases in this investigation has been collected in Table 5-2.

Table 5-2. The list of the analyzed phases with their reference card numbers and crystal structures.

Phase	ICDD Card Number	Crystal Structure (symmetry)
(La,Sr)(Cr,Fe)O_{3-δ}	04-013-5267	Rhombohedral ($R\bar{3}c$)
(La,Sr)(Cr,Fe)O_{3-δ}	04-013-5265	Orthorhombic (Pnma)
LaFeO_{3-δ}	01-084-6534	Orthorhombic (Pbnm)
YSZ	01-077-2286	Cubic (Fm-3m)
ScYSZ	04-016-6138	Cubic (Fm-3m)
ScCeSZ	04-022-1613	Cubic (Fm-3m)
La₂O₃	03-065-3185	Cubic (Ia-3)
SrZrO₃ (SZO)	01-076-0167	Cubic (Pm-3m)
(La_{0.5}Zr_{0.5})O_{1.75} (LZO)	01-085-6856	Cubic (Fm-3m)
Fe₂CrO₄ (Spinel)	01-084-4061	Cubic (Fd-3m)

In the current research, in order to recognize correlations between essential parameters involved in the chemical stability, results have been presented in separate sections. Later, in the discussion part, the correlations among parameters and their corresponding effects on the chemical stability have been explained with the help of computational Thermodynamic.

a. The Effect of $p(\text{O}_2)$

Three different atmospheres have been applied to the system at 1400°C for 10 hours. They include from oxidizing (ambient air - $p(\text{O}_2)=0.21$ atm) to reducing (argon - $p(\text{O}_2)\sim 10^{-4}$ atm) and very reducing (forming gas 1 - $p(\text{O}_2)\sim 10^{-17}$ atm) atmospheres. Figure 5-4 presents several X-ray diffraction patterns for different fluorite phases after heat treating under argon for 10 hours. In all samples, the fluorite phases can survive the conditions.

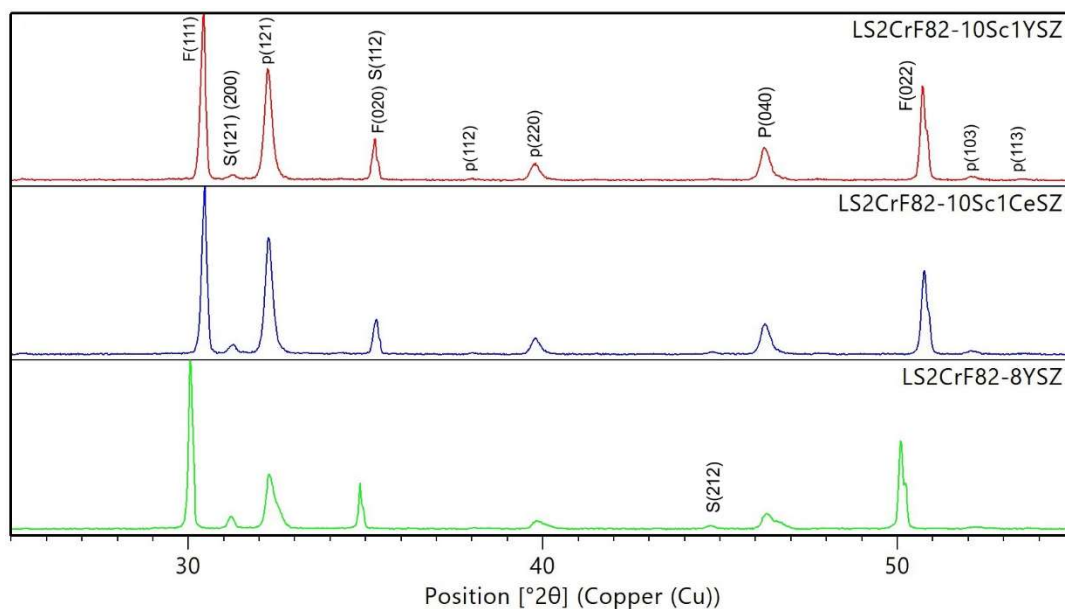


Figure 5-4. XRD patterns for $(\text{La}_{0.8}, \text{Sr}_{0.2})_{0.95}\text{Cr}_{0.8}\text{Fe}_{0.2}\text{O}_{3-\delta}$ -fluorite phases after heat treatment under argon for 10 hours.

The formation of SZO is common for samples heat-treated under reducing atmospheres. The Reitveld results reveal that SZO content can alternate between ~2.2 to 6.2 Wt.%. Figure 5 shows the XRD patterns for LS2CrF91-10Sc1CeSZ after heat treatments under different $p(\text{O}_2)$. Its content mainly depends on $p(\text{O}_2)$ so that lower $p(\text{O}_2)$ can promote its formation. It seems that the Cr: Fe ratio also leaves effects on the formation of SZO. The effect of the ratio on SZO has been examined in the next section.

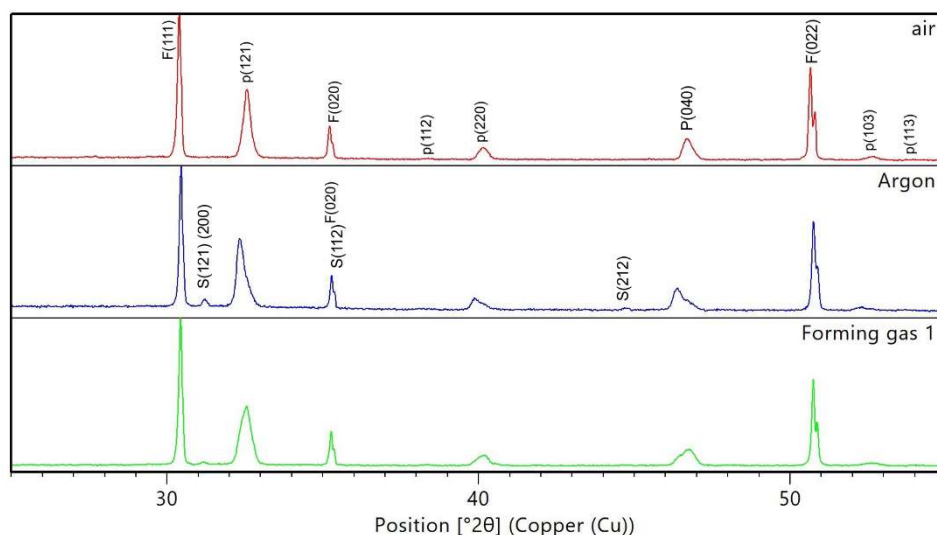


Figure 5-5. XRD patterns for $(\text{La}_{0.8}, \text{Sr}_{0.2})_{0.95}\text{Cr}_{0.9}\text{Fe}_{0.1}\text{O}_{3-\delta}$ -10Sc1CeSZ after heat treatment at 1400C for 10 hours, forming gas 1 (wet-0.1% H_2 -Ar).

b. The Effect of Sr

Due to the wide formation of SZO for most samples, the effect of Sr-content has been examined separately. In the first level, Sr content alternates between two values of 0.095 and 0.19 when the Cr: Fe ratio is fixed to 7:3 for both. This design provides two different perovskite compositions: $(\text{La}_{0.8}\text{Sr}_{0.1})_{0.95}\text{Cr}_{0.7}\text{Fe}_{0.3}\text{O}_{3-\delta}$ and $(\text{La}_{0.8}\text{Sr}_{0.2})_{0.95}\text{Cr}_{0.7}\text{Fe}_{0.3}\text{O}_{3-\delta}$. Their chemical compatibilities have been examined with three separate fluorite phases: 10Sc1YSZ, 10Sc1CeSZ, and 8YSZ. In total, there are 5 different compositions of dual-phase composites under heat treatment conditions.

Initial XRD results show that the chemical stability of the samples can be mainly affected by the initial Sr-content in the perovskite (Figure 5-6). The chemical stability of the dual-phase samples deteriorates over the Sr-content reduction. XRD patterns for LS1CrF73-8YSZ and LS1CrF73-10Sc1CeSZ show the formation of the LZO phase up to ~16 and ~19 Wt.% for the heat treatment under air, respectively (Figure 5-6). When $p(\text{O}_2)$ drops, the same samples have La_2O_3 as the secondary phase for the heat treatment under forming gas 1. No SZO phase has been observed for low Sr-content samples under all conditions.

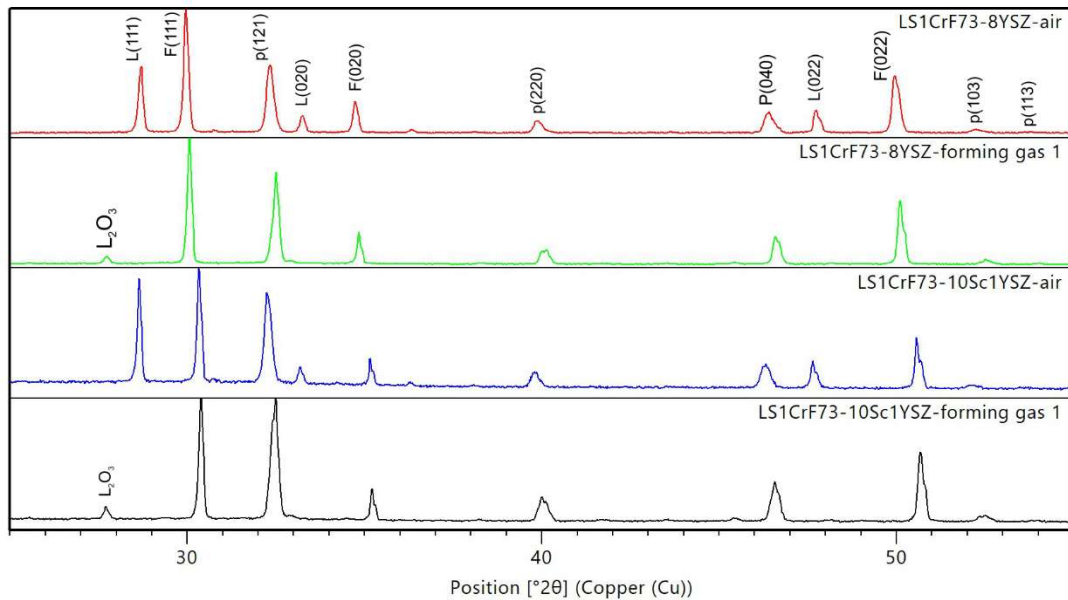


Figure 5-6. XRD patterns for $(\text{La}_{0.9}, \text{Sr}_{0.1})_{0.95}\text{Cr}_{0.7}\text{Fe}_{0.3}\text{O}_{3-\delta}$ -8YSZ and 10Sc1YSZ after heat treatment at 1400°C for 10 hours under air and forming gas 1 (wet-0.1% H_2 -Ar).

Samples with less Sr-content show no peaks for secondary phases after the heat treatment under argon. However, further investigations by SEM/EDS reveals that these samples have new morphologies which are mainly rich from Sr and O. Apparently, a Sr-segregation takes place for these samples (Figure 5-7). Based on the observed morphology in Figure 5-7, it is not expected that these regions are crystalline. It can explain why there is no peak for them in XRD patterns (Figure 5-6). Plus, the SrO phase (ICDD#00-

006-0520) has exact peak positions with 8YSZ (ICDD#01-077-2286). Accordingly, peaks for the 8YSZ phase with higher intensities can readily mask any possible SrO peaks in XRD patterns.

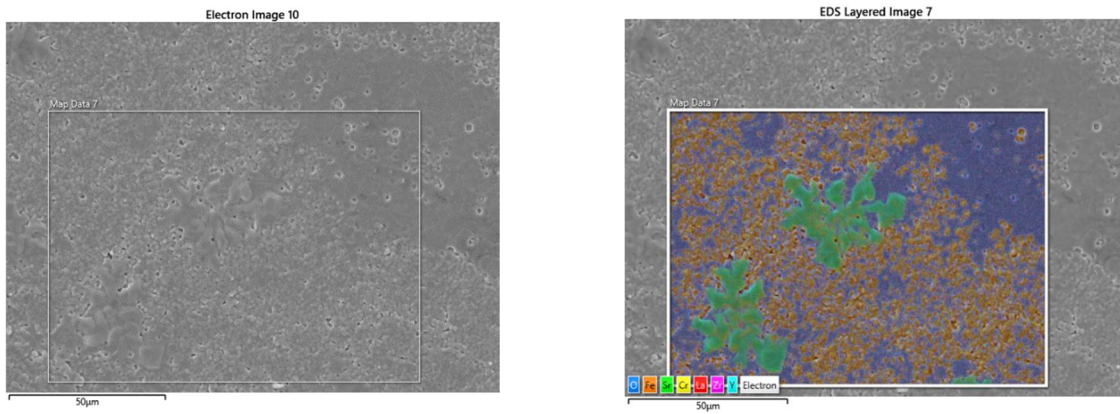


Figure 5-7. Microstructural analysis on $(\text{La}_{0.9}, \text{Sr}_{0.1})_{0.95}\text{Cr}_{0.7}\text{Fe}_{0.3}\text{O}_{3-\delta}$ -8YSZ after heating at 1400°C for 10 hours under forming gas 1 (wet-0.1% H_2 -Ar).

Further examinations on LS1CrF73-fluorite samples show that samples for all heat treatments have these Sr-rich regions, regardless of applied $p(\text{O}_2)$ (Figure 5-8). However, a decrease in $p(\text{O}_2)$ leads to changes in their morphology from irregular shapes under air (Figure 5-8-a and b) to bar-like and flower-like shapes under forming gas 1 (Figure 5-8-c and d).

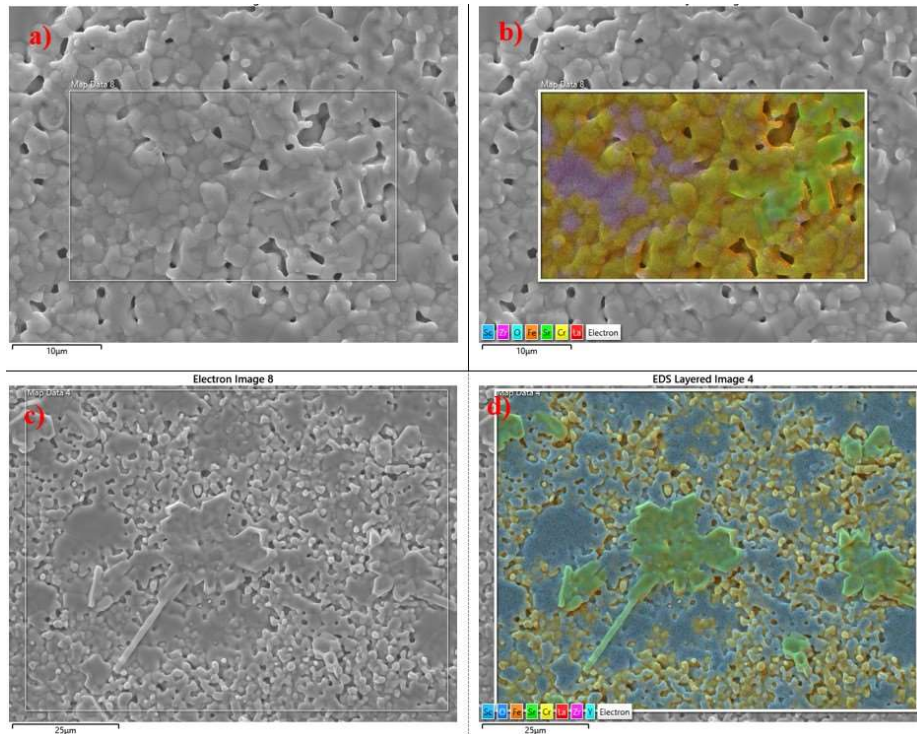


Figure 5-8. Microstructural analysis on $(\text{La}_{0.9}, \text{Sr}_{0.1})_{0.95}\text{Cr}_{0.7}\text{Fe}_{0.3}\text{O}_{3-\delta}$ -10Sc1CeSZ after heating at 1400°C for 10 hours under a and b) air c and d) forming gas 1 (wet-0.1% H_2 -Ar).

When Sr-content increases from 0.095 (LS1CrF73) to 0.19 (LS2CrF73), there is no sign of LZO and La_2O_3 phases or the Sr-segregation areas (Figure 5-9) neither in XRD nor in SEM results. However, SZO has been formed for two LS2CrF73-10Sc1YSZ and LS2CrF73-10Sc1CeSZ samples under reducing atmospheres, mainly due to an increase in Sr. No SZO phase has been detected for LS2CrF73-8YSZ for all heat treatment conditions (Figure 5-2). Under identical conditions, it seems that 8YSZ has better compatibility with LS2CrF73, compared with two other fluorite phases.

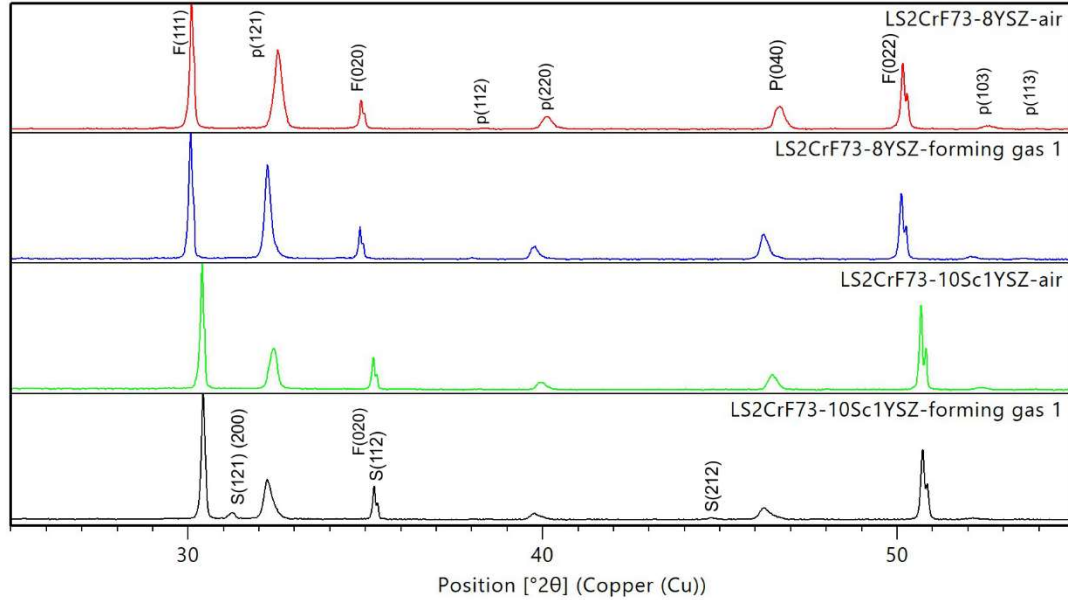


Figure 5-9. XRD patterns for $(\text{La}_{0.8}, \text{Sr}_{0.2})_{0.95}\text{Cr}_{0.7}\text{Fe}_{0.3}\text{O}_{3-\delta}$ -8YSZ and 10Sc1YSZ after heat treatment at 1400°C for 10 hours under air and forming gas 1 (wet-0.1% H_2 -Ar).

c. The Effect of The Cr: Fe Ratio

The effect of the Cr: Fe ratio in chemical stability of the perovskite phase has been well investigated by Sabarou and Gupta in a series of papers [16, 50, 54, 56]. The formations of spinel solid solution among Fe-Cr-O, a Fe-rich liquid phase, and phase separation in perovskite have been already reported for $(\text{La}, \text{Sr})(\text{Cr}, \text{Fe})\text{O}_{3-\delta}$. In dual-phase composites of LSCrF and fluorite phases, concerns about chemical stabilities are mainly about the formations of LZO and SZO phases. The phase stability in the perovskite structure leaves effects on the formations of LZO and SZO.

Figure 5-10 shows the microstructure of LS2CrF55-8YSZ after heat treating for 10 hours under argon. Regardless of 8YSZ regions (pink areas), two kinds of morphologies can be seen for the perovskite phase. Firstly, there are three colonies of the perovskite grains (white arrows). These are similar to grains observed in Figure 5-3. Secondly, there are river-like areas for the perovskite with irregular shapes for grains. It is believed that these river-like areas represent the formation of a liquid phase at high temperatures,

which can be later solidified into the perovskite phase due to the fast cooling procedure. It is also in good agreement with previous simulations performed on the fast cooling behavior of the liquid phase for LSCrF perovskites [16].

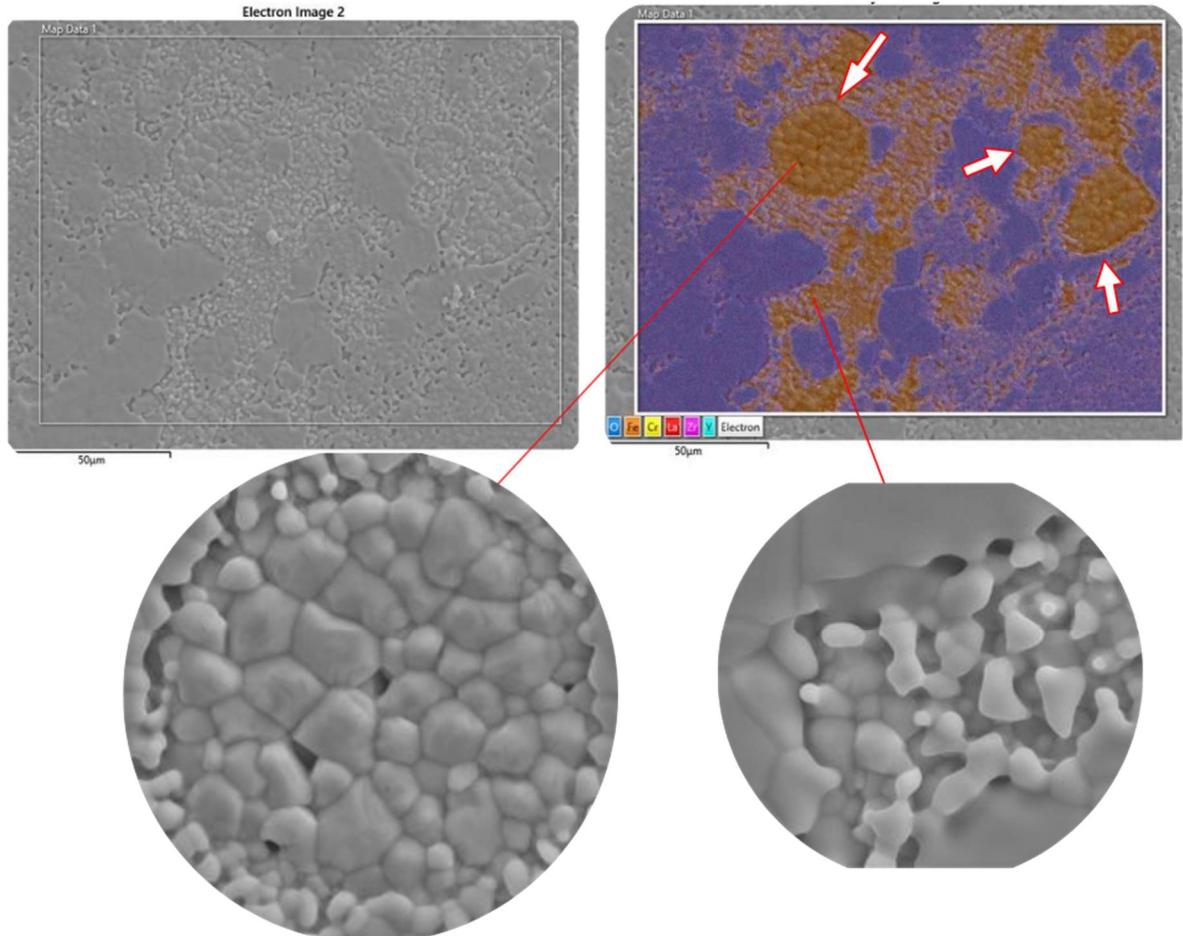


Figure 5-10. Microstructural analysis on $(\text{La}_{0.8}, \text{Sr}_{0.2})_{0.95}\text{Cr}_{0.5}\text{Fe}_{0.5}\text{O}_{3-\delta}\text{-8YSZ}$ after heating at 1400°C for 10 hours under argon.

Another effect of changes in the Cr: Fe ratio is related to its impact on the formation of SZO. Figure 5-11 shows the change in the formation of SZO with the Cr: Fe ratio according to XRD refinement results for 24 samples. It covers results for two $p(\text{O}_2)$ conditions for three fluorite phases. It is expected that some phases like the spinel and amorphous structures cannot be detected in the XRD patterns. To consider their contributions in this analysis, a tolerance bar for ± 1 %Wt. has been considered for all points.

As can be seen, the formation of SZO has been widely affected by changes in the Cr: Fe ratio. Contrary to the points for the forming gas 1, the results for argon show a trend as a decrease in the Cr: Fe ratio leads to the reduction in SZO. This trend has been observed for all three fluorite phases. However, when $p(\text{O}_2)$ drops under the forming gas 1, erratic behavior has been observed. It can be mainly due to the

formation of the liquid phase in the perovskite under very reducing atmospheres. For 8YSZ samples, a similar trend in Scandia stabilized zirconia has not been observed. Interestingly, no SZO has been formed for LS2CrF73, 55-8YSZ, for both atmospheres. It seems that the formation of SZO has been more limited with 8YSZ, especially for low Cr: Fe ratios. As no SZO phase has been detected for heat treatments under air, it can be concluded that the SZO formation can be limited by the use of lower Cr: Fe ratio and more oxidizing $p(O_2)$.

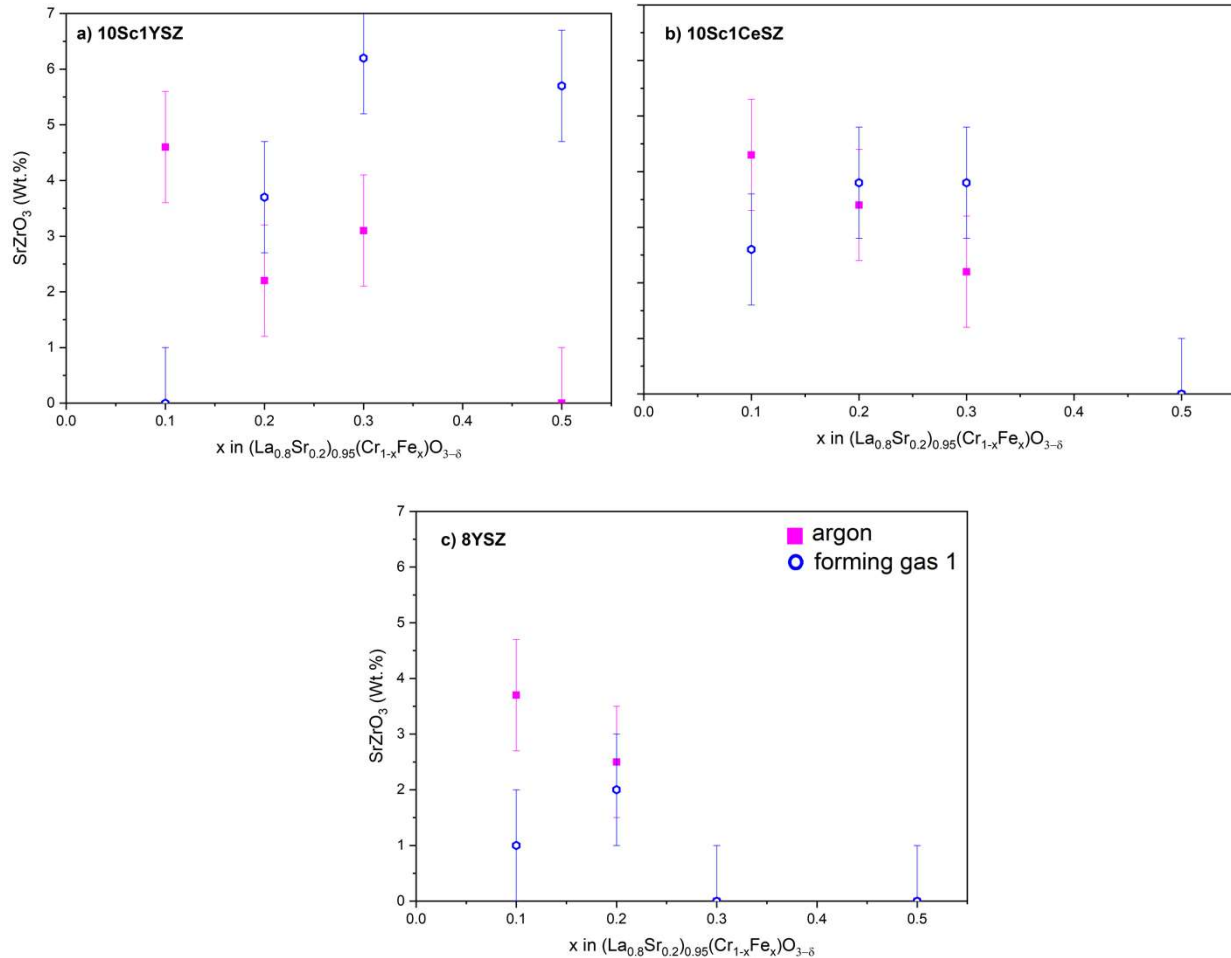


Figure 5-11. Changes in the phase content of SrZrO₃ with the Cr: Fe ratio for a)10Sc1YSZ, b)1Sc1CeSZ, and c) 8YSZ after heat treatments at 1400°C under argon and forming gas 1 (wet-0.1% H₂-Ar).

The spinel solid solution is another phase, which its formation is mainly affected by the Cr: Fe ratio. Microstructural analysis reveals that spinel grains can be found in almost all samples with different morphologies (Figure 5-12). Previous studies on single-phase perovskite of LSCrF show that an increase in Fe content increases the formation of the spinel phase [16]. The same trend has been observed here for dual-phase composites samples after SEM analysis. However, it is scarce to detect the spinel phase in XRD patterns. In this study, only one sample has small peaks of this phase after the stability test (LS2CrF73-

8YSZ). The disappearance of the spinel phase in XRD spectra can leave effects on the phase content of SZO in Figure 5-11.

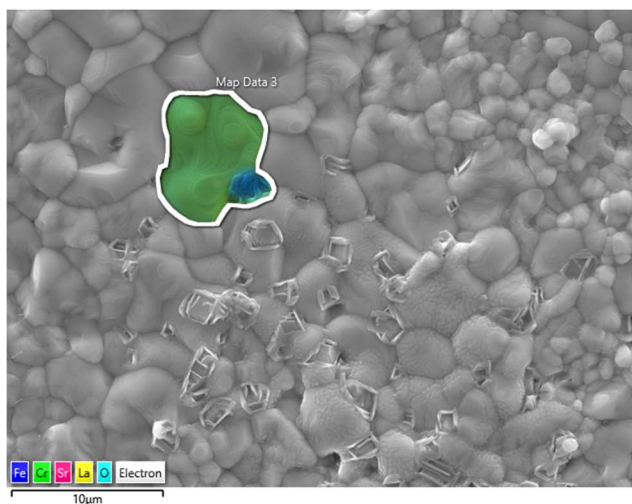


Figure 5-12. The formation of the spinel phase in $(\text{La}_{0.8}, \text{Sr}_{0.2})_{0.95}\text{Cr}_{0.5}\text{Fe}_{0.5}\text{O}_{3-\delta}-10\text{Sc}1\text{YSZ}$ after the heat treatment at 1400°C for 10 h under argon.

d. Perovskite Phase Separation

The crystal symmetries of the LSCrF perovskite under ambient conditions change from rhombohedral to orthorhombic when the Cr: Fe ratio or Sr-content decreases [92, 96]. In the previous chapter, it was shown the fluctuations in dopants can result in phase separation in the perovskite. The perovskite phase separation is a new reported phenomenon in $(\text{La},\text{Sr})(\text{Cr},\text{Fe})\text{O}_{3-\delta}$, in which the initial Cr-rich perovskite structure is separated into two Cr-rich and Fe-rich perovskite structures. It has been comprehensively investigated in the previous chapter. In the current study, after the heat treatments and stability test, similar phase separation has been observed for the perovskite phase (Figure 5-13).

In this study, results based on the Rietveld refinement reveal that the initial Cr-rich perovskite structures with rhombohedral symmetry are separated into two rhombohedral and orthorhombic phases (Figure 5-13). This figure covers two utterly different $p(\text{O}_2)$ conditions for the LS2CrF82-10Sc1SZ sample. All peaks for the perovskite phase have left shoulders across 2 theta angles from 20 to 120° , which represent the presence of two rhombohedral and orthorhombic phases in one sample. Peak splitting for the same Cr-rich samples has also been observed for heat treatments under air and argon. Table 5-3 shows the results for the phase separation analysis on the XRD patterns of these samples. Based on Table 5-3, the content of the second perovskite can be reached ~ 20 Wt.% under the stability test condition.

Table 5-3. Perovskite phase separation in dual-phase composites sample (perovskite#1 is Cr-rich, and perovskite #2 is Fe-rich)

Sample	Conditions	Perovskite Content (Wt.%)
LS2CrF82-10Sc1YSZ	1400°C-10h-air	Perovskite #1= 36.5 Perovskite #2 10.1
LS2CrF82-10Sc1CeSZ	1400°C-10h-air	Perovskite #1= 38.1 Perovskite #2= 5.0
LS2CrF91-10Sc1YSZ	1400°C-10h-Ar	Perovskite #1= 39.4 Perovskite #2= 4.4
LS2CrF91-8YSZ	1400°C-10h-Ar	Perovskite #1= 45.3 Perovskite #2= 5.8
LS2CrF82-8YSZ	1400°C-10h-Ar	Perovskite #1= 26.7 Perovskite #2= 8.5
LS2CrF91-10Sc1YSZ	850°C-10h-wet-4%H ₂ -Ar	Perovskite #1= 37.9 Perovskite #2= 6.9
LS2CrF82-10Sc1YSZ	850°C-10h-wet-4%H ₂ -Ar	Perovskite #1= 26.6 Perovskite #2= 20.4
LS2CrF82-10Sc1CeSZ	850°C-10h-wet-4%H ₂ -Ar	Perovskite #1= 23.6 Perovskite #2= 20.3
LS2CrF91-8YSZ	850°C-10h-wet-4%H ₂ -Ar	Perovskite #1= 44.5 Perovskite #2= 4.5
LS2CrF82-8YSZ	850°C-10h-wet-4%H ₂ -Ar	Perovskite #1= 33.5 Perovskite #2= 6.1

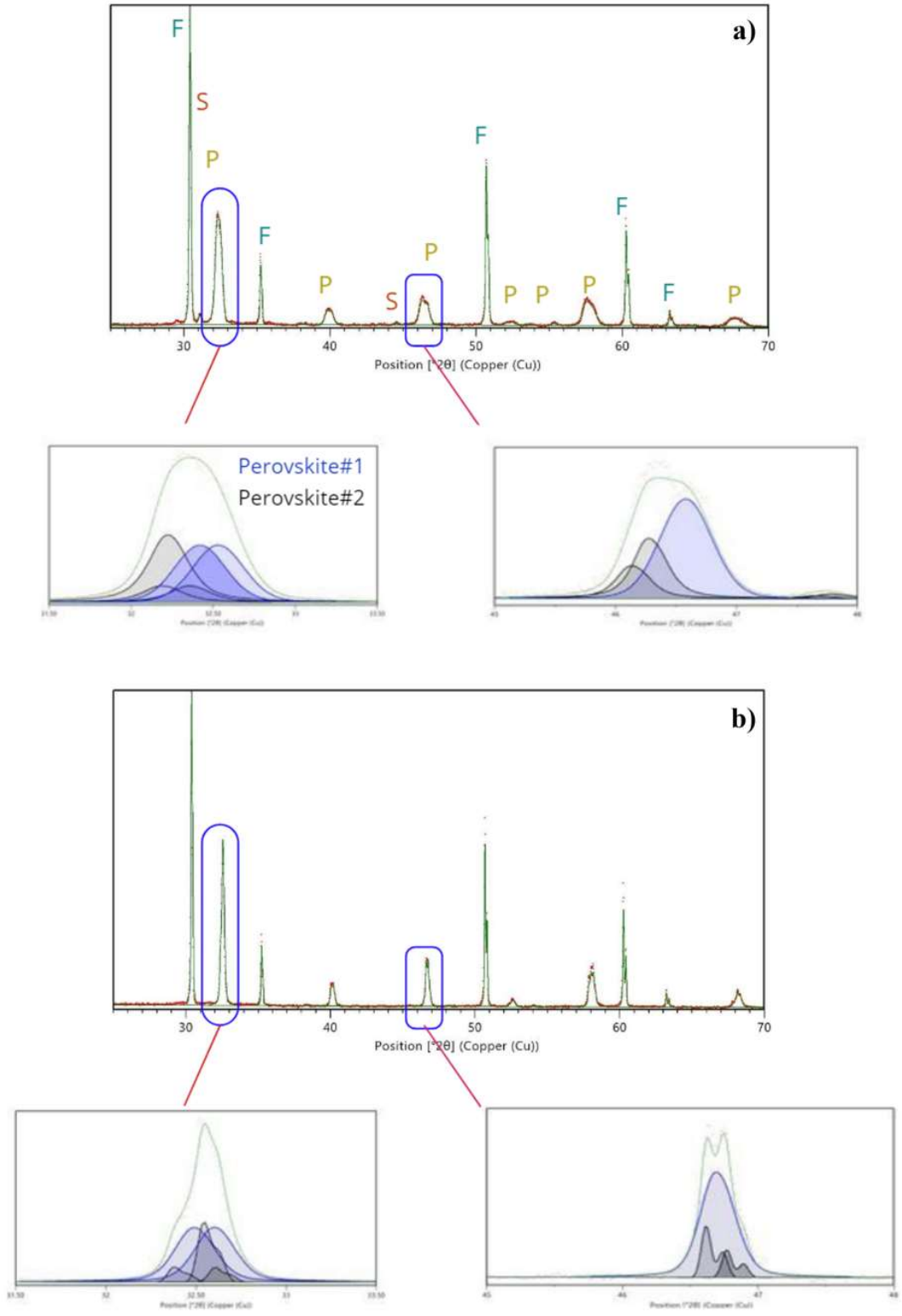
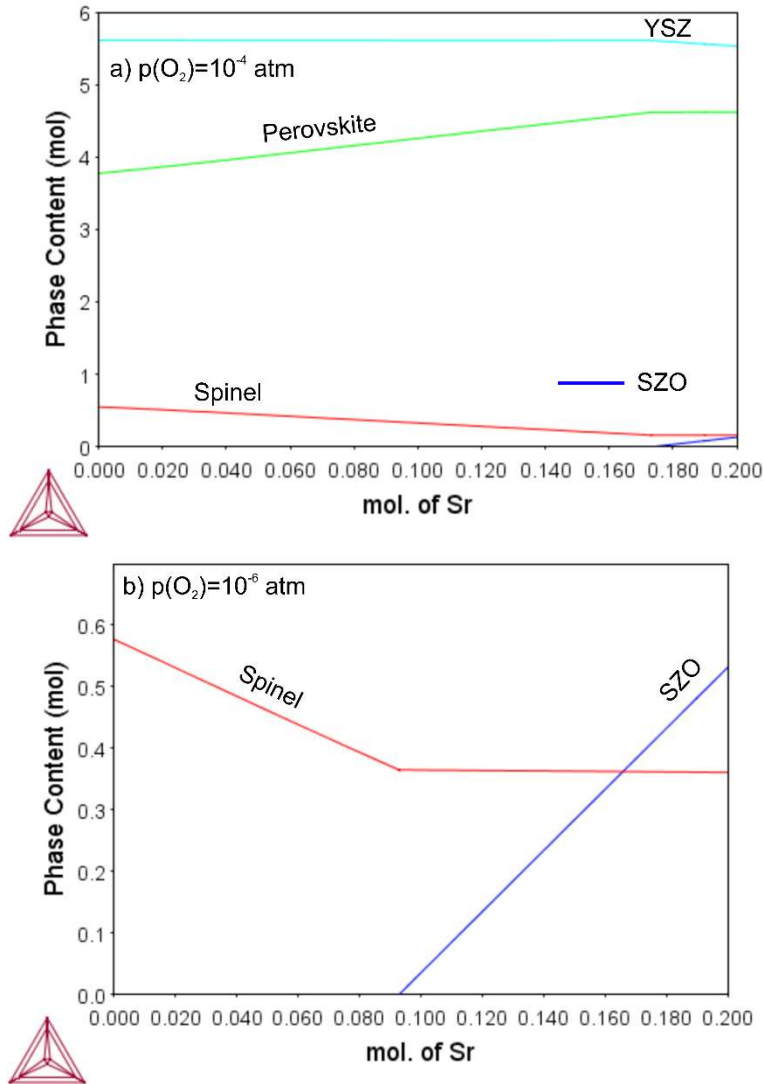


Figure 5-13. The occurrence of perovskite phase separation for LS₂CrF₈₂-10Sc₁YSZ after a) heating under wet-4% H₂-Ar at 850°C for 10 hours b) heat treatment under air at 1400°C for 10 hours. Blue peak: Cr-perovskite, Black peaks: Fe-rich perovskite.

e. Simulations by Computational Thermodynamic

Due to the importance of SZO as the dominant secondary phase, the first series of simulations has been conducted to unravel the correlations of the SZO formation with Sr content, $p(\text{O}_2)$, temperature, and the Cr: Fe ratio. Figure 5-14 shows the phase stability of LS2CrF73-8YSZ at three different $p(\text{O}_2)$ while Sr-content changes from 0 to 0.2 mol. Temperature is fixed at 1400°C.



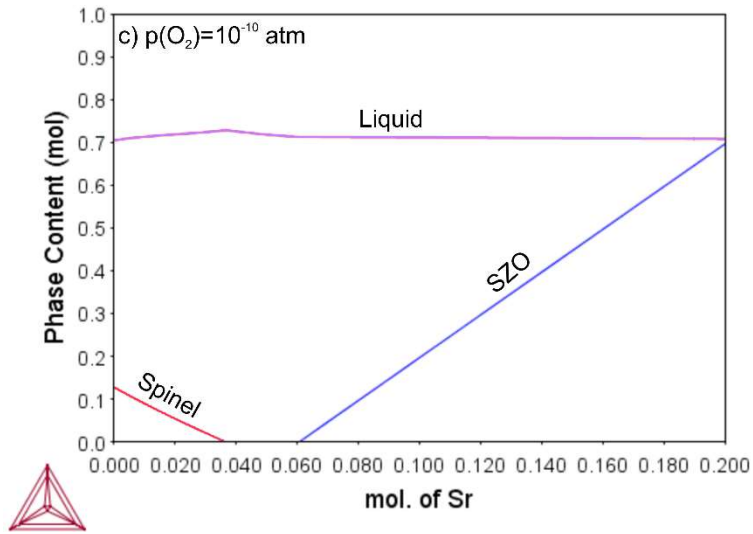


Figure 5-14. The correlation between SZO and spinel phases with changes in $p(\text{O}_2)$ at 1400°C in LS2CrF73-8YSZ .

The formation of the SZO is promoted with a decrease in $p(\text{O}_2)$. It means that it would be harder for the system not to have SZO even for few amounts of Sr when $p(\text{O}_2)$ is 10^{-18} atm. It can explain why no SZO phase has been detected for any samples of heat-treated in air. The correlation of the SZO and the spinel phases is also interesting. It seems that the formation of spinel counteracts the formation of SZO. At $p(\text{O}_2)=10^{-18}$ atm, the spinel phase has been disappeared owing to the formation of the liquid phase. Based on these results, there is an optimum for Sr-content at every $p(\text{O}_2)$.

Figure 5-15 a and b show the behavior of SZO formation with changes in temperature and the Cr:Fe ratio at different $p(\text{O}_2)$, respectively. The breakpoints in lines occur when either the liquid or spinel phases form. In general, the formation of SZO decreases if both temperature and $p(\text{O}_2)$ increase. In this case, it can reach its minimum range between 1200 to 1400°C . Also, the sensitivity to $p(\text{O}_2)$ increases with an increase in temperature. It can be due to the formation of the liquid phase in the perovskite at low $p(\text{O}_2)$ and high temperatures.

Due to counteracting behavior between the spinel and SZO phases, the SZO formation at 1400°C has been simulated with the Cr: Fe ratio in Figure 5-15. b under three different $p(\text{O}_2)$. The general trend is in good agreement with experimental findings for argon so that a decrease in the Cr: Fe ratio can reduce the formation of SZO. Interestingly, the results for $p(\text{O}_2)=10^{-4}$ atm is match with experimental results for the heat treatments under argon in Figure 5-11. However, there is a deviation between simulated and experimental results as $p(\text{O}_2)$ drops further. It can be due to limitations in XRD techniques in detecting low-content and low crystalline phases. Indeed, in the simulations, there are five different phases, including SZO, spinel, perovskite, fluorite, and liquid, whereas the XRD refinements are based on only three phases of perovskite, fluorite, and SZO in Figure 5-11. It is because there are no peaks for other remaining phases

in XRD patterns. It is believed that this limitation in XRD is the primary source of deviations between Figure 5-15 and Figure 5-11.

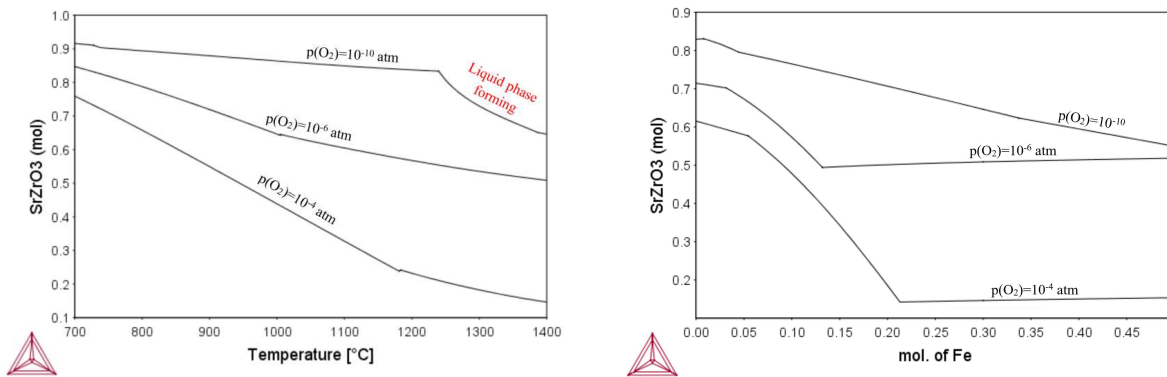


Figure 5-15. The formation of SZO with changes in a) temperature and b) the Cr: Fe ratio at 1400°C under different oxygen partial pressures ($p(O_2)$).

The formations of the liquid phase and spinel phases have also been modeled with $p(O_2)$ and changes in the Cr: Fe ratio at 1400°C (Figure 5-16). For more oxidizing $p(O_2)$ (10^{-4} and 10^{-6} atm), there is no liquid phase. As $p(O_2)$ drops further, the liquid phase forms, mainly at the expense of the spinel phase.

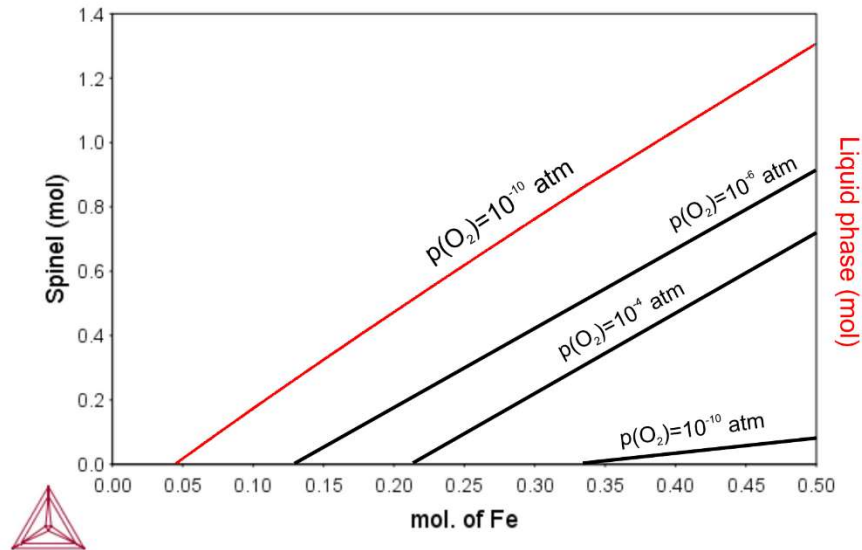


Figure 5-16. The formations of spinel and liquid phases with changes in the Cr: Fe ratio under different $p(O_2)$ conditions at 1400°C.

6. Discussion

According to the mentioned results, the chemical stability of the sample much depends on dopants contents on A- and B-sites. In the comparison between Figure 5-6 and Figure 5-9, reduction in Sr on A-site

of the LSCrF perovskite mainly changes the chemical stability behavior in the presence of the fluorite phases. For the lower content of Sr, it is believed that Sr leaves the perovskite structure at high temperature and oxidizing atmospheres and destabilize the whole perovskite structure. It leads to release in La_2O_3 , which later reacts with ZrO_2 and forms LZO. This can explain the formations of LZO in Figure 5-6. Indeed, the limited formation of LZO in the current study is surprising. It was initially expected that the LZO would be one of the dominant secondary phases for the samples. However, it can only be characterized for 3 out of 60 examined samples.

Furthermore, the analyzed LZO phase in this investigation has a fluorite structure with $(\text{La}_{0.5}\text{Zr}_{0.5})\text{O}_{1.75}$ composition, which is different from the widely reported $\text{La}_2\text{Zr}_2\text{O}_7$ phase in similar systems [126-128]. The later has a pyrochlore structure and is more stable against oxygen diffusion due to the more ordered cation structures. It is stable at room temperature, while the fluorite structure of LZO is a defect structure and forms at high temperatures. In the current research, it is believed that the formation of LZO has been suppressed due to employing a combination of doping, low $p(\text{O}_2)$, high-temperature heat treatment, and fast cooling. Pertinent contents of dopants, especially on A-site, can stop releasing La_2O_3 from the perovskite structure, while heat treatments at high temperatures and consequence fast cooling prevent the $\text{La}_2\text{Zr}_2\text{O}_7$ phase from developing. Low $p(\text{O}_2)$ also seems to be against the formation of the LZO phase as only (LS2CrF55-8YSZ) has the LZO phase $(\text{La}_{0.5}\text{Zr}_{0.5})\text{O}_{1.75}$ after the stability test under forming gas 2 (wet-4% H_2 -Ar).

With the same approach, the formation of SZO can be affected by a combination of low $p(\text{O}_2)$, high Sr content on A-site, and high Cr: Fe ratio. The effect of Cr: Fe ratio on the formation of SZO resembles the similar effect of the ratio on the SrO formation in single-perovskite of LSCrF as it has been covered in the previous chapter. Based on the results in Figure 5-11 and Figure 5-15, the role of the Cr: Fe ratio depends on applied $p(\text{O}_2)$. At very low $p(\text{O}_2)$ ($<10^{-8}$), low Cr: Fe ratio results in the formation of the liquid phase in the perovskite at elevated temperatures, mainly at the expense of the spinel phase (Figure 5-16). It is expected that reactivity between two perovskite and fluorite phases and diffusions of cations increases after the formation of the liquid. Erratic trends in SZO formations in Figure 5-11 for the forming gas 1 can be due to the formation of the liquid phase. However, if the spinel phase can be maintained and the formation of the liquid phase can be suppressed, the formation of SZO will be minimized due to the counteracting behavior between the spinel and SZO phases in Figure 5-14. The simulations in Figure 5-15 and experimental results in Figure 5-11 reveal this technique can be done by applying oxidizing atmospheres between 10^{-4} am to ambient air. These atmospheres help to stabilize the spinel phase at high temperatures ($>1200^\circ\text{C}$) without forming the liquid phase.

According to the results and examined parameters in this study, in dual-phase composites of LSCrF-stabilized zirconia, the critical parameters for the development of the LZO and SZO phases can be schematically plotted in Figure 5-17. As can be seen, some parameters, like Sr content and $p(O_2)$ have double-edged effects. It shows the importance of balancing parameters in designing dual-phase composites of perovskites and fluorites.

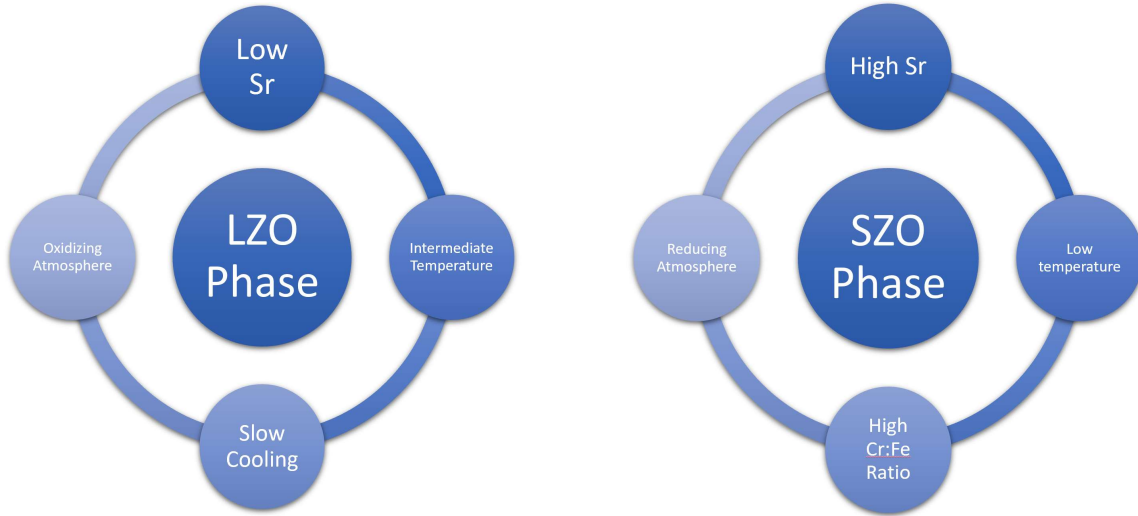


Figure 5-17. Involved parameters in the formations of a) $(La_{0.5}Zr_{0.5})O_{1.75}$ (LZO) and b) $SrZrO_3$ (SZO) phases in $(La,Sr)(Cr,Fe)O_{3-\delta}$ -8YSZ dual-phase composites.

It is also believed that fast cooling procedure on the SZO formation and the Cr: Fe ratio on the LZO formation would also be effective. These are the subjects for the next study.

7. Conclusion

The current research has examined the chemical stability of $(La,Sr)(Cr,Fe)O_{3-\delta}$ perovskites with YSZ, 10Sc1YSZ, and 10Sc1CeSZ under oxidizing and reducing atmospheres at high temperatures. The results show that the chemical stability of dual-phase samples mainly depends on accurate balancing between dopant content on A-site and B-site concerning applied conditions. Two secondary phases of $SrZrO_3$ (SZO) and spinel have been characterized as significant challenges to maintain chemical stability. Owing to the use of computational Thermodynamic, a wide range of conditions and compositions can be examined to unravel the correlations between dopants and these two secondary phases. The simulation results show that the SZO formation can be limited by counterbalancing with the spinel phase, and the spinel phase can be controlled by the Cr: Fe ratio and $p(O_2)$. Accordingly, the formations of secondary phases can be minimized with precise doping. In the current study, the best chemical stability has been reported for LS2CrF73-8YSZ. The use of computational Thermodynamic helps to examine different

scenarios and narrow down on appropriate conditions and compositions. Findings in the current work can be utilized for materials development in dual-phase ceramic membranes and solid oxide fuel cells.

Chapter 6 : Conclusion and Future Work

1. The Contribution of This Dissertation

In this project, the focus has been on the chemical stability of LSCrF perovskites at different temperatures and oxygen partial pressures. The findings for the perovskite have been later extended to dual-phase composites of the perovskite and fluorite phases. The summary of contributions of this dissertation can be presented as below:

I. The critical role of the Cr: Fe ratio in the chemical stability of LSCrF perovskite has been well investigated with changes in temperatures (T) and oxygen partial pressures ($p(\text{O}_2)$). Firstly, all secondary phases have been characterized as T and $p(\text{O}_2)$ change. They include corundum, spinel, SrO, and La_2O_3 phases in the perovskite. Secondly, the investigation has focused on involved mechanisms and studied correlations among parameters to minimize formations of the secondary phases. For LSCrF perovskites, it is the first time that the origin of secondary phases is documented, and there are proposed parameters to control their formations.

II. The examined results for the Cr: Fe ratio shed more light on the role of the Cr: Fe ratio, which contradicts previous findings for this system. It rejects the general believes that Cr-rich LSCrF perovskites always present the best chemical stability. In the contrary, the results in this study propose that the Cr: Fe ratio should be carefully tuned based on applied T and $p(\text{O}_2)$ and target working conditions. It is proved that a 7:3 ratio for the Cr: Fe can have better phase stabilities under routine fabrication and processing conditions of Oxygen Transport Membranes (OTM).

III. The formation of the liquid phase has been reported and studied in this project for the first time. The dissertation reveals an increase in a liquid phase formation with an increase in T and a decrease in the Cr: Fe ratio or $p(\text{O}_2)$. Owing to the use of computational Thermodynamic, the behavior of the liquid phase under different fabrication and operating conditions have been documented. These findings can help to control the formation of the liquid phase and take advantage of it to improve overall densifications.

IV. Perovskite phase separation is another novel phenomenon in LSCrF perovskites, which has been reported in this dissertation for the first time. Owing to a combination approach from experiments and computational Thermodynamic, the phase

separation has been investigated so that its behavior could be tracked with changes in the Cr: Fe ratio, T, and $p(\text{O}_2)$. The correlations among contents of dopants and the phase separation have been developed to predict and monitor the phenomenon over T and $p(\text{O}_2)$ ranges.

V. The chemical stability of LSCrF with 8YSZ, 10Sc1YSZ, and 1Sc1CeSZ phases have been thoroughly investigated in this dissertation for the bulk samples. The focus of the research is on correlations of the Cr: Fe ratio and applied T and $p(\text{O}_2)$ in formations of secondary phases and degradations in crystal symmetries of the perovskite phase. The main secondary phases have been characterized, and their counteracting behavior has been documented.

VI. Sr-segregation is another phenomenon that has been reported in this dissertation for the first time. It shows that the bulk chemical stability of dual-phase LSCrF-fluorite phases mainly depends on the precise doping of Sr on A-site in the perovskite structures. Indeed, too low Sr-content destabilizes the perovskite structure and leads to the release of La_2O_3 and Sr segregation at high temperatures, while too much Sr content promotes the formation of SrZrO_3 (SZO) under reducing atmospheres.

VII. Owing to the use of computational Thermodynamic approach, different compositions and conditions could quickly be examined to find correlations among parameters. This trend results in practical procedures to minimize SZO and LZO ($\text{La}_2\text{Zr}_2\text{O}_7/\text{La}_{0.5}\text{Zr}_{0.5}\text{O}_{1.75}$) formations in dual-phase ceramic membranes of LSCrF and cubic YSZ. Based on these results, YSZ has been preferred over Scandia stabilized Zirconia phases because of presenting better chemical compatibility with the LSCrF phase. The combination of LSCrF-YSZ can survive one of the harshest possible conditions of OTM, while two other fluorites have been decomposed.

VIII. Involved parameters in the formations of SZO and LZO have been investigated, and they are procedures on how to balance these parameters with the Cr: Fe ratio in the perovskite phase and applied T and $p(\text{O}_2)$.

IX. The dissertation reveals the strength of the computational Thermodynamic as a novel approach in materials design and development. This approach helps to sweep numerous compositions and scenarios for materials and ultimately narrow down on several

final answers. It also acts as a powerful materials characterization assistant when routine analytical techniques face their limitations.

In conclusion, it is believed that LSCrF-YSZ has excellent potential for OTM and SOFC applications. It can survive very high temperatures and reducing atmospheres where a similar system cannot tolerate. Hence, the precise design of this material can push current limits for OTM materials and enhance its performance.

2. The future works

The current dissertation provides a new perspective in materials development for the oxygen transport membrane. It presents the capability of computational Thermodynamic to shape experiments, interpret results, and define the right directions for further investigations. Here are the proposed items for further investigations in this field.

- I. There is a shortage of thermoelectric data on for LSCrF perovskites for a wide range of $p(\text{O}_2)$ and different temperatures. It requires electrical conductivity and Seebeck coefficient measurements concerning changes in the Cr: Fe ratio. Due to the increase of Fe in B-site, the decrease in the Cr: Fe ratio promotes the role of oxygen nonstoichiometry in defect chemistry for the perovskite. It can shape its thermal and chemical expansions behaviors and its mixed ionic-electronic conductivity characteristics. These results should be completed with dilatometry and thermogravimetric results to provide a broad perspective of involved defect chemistry for the system. The provided results in this dissertation clearly define frameworks for ranges of temperature and $p(\text{O}_2)$, where the perovskite remains stable. This helps to improve the quality of defect models for this system.
- II. The ratio between perovskite and fluorite phases still needs to be tuned precisely. In dual-phase ceramic membranes, the fragile phase is the perovskite. Hence, deteriorations in the bulk chemical stability of the dual-phase samples can be minimized by a decrease in the content of the perovskite phase. However, it requires mass transport data like oxygen permeation and electrical conductivity to confirm the best ratio between fluorite and perovskite phases.

- III. Other techniques like coating, hollow fiber, and infiltration can also be examined to minimized degradation in the perovskite phase in dual-phase membranes. However, they need separate investigations with the focus on mechanical properties.
- IV. Databases for both perovskite and fluorite phase need to be re-assessed, especially for dual-phase composites of LSCrF and fluorite phases. Currently, it cannot simulate the existence of the perovskite phase for very reducing atmospheres (lower than 10^{-18} atm). Also, the descriptions of perovskite, LZO, tetragonal, and monoclinic YSZ phases should be re-assessed.

Reference:

- [1] Department of Energy, National Energy Technology Laboratory, Report, 2013.
- [2] E. Yantovski, J. Gorski, B. Smyth, J. ten Elshof, *Energy*, 29 (2004) 2077-2088.
- [3] S. Gupta, M.K. Mahapatra, P. Singh, *Materials Science and Engineering: R: Reports*, 90 (2015) 1-36.
- [4] E.T. Robinson, in: ACS Division of Fuel Chemistry, Preprints, 2003, pp. 347-349.
- [5] C.Y. Tsai, A.G. Dixon, W.R. Moser, Y.H. Ma, *Aiche Journal*, 43 (1997) 2741-2750.
- [6] S.M. Hashim, A.R. Mohamed, S. Bhatia, *Advances in Colloid and Interface Science*, 160 (2010) 88-100.
- [7] T. Ishihara, *Perovskite Oxide for Solid Oxide Fuel Cells*, Springer Science & Business Media, 2009.
- [8] J. Sunarso, S.S. Hashim, N. Zhu, W. Zhou, *Progress in Energy and Combustion Science*, 61 (2017) 57-77.
- [9] V.M. Goldschmidt, *Naturwissenschaften*, 14 (1926) 477-485.
- [10] C.J. Bartel, C. Sutton, B.R. Goldsmith, R. Ouyang, C.B. Musgrave, L.M. Ghiringhelli, M. Scheffler, *Science Advances*, 5 (2019) eaav0693.
- [11] S. Gupta, Ph.D. Thesis, University of Connecticut, Storrs, 2015.
- [12] M. Mori, T. Yamamoto, H. Itoh, T. Watanabe, *Journal of Materials Science*, 32 (1997) 2423-2431.
- [13] S. Darvish, M. Asadikiya, B. Hu, P. Singh, Y. Zhong, *International Journal of Hydrogen Energy*, 41 (2016) 10239-10248.
- [14] C.C. Wang, S. He, K. Chen, M.R. Rowles, S. Darvish, Y. Zhong, S.P. Jiang, *Journal of The Electrochemical Society*, 164 (2017) F514-F524.
- [15] C.C. Wang, S. Darvish, K. Chen, B. Hou, Q. Zhang, Z. Tan, Y. Zhong, S.P. Jiang, *Electrochimica Acta*, 312 (2019) 202-212.
- [16] H. Sabarou, S. Darvish, S. Gupta, P. Singh, Y. Zhong, *Solid State Ionics*, 310 (2017) 1-9.
- [17] V.V. Kharton, A.V. Kovalevsky, A.P. Viskup, F.M. Figueiredo, A.A. Yaremchenko, E.N. Naumovich, F.M.B. Marques, *Journal of the Electrochemical Society*, 147 (2000) 2814-2821.
- [18] S. Darvish, Y. Zhong, S. Gopalan, *ECS Transactions*, 78 (2017) 1021-1025.
- [19] M.C. E Povoden-Karadeniz, T Ivas, *Journal of Materials Research*, 27 (2012) 1915-1926.
- [20] M. Hillert, *Journal of Alloys and Compounds*, 320 (2001) 161-176.

- [21] E. Povoden, M. Chen, A.N. Grundy, T. Ivas, L.J. Gauckler, 30 (2009) 12-27.
- [22] J.R. Taylor, A.T. Dinsdale, Zeitschrift Fur Metallkunde, 84 (1993) 335-345.
- [23] E. Povoden, A. Nicholas Grundy, L.J. Gauckler, Journal of phase equilibria and diffusion, 27 (2006) 353-362.
- [24] A.N. Grundy, Ph.D. Thesis, Swiss Institute of Technology Zurich, Zurich, 2003.
- [25] M. Chen, Ph.D. Thesis, Swiss Federal Institute of Technology, Zurich, 2005.
- [26] M. Chen, Thermodynamic Modeling of the La-Sr-Mn-O-Y-Zr System, 2006.
- [27] M. Asadikiya, Y. Zhong, Journal of Materials Science, 53 (2018) 1699-1709.
- [28] M. Asadikiya, P. Foroughi, Y. Zhong, Calphad, 61 (2018) 264-274.
- [29] Y. Zhong, M. Chen, Private Communications, 2013.
- [30] Scientific Group Thermodata Europe, SGTE Substances Database-SSUB5. Thermo-Calc.
- [31] R. Del Toro, P. Hernández, Y. Díaz, J.L. Brito, Materials Letters, 107 (2013) 231-234.
- [32] M. Asgari, A. Ataie, H. Sabarou, Journal of Materials Engineering and Performance, 23 (2013) 826-832.
- [33] H. Sabarou, A. Ataie, Ultrafine Grained and Nano-Structured Materials Iv, 829 (2014) 762-766.
- [34] M. Jafari, M. Salavati-Niasari, K. Saberyan, H. Sabarou, Synthesis and Reactivity in Inorganic Metal-Organic and Nano-Metal Chemistry, 45 (2015) 58-67.
- [35] H. Sabarou, A. Ataie, International Journal of Modern Physics: Conference Series, 05 (2012) 134-141.
- [36] A. Ataie, H. Sabarou, Journal of Nanostructures, 1 (2011) 7-13.
- [37] S. Lee, T.W. Knight, E. Roberts, Nuclear Engineering and Design, 292 (2015) 39-45.
- [38] J. Sfeir, P.A. Buffat, P. Ockli, N. Xanthopoulos, R. Vasquez, H.J. Mathieu, J. Van Herle, K.R. Thampi, Journal of Catalysis, 202 (2001) 229-244.
- [39] J. Fergus, Solid State Ionics, 171 (2004) 1-15.
- [40] N. Sakai, H. Yokokawa, T. Horita, K. Yamaji, International Journal of Applied Ceramic Technology, 1 (2004) 23-30.
- [41] P. Singh, T.R. Vasilow, V.L. Richards, in, Google Patents, 1996.
- [42] Y. Zhang, R.-h. Yuan, J.-f. Gao, C.-s. Chen, Separation and Purification Technology, 166 (2016) 142-147.

- [43] M.F. Lü, E.V. Tsipis, J.C. Waerenborgh, a.a. Yaremchenko, V.a. Kolotygin, S. Bredikhin, V.V. Kharton, *Journal of Power Sources*, 206 (2012) 59-69.
- [44] S. Darvish, H. Sabarou, S.K. Saxena, Y. Zhong, *Journal of The Electrochemical Society*, 162 (2015) E134-E140.
- [45] W. He, H. Huang, M. Chen, J.F. Gao, C.S. Chen, *Solid State Ionics*, 260 (2014) 86-89.
- [46] W. Fang, Y. Zhang, J. Gao, C. Chen, *Ceramics International*, 40 (2014) 799-803.
- [47] M. Oishi, K. Yashiro, K. Sato, J. Mizusaki, T. Kawada, *Journal of Solid State Chemistry*, 181 (2008) 3177-3184.
- [48] K. Salnikow, A. Zhitkovich, *Chemical research in toxicology*, 21 (2007) 28-44.
- [49] J. Peña-Martínez, D. Marrero-López, D. Pérez-Coll, J.C. Ruiz-Morales, P. Núñez, *Electrochimica Acta*, 52 (2007) 2950-2958.
- [50] H. Sabarou, Y. Zhong, Investigation on the Phase Stability of Perovskite in La-Sr-Cr-Fe-O System, in: *Advances in Solid Oxide Fuel Cells and Electronic Ceramics II*, John Wiley & Sons, Inc., 2017, pp. 127-135.
- [51] Y.Q. Zhang, J.H. Li, Y.F. Sun, B. Hua, J.L. Luo, *ACS Appl Mater Interfaces*, 8 (2016) 6457-6463.
- [52] S. Tao, J.T. Irvine, *Chemistry of materials*, 16 (2004) 4116-4121.
- [53] S. Gupta, J.J. Adams, J.R. Wilson, E.G. Eddings, M.K. Mahapatra, P. Singh, *Applied Energy*, 165 (2016) 72-80.
- [54] S. Gupta, H. Sabarou, Y. Zhong, P. Singh, *International Journal of Hydrogen Energy*, 42 (2017) 6262-6271.
- [55] S. Gupta, P. Singh, *ECS Transactions*, 66 (2015) 117-123.
- [56] S. Gupta, H. Sabarou, Y. Zhong, P. Singh, *International Journal of Hydrogen Energy*, 42 (2017) 25351-25358.
- [57] S. Bajaj, G.S. Pomrehn, J.W. Doak, W. Gierlotka, H.-j. Wu, S.-W. Chen, C. Wolverton, W.A. Goddard, G.J. Snyder, *Acta Materialia*, 92 (2015) 72-80.
- [58] A. Bertei, M. Carpanese, D. Clematis, A. Barbucci, M. Bazant, C. Nicoletta, *Solid State Ionics*, 303 (2017) 181-190.
- [59] M. Yang, Y. Zhong, Z.-K. Liu, *Solid State Ionics*, 178 (2007) 1027-1032.
- [60] S.M. Aghaei, I. Torres, I. Calizo, *Computational Materials Science*, 138 (2017) 204-212.
- [61] A.S. Rad, S.M. Aghaei, E. Aali, M. Peyravi, *Diamond and Related Materials*, (2017).

- [62] M. Asadikiya, H. Sabarou, M. Chen, Y. Zhong, *Rsc Advances*, 6 (2016) 17438-17445.
- [63] E. Povoden, A. Nicholas Grundy, L.J. Gauckler, *Journal of Phase Equilibria and Diffusion*, 27 (2006) 353-362.
- [64] S. Darvish, S. Gopalan, Y. Zhong, *Journal of Power Sources*, 336 (2016) 351-359.
- [65] M. Mori, Y. Hiei, N.M. Sammes, *Solid State Ionics*, 123 (1999) 103-111.
- [66] J.B. Webb, M. Sayer, A. Mansingh, *Canadian Journal of Physics*, 55 (1977) 1725-1731.
- [67] N. Sammes, R. Ratnaraj, *Journal of materials science*, 30 (1995) 4523-4526.
- [68] N.N. Gurusinghe, J. de la Figuera, J.F. Marco, M.F. Thomas, F.J. Berry, C. Greaves, *Materials Research Bulletin*, 48 (2013) 3537-3544.
- [69] X. Chen, T. Grande, *Chemistry of Materials*, 25 (2013) 3296-3306.
- [70] E. Scheil, *Zeitschrift für Metallkunde*, 34 (1942) 70-72.
- [71] M. N.Rahaman, *Sintering of Ceramics*, CRC Press, 2007.
- [72] R.M. German, P. Suri, S.J. Park, *Journal of Materials Science*, 44 (2009) 1-39.
- [73] Priority List of Hazardous Substances | ATSDR, <https://www.atsdr.cdc.gov/spl/>, (2017 (accessed 05/31/2017)).
- [74] J.A. Jacobs, S.M. Testa, *Overview of chromium (VI) in the environment: background and history*, CRC Press: Boca Raton, FL, 2005.
- [75] A.A. Yaremchenko, V.V. Kharton, V.a. Kolotygin, M.V. Patrakeevev, E.V. Tsipis, J.C. Waerenborgh, *Journal of Power Sources*, 249 (2014) 483-496.
- [76] N. Sakai, H. Yokokawa, T. Horita, K. Yamaji, *International Journal of Applied Ceramic Technology*, 1 (2004) 23-30.
- [77] J.E. tenElshof, H.J.M. Bouwmeester, H. Verweij, *Proceedings of the First International Symposium on Ceramic Membranes*, 95 (1997) 37-47.
- [78] S.S. Liou, W.L. Worrell, *Applied Physics a-Materials Science & Processing*, 49 (1989) 25-31.
- [79] H. Sabarou, V. Drozd, O. Awadallah, A. Durygin, S. Darvish, D. Huang, Y. Zhong, *Journal of Alloys and Compounds*, 784 (2019) 592-602.
- [80] H. Sabarou, D.H. Huang, Y. Zhong, *Ceramics International*, 43 (2017) 12249-12257.
- [81] Y. Zhong, H. Sabarou, X. Yan, M. Yang, M.C. Gao, X. Liu, R.D. Sisson, *Materials & Design*, 182 (2019) 108060.
- [82] A. Zuev, L. Singheiser, K. Hilpert, *Solid State Ionics*, 147 (2002) 1-11.

- [83] J. Vieten, B. Bulfin, P. Huck, M. Horton, D. Guban, L.Y. Zhu, Y.J. Lu, K.A. Persson, M. Roeb, C. Sattler, *Energy & Environmental Science*, 12 (2019) 1369-1384.
- [84] M. Oishi, K. Yashiro, J.O. Hong, Y. Nigara, T. Kawada, J. Mizusaki, *Solid State Ionics*, 178 (2007) 307-312.
- [85] M. Oishi, K. Yashiro, K. Sato, J. Mizusaki, T. Kawada, *Journal of Solid State Chemistry*, 181 (2008) 3177-3184.
- [86] W. Fang, Y. Zhang, J. Gao, C. Chen, *Ceramics International*, 40 (2014) 799-803.
- [87] T. Liu, Y. Wang, R. Yuan, J. Gao, C. Chen, H.J.M. Bouwmeester, (2013).
- [88] V.V. Kharton, J.C. Waerenborgh, A.P. Viskup, S.O. Yakovlev, M.V. Patrakeev, P. Ski, I.P. Marozau, A.A. Yaremchenko, A.L. Shaula, V.V. Samakhval, *Journal of Solid State Chemistry*, 179 (2006) 1273-1284.
- [89] R.H. Yuan, W. He, Y. Zhang, J.-F. Gao, C.-s. Chen, *Journal of Membrane Science*, 499 (2016) 335-342.
- [90] J.M. Haag, B.D. Madsen, S.A. Barnett, K.R. Poeppelmeier, (2008).
- [91] H. Zhang, J.X. Yi, X. Jiang, *Acs Applied Materials & Interfaces*, 9 (2017) 17219-17226.
- [92] H. Hayashi, M. Watanabe, M. Ohuchida, H. Inaba, Y. Hiei, T. Yamamoto, M. Mori, *Solid State Ionics*, 144 (2001) 301-313.
- [93] H. Hayashi, M. Watanabe, H. Inaba, *Thermochimica Acta*, 359 (2000) 77-85.
- [94] H.E. Hofer, W.F. Kock, *Journal of the Electrochemical Society*, 140 (1993) 2889-2894.
- [95] A. Fossdal, M. Menon, I. Waernhus, K. Wiik, M.A. Einarsrud, T. Grande, *Journal of the American Ceramic Society*, 87 (2004) 1952-1958.
- [96] T. Wei, X. Liu, C. Yuan, Q. Gao, X. Xin, S. Wang, *Journal of Power Sources*, 250 (2014) 152-159.
- [97] E. Povoden-Karadeniz, A.N. Grundy, M. Chen, T. Ivas, L.J. Gauckler, *Journal of Phase Equilibria and Diffusion*, 30 (2009) 351-366.
- [98] I. Yasuda, M. Hishinuma, *Solid State Ionics*, 80 (1995) 171-171.
- [99] A.K. Huber, M. Falk, M. Rohnke, B. Luerssen, L. Gregoratti, M. Amati, J. Janek, *Physical Chemistry Chemical Physics*, 14 (2012) 751-758.
- [100] L. Zhao, J. Drennan, C. Kong, S. Amarasinghe, S.P. Jiang, *Journal of Materials Chemistry A*, 2 (2014) 11114-11123.

- [101] J.C. De Vero, H. Yokokawa, K. Develos-Bagarinao, S.-S. Liu, H. Kishimoto, T. Ishiyama, K. Yamaji, T. Horita, *MRS Communications*, 9 (2019) 236-244.
- [102] J. Topfer, S. Aggarwal, R. Dieckmann, *Solid State Ionics*, 81 (1995) 251-266.
- [103] J. J. Liu, T. Liu, W. D. Wang, J. F. Gao, C. S. Chen, *Journal of Membrane Science*, 389 (2012) 435-440.
- [104] C.D. Li, J.J. Chew, A. Mahmoud, S.M. Liu, J. Sunarso, *Journal of Membrane Science*, 567 (2018) 228-260.
- [105] S.P. Jiang, *Journal of Materials Science*, 43 (2008) 6799-6833.
- [106] S.K. Mazumder, K. Acharya, C.L. Haynes, R. Williams, M.R. von Spakovsky, D.J. Nelson, D.E. Rancruel, J. Hartvigsen, R.S. Gemmen, *Ieee Transactions on Power Electronics*, 19 (2004) 1263-1278.
- [107] Z. Shen, S.J. Skinner, J.A. Kilner, *Physical Chemistry Chemical Physics*, 21 (2019) 13194-13206.
- [108] Z. Shen, J.A. Kilner, S.J. Skinner, *The Journal of Physical Chemistry C*, 122 (2018) 27135-27147.
- [109] Y.I. Kwon, J.H. Park, S.M. Kang, G.D. Nam, J.W. Lee, J.H. Kim, D. Kim, S.M. Jeong, J.H. Yu, J.H. Joo, *Energy & Environmental Science*, 12 (2019) 1358-1368.
- [110] T.J. Mazanec, T.L. Cable, J.G. Frye, *Solid State Ionics*, 53 (1992) 111-118.
- [111] J. Kim, Y.S. Lin, *Aiche Journal*, 46 (2000) 1521-1529.
- [112] C.S. Chen, H. Kruidhof, H.J.M. Bouwmeester, H. Verweij, A.J. Burggraaf, *Solid State Ionics*, 86-8 (1996) 569-572.
- [113] C.S. Chen, A.J. Burggraaf, *Journal of Applied Electrochemistry*, 29 (1999) 355-360.
- [114] T. Liu, W. Zhao, Y. Wang, *ACS Applied Nano Materials*, 1 (2018) 3774-3778.
- [115] J. Sunarso, S. Baumann, J.M. Serra, W.a. Meulenber, S. Liu, Y.S. Lin, J.C. Diniz da Costa, *Journal of Membrane Science*, 320 (2008) 13-41.
- [116] T. Liu, W. He, H. Huang, S. Wang, H.J.M. Bouwmeester, C. Chen, *Industrial & Engineering Chemistry Research*, 54 (2014) 6131-6136.
- [117] P. Zhu, I. Falls, *Ceramic Membranes for Permeation*, 2008.
- [118] B. Wang, M. C. Zhan, D. C. Zhu, W. Liu, C. S. Chen, *Journal of Solid State Electrochemistry*, 10 (2006) 625-628.
- [119] W. Li, J.J. Liu, C.S. Chen, *Journal of Membrane Science*, 340 (2009) 266-271.

- [120] Y. Cheng, T. Oh, M. Rahmanipour, R. Wilson, R.J. Gorte, J.M. Vohs, in: ECS Transactions, 2017, pp. 729-740.
- [121] W. He, J. J. Liu, C.-s. Chen, M. Ni, Journal of Membrane Science, 491 (2015) 90-98.
- [122] Y. Zhang, R. H. Yuan, Z. Y. He, J. F. Gao, C. S. Chen, Solid State Ionics, 288 (2016) 342-346.
- [123] X. Liu, H. Wu, Z. He, J. Gao, X. Meng, T. Luo, C. Chen, Z. Zhan, International Journal of Hydrogen Energy, 42 (2017) 18410-18416.
- [124] S.G.F.B.S. Hans Lukas, Computational Thermodynamics The Calphad Method, 2007.
- [125] E. Povoden-Karadeniz, M. Chen, T. Ivas, a.N. Grundy, L.J. Gauckler, Journal of Materials Research, 27 (2012) 1915-1926.
- [126] A.V. Radha, S.V. Ushakov, A. Navrotsky, Journal of Materials Research, 24 (2009) 3350-3357.
- [127] B. Paul, K. Singh, T. Jaron, A. Roy, A. Chowdhury, Journal of Alloys and Compounds, 686 (2016) 130-136.
- [128] L. Rapenne, C. Jimenez, T. Caroff, C. Millon, S. Morlens, P. Bayle-Guillemaud, F. Weiss, Journal of Materials Research, 24 (2009) 1480-1491.